Optimisation d'hétéro-structures à multipuits quantiques InGaN sur sous-couche InGaN pour diodes electroluminescentes émettant dans le domaine spectral bleu-vert

Saiful Alam

HAL Id: tel-02431758

https://hal.science/tel-02431758

Submitted on 8 Jan 2020

THESE

ALAM Saiful

Optimisation d'hétéro-structures à multipuits quantiques InGaN sur sous-couche InGaN pour diodes electroluminescentes émettant dans le domaine spectral bleu-vert

---

Thèse soutenue publiquement le 16 Mai 2018 à Metz, devant le jury composé de :

Pr. Abdallah Ougazzaden	Georgia Institute of Technology, USA	Directeur de thèse
Dr. Ivan.-C. Robin	CEA-Leti (DOPT), Grenoble, France	Co-directeur de thèse
Pr. Christian Brylinski	Université Claude Bernard Lyon 1, Lyon, France	Rapporteur
Dr. Eva Monroy	CEA-INAC/PHELIQS, Grenoble, France	Rapporteur
Pr. Evelyne Gil	Université Clermont Auvergne, France	Examinateur
Dr. Pierre Lefebvre	Laboratoire Charles Coulomb, Montpellier, France	Examinateur
Dr. David J. Rogers	Nanovation, Châteaufort, France	Examinateur
Dr. Régine Maillard	LMOPS, Université de Lorraine, France	Examinateur

A Dissertation

Presented to The Academic Faculty by

Saiful Alam

In Partial Fulfillment of the Requirements for the Degree of

Doctor of Philosophy in **Physics**

High Indium Concentration InGaN Multi-Quantum-Well-Based Blue-Green Light-Emitting Diodes Grown on InGaN "Semi-Bulk" Buffer

---

Thesis defended publicly on 16 May 2018 at Metz, with the members of Jury :

Prof. Abdallah Ougazzaden	Georgia Institute of Technology, USA	Advisor
Dr. Ivan-C. Robin	CEA-Leti (DOPT), Grenoble, France	Co-advisor
Prof. Christian Brylinski	University Claude Bernard Lyon 1, Lyon, France	Reporter
Dr. Eva Monroy	CEA-INAC/PHELIQS, Grenoble, France	Reporter
Prof. Evelyne Gil	University Clermont Auvergne, France	Examiner
Dr. Pierre Lefebvre	Laboratory Charles Coulomb, Montpellier, France	Examiner
Dr. David J. Rogers	Nanovation, Châteaufort, France	Examiner
Dr. Régine Maillard	LMOPS, University of Lorraine, France	Examiner

To my parents

ACKNOWLEDGEMENT

TABLE OF CONTENTS

LIST OF TABLES

LIST OF FIGURES

9

LIST OF SYMBOLS AND ABBREVIATIONS

2θ	(XRD) Angle of diffracted X-ray beam
χ	Electron affinity
λ	Wavelength
ω	(XRD) Angle of incident X-ray beam
Φ	(Semiconductors) Electrostatic potential
E_g	Semiconductor band-gap energy
J	Current density
k	Boltzmann constant
n	Density of electrons
p	Density of holes
q	Elementary charge
T	Temperature (in Kelvin)
V	Voltage
AFM	Atomic Force Microscopy
AlGaN	Aluminium Gallium Nitride
AlN	Aluminium Nitride
BF-STEM	Bright-field STEM
CCS	Close Coupled Showerhead
CL	Cathodoluminescence
CRI	Colour Rendering Index
CW	Continuous Wave
EDX	Energy-Dispersive X-ray spectroscopy
ELOG	Epitaxial Lateral Over Growth
EQE	External Quantum Efficiency
FWHM	Full Width at Half Maximum

GaN	Gallium Nitride
HAADF-STEM	High-Angle Annular Dark-Field STEM
HCP	Hexagonal Close Packed
I-V	Current-voltage characteristics
In	Indium
InGaN	Indium Gallium Nitride
InN	Indium Nitride
mlum	Milli-lumen
MOCVD	Metal-Organic Chemical Vapour Deposition
MOVPE	Metal-Organic Vapour-Phase Epitaxy
PL	Photoluminescence
RMS (AFM)	Root Mean Square
RSM (XRD)	Reciprocal Space Mapping
SB	Semi-Bulk
SEM	Scanning Electron Microscopy
Si	Silicon
SIMS	Secondary Ion Mass Spectroscopy
SSDRC	Solid-State Device Research Conference
STEM	Scanning Transmission Electron Microscopy
SAG	Selective Area Growth
WPE	Wall-Plug Efficiency
XRD	X-ray Diffraction

SUMMARY

Solid-state lighting has got much attention for its prospect to reduce lighting energy consumption up to 85% [1]. GaN-based light-emitting diodes (LEDs) have already been commercialized for solid-state lighting [1,2], since the InGaN/GaN-based multi-quantum-well (MQW) of LEDs can be designed to produce light in the entire visible spectral range. There are two approaches to create white light emission from LEDs for lighting applications: the first involves monolithic integration of red (R), green (G), and blue (B) LEDs on the same chip or module and the other approach uses yellow phosphor coating on the surface of blue LED [3]. However, phosphor-based down-conversion results in low efficiency due to Stokes loss [4] and also can yield low colour rendering index (CRI) [3]. Hence, for highly efficient and with high CRI white light, generation of white light by RGB combination is necessary. InGaN/GaN-based blue LED has achieved good performance now-a-days [5]. III-phosphides based red LED has also good efficiency [4]. However, with intermediary wavelengths for green spectra emission, the efficiency of devices from epitaxy grown along the commonly used (0001-Ga) direction of GaN decreases with increasing indium (In) content in the active region [6] and this "green-gap" is the main obstacle to get phosphor-free white LEDs. The separation of electrons and holes within the QWs induced by the built-in piezoelectric field [6], the degraded InGaN crystal quality for high In-content that creates more non-radiative recombination centers because of lower growth temperature [7], and the In segregation or In phase separation due to solid phase miscibility gap [8] are the hurdles to overcome the poor efficiency problem of green light-emitting devices [9]. Non- or semi-polar LED structures could be a solution to reduce or omit the polarization problem, where

selective area growth technique with optimized epitaxial growth parameters allows to grow stable semi-polar or non-polar facets [10]. However, easier growth of good crystal quality and fewer processing steps make (0001-Ga) direction growth still commercially promising. Therefore, optimized structure design to alleviate polarization and enhance optical emission from hetero-structures grown along this direction growth is still in demand. The conventional InGaN multi-quantum-well (MQW) LED structures are grown on GaN buffer and use GaN as barrier layers. However, our objective has been to grow high In-content MQWs with InGaN barriers on a novel so called "semi-bulk" (SB) InGaN buffer. Therefore, the goal of the thesis was to simulate, grow by metalorganic vapour phase epitaxy (MOVPE) and process LED structure with high In-content in the MQW with InGaN barriers, grown on high quality "semi-bulk" InGaN buffer, that will emit in the blue to green spectra.

The external quantum efficiency (EQE) of blue LED has already reached ~80% [5], however, for longer wavelength green emission, the efficiency is still limited for the so called "green-gap". For true green (520 nm - 540 nm), which is required to get high CRI white light by RGB combination, mostly reported wall-plug efficiency (WPE) are less than 40% and recent development by *Osram* has reached around 60% [11]. However, part or full of the light is down-converted by phosphor, which yields poor spectrum full width at half maximum, together with poor CRI, poor colour temperature and enhanced differential aging problem, compared to those for direct green [12]. Moreover, human eyes have the highest sensitivity at green spectra. As a consequence, to reach white LEDs with higher efficiency, it is of great importance to understand the origins of the "green-gap" and to find solutions to the problems induced by these low efficiency and strong droop phenomena for green emission. This is the arena the scope of the thesis lies in.

Chapter 1 discusses about the goal of the thesis. The emergence of solid state lighting, the history of LED and the different materials used for LED fabrication from early age to now have been briefly discussed. It introduces the crystal structure of the III-nitride materials including the properties of GaN. The strain and polarization properties of wurtzite GaN are described. The theory of multi-quantum-well (MQW), the radiative and non-radiative recombination processes and the quantum confined stark effect (QCSE) in MQW are discussed. The chapter ends with the principle of light-emitting diode (LED), the electrical characteristics, the ohmic and Schottky contacts, the different terms of the LED efficiency and an introduction to the value chain of LED fabrication.

Chapter 2 describes the epitaxial growth and characterization techniques. The theory of MOVPE technique is discussed. The reactors used in this thesis work (T-shape and *Aixtron* CCS) are discussed in brief. Different after-growth characterization techniques such as X-ray diffraction (XRD), atomic force microscopy (AFM), scanning electron microscopy (SEM), cathodoluminescence (CL), photoluminescence (PL), secondary ion mass spectroscopy (SIMS), Hall measurement, scanning transmission electron microscopy (STEM) and energy dispersive X-ray (EDX) are discussed in short.

Chapter 3 shows simulation results of the LED structures designed for this thesis work. The simulation method and the details of the results are discussed in terms of polarization, band structure and internal quantum efficiency (IQE).

Chapter 4 shows the epitaxial growth and characterization results of the MQW and LED samples in this thesis work. Detailed study of the "semi-bulk" InGaN buffer growth and optimization is presented in this chapter, together with the optimization of

MQW structures grown on SB buffer, and the optimization of the p-GaN epitaxial growth. The related morphological and optical characterization results along with electrical test of the epi-wafer complete LED structure are presented. The advantages of using InGaN as barriers, and the improvement of emission intensity and the wavelength red-shift effect when InGaN SB buffer is used, are also presented and discussed.

Chapter 5 shows the technological processing of LEDs emitting in blue-cyan spectra grown on InGaN SB buffer. The optimization of the p-contact and the related experimental results are discussed. The processing steps and the electrical test results of the processed LED chips are presented.

Chapter 6 summarizes the results and describes the outlook and perspective of the thesis work. The scientific output of this thesis work such as publications, conference communications are presented.

RESUME

L'éclairage à base de matériaux semi-conducteurs a beaucoup attiré l'attention pour son potentiel à réduire la consommation d'électricité jusqu'à 85% [1]. Les diodes électroluminescentes (DEL) à base de GaN ont déjà été commercialisées comme solution économique d'éclairage [1,2], étant donné que les multi-puits quantiques (MQW) basés sur InGaN/GaN peuvent être conçus pour produire de la lumière dans toute la gamme spectrale visible. Il existe deux approches pour obtenir une émission de lumière blanche à partir des DEL pour les applications d'éclairage : la première implique l'intégration monolithique des DEL rouges (R), vertes (G) et bleues (B) sur la même puce ou module et l'autre approche utilise un revêtement de phosphore sur la surface de la DEL bleue [3]. Cependant, la conversion à base de phosphore conduit à une faible efficacité due à la perte de Stokes [4] et peut également produire un faible indice de rendu des couleurs (IRC) [3]. Par conséquent, pour une efficacité élevée et une lumière blanche avec un IRC élevé, la génération de lumière blanche par combinaison RGB est nécessaire. La DEL bleue basée sur InGaN/GaN présente une bonne performance aujourd'hui [5]. La DEL rouge à base de III-phosphure est également très efficace [4]. Cependant, avec des longueurs d'onde intermédiaires pour l'émission de spectre vert, l'efficacité des dispositifs diminue avec l'augmentation de la composition d'indium (In) dans la région active [6] à cause de l'épitaxie selon la direction de GaN communément utilisée (0001-Ga). Ce « green-gap » est le principal obstacle pour obtenir une DEL blanche sans phosphore. La séparation des électrons et des trous dans les puits quantiques induite par le champ piézoélectrique [6], la qualité de l'InGaN dégradé en raison de la température de croissance plus faible pour un contenu élevé de In qui crée plus de centres de recombinaison non radiatifs [7], la

ségrégation ou la séparation de phase de l'In en raison de l'écart de miscibilité en phase solide [8] sont les obstacles pour surmonter le problème de dégradation de l'efficacité des DELs émettant de la lumière verte [9]. Les structures DEL non ou semi-polaires pourraient être une solution pour réduire ou omettre le problème de polarisation, où la technique de croissance sélective (SAG) avec des paramètres optimisés de croissance épitaxiale permet de développer des facettes semi-polaires ou non polaires stables [10]. Cependant, une croissance plus facile de bonne qualité cristalline avec moins d'étapes de fabrication font que la croissance de la direction (0001-Ga) est toujours commercialement prometteuse. Par conséquent, une conception de structure optimisée pour atténuer la polarisation et augmenter l'émission optique provenant d'hétéro-structures élaborées dans cette direction de croissance est toujours demandée. Les structures de DEL classiques multi-puits quantiques (MQW) InGaN/GaN sont développées sur une template GaN et utilisent du GaN comme couches barrières. Cependant, notre objectif a été de faire croître des MQW à contenu élevé avec des barrières InGaN sur une nouvelle template InGaN appelé « semi-bulk » (SB). Par conséquent, le but de la thèse est de simuler, décroître par épitaxie en phase vapeur organométallique (MOVPE) et de fabriquer la structure de DELs à haute teneur en In dans les barrières MQW avec InGaN, crues sur une template InGaN « semi-bulk » de haute qualité, et qui émettent dans le spectre du bleu au vert.

L'efficacité quantique externe (EQE) de la DEL bleue a déjà atteint ~ 80% [5], cependant, pour une émission verte de plus grande longueur d'onde, l'efficacité est encore limitée pour ce que l'on appelle le « green-gap ». Pour le vert (520 nm - 540 nm), qui est requis pour obtenir une lumière blanche à fort IRC par combinaison RGB, le rendement à la prise (« wall-plug efficiency ») le plus souvent rapporté est

inférieur à 40% et le développement récent par *Osram* atteint environ 60% [11]. Cependant, une partie ou la totalité de la lumière est convertie en phosphore, ce qui donne un spectre pauvre en pleine largeur à mi-hauteur (FWHM), avec un IRC et une température de couleur médiocres comparées à celles du vert (520 nm - 540 nm) [12]. Par conséquent, pour atteindre les DELs blanches avec une efficacité plus élevée, il est très important de comprendre les origines du « green-gap » et de trouver des solutions aux problèmes induisant ces faibles rendements pour les émissions vertes. C'est la problématique autour du quelle s'articule cette thèse.

Le chapitre 1 traite l'objectif de la thèse. L'émergence de l'éclairage à base de semi-conducteurs et l'histoire des DELs et les différents matériaux utilisés pour la fabrication des DELs ont été brièvement discutés. Ce chapitre introduit la structure cristalline des matériaux III-nitrure incluant les propriétés de GaN. Les propriétés de déformation et de polarisation de wurtzite GaN sont décrites. La théorie des multi-puits quantiques (MQW), les processus de recombinaison radiative et non-radiative et l'effet stark quantique (QCSE) dans les MQW sont discutés. Le chapitre se termine par le principe de fonctionnement de la diode électroluminescente, les caractéristiques électriques, les contacts ohmiques et Schottky, les différents termes de l'efficacité des DELs et une introduction aux étapes de fabrication des DELs.

Le chapitre 2 décrit les techniques de croissance épitaxiales et de caractérisation. La théorie de la technique d'épitaxie en phase vapeur organométallique est discutée. Les réacteurs utilisés dans ce travail de thèse (T-shape et *Aixtron* CCS) sont brièvement abordés. Différentes techniques de caractérisation après-croissance telles que diffraction des rayons X, microscopie à force atomique, microscopie électronique à balayage, cathodoluminescence, photoluminescence,

spectroscopie de masse des ions secondaires, mesure à effet Hall, la microscopie électronique à transmission et la dispersion d'électrons par rayons X sont brièvement discutées.

Le chapitre 3 montre les résultats de simulation des structures de DEL conçues pour ce travail de thèse. La méthode de simulation et les détails des résultats sont discutés en termes de polarisation, de structure de bande et d'efficacité quantique interne (IQE).

Le chapitre 4 montre les résultats de croissance et de caractérisation épitaxiale des échantillons élaborés dans ce travail de thèse. L'étude détaillée de la croissance et de l'optimisation de la template InGaN « semi-bulk » (SB) est présentée dans ce chapitre, ainsi que l'optimisation des structures MQW crues sur une template SB et l'optimisation de la croissance épitaxiale de p-GaN. Les résultats de caractérisation morphologique et optique associés ainsi que les tests électriques de la structure DEL complète après croissance sont présentés. Les avantages de l'utilisation d'InGaN comme barrières, et l'amélioration de l'intensité d'émission et de l'effet de décalage de longueur d'onde lorsque la template InGaN SB est utilisée, sont également présentés et discutés.

Le chapitre 5 montre les étapes de fabrication des DELs émettant dans les spectres bleu-cyan élaborées sur une template SB InGaN. L'optimisation du p-contact et les résultats expérimentaux associés sont discutés. Les étapes de fabrication et les résultats des tests électriques des DELs sont présentés.

Le chapitre 6 résume les résultats et décrit les perspectives du travail de thèse. Les résultats scientifiques de ce travail de thèse tels que les publications, les communications de conférence sont présentés.

CHAPTER 1.   INTRODUCTION

1.1   Emergence of solid-state lighting (SSL)

Lighting is closely related to human civilization. Almost 20% of the world's total consumed energy is consumed for lighting applications [13]. Producing electric energy is expensive, both in monetary value (The US alone has an expense of USD 60 billion as the cost of electricity production [13]), and also in terms of impact on climate associated with the use of fossil fuel and carbon dioxide emission. Solid-state lighting using light-emitting diodes (LEDs) can reduce, by more than 50%, the generation of green-house gases related to lighting. Accordingly, lighting will then use less than one-tenth of all electricity generated. In the US scenario, at an average commercial price of 0.10/kilowatt-hour, it corresponds to an annual saving of USD 40 billion [14], saving almost 46% of lighting-related electricity consumption (Figure 1).
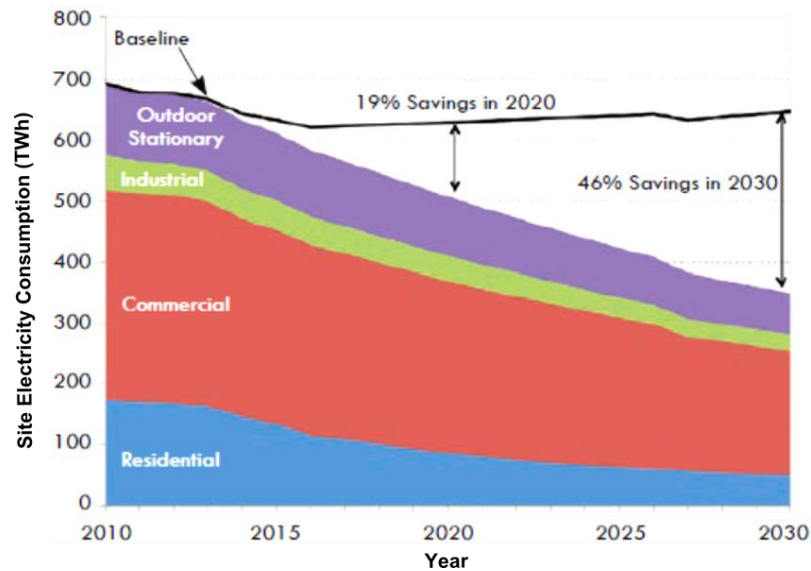
Figure 1 : Energy saving by using SSL (adapted from [14]).

Moreover, LED lighting will provide reductions of at least 10% in fuel consumption and CO_2 emission from power stations within the next ten years [15]. In this way, SSL can significantly improve the global-warming scenario. LEDs can convert electrical energy to light energy very efficiently compared to conventional lighting. Incandescent light bulbs have efficiency lower than 5% for visible light and compact fluorescent lamps (CFL) have around 20%. SSL has already been replacing conventional lighting. Even though LEDs have already been commercialized for SSL solutions, less than 10% of the existing lighting installations use SSL products [12], even with government policy support, due to limited efficiency and higher cost. In order to replace the conventional lighting, the luminous efficiency and cost effectiveness have still to be improved. The main barriers are reliability, color stability and compatibility. This means, there is still progress necessary to overcome fundamental scientific and technological barriers such as efficiency-droop, the "green-gap", using of low-cost substrate or efficient lift-off techniques, to develop or improve materials with high crystal quality, and to improve packaging and extraction efficiency.

Apart from energy saving in general lighting, LEDs can enable better light utilization, improved optical and brightness control, directability, colour tunability, low glare, and design flexibility (for example, *Osram* "Omnipoint" concept). It can also provide improved life-cycle assessment, spectral resolution control for human health, productivity, horticultural lighting, livestock lighting [14], and also high speed communication such as Li-Fi [16]. Compared to CFL lights, they can also lead to a reduction of the consumption of materials that are highly toxic like mercury or lead, or scarce like rare earth elements.

LEDs have a vast area of application other than general lighting, such as automotive head-light, light source for traffic-signal light, full-colour illumination for back-lighting for liquid-crystal displays, decoration lights, street lights [2], and also for healthcare, and plants research [14].

1.2 History of LEDs and materials for LEDs

1.2.1 History of LEDs

After the observation of the emission of visible light of various colours from the region of carborundum (SiC) semiconductor near a metal point contact of a diode by British electrical engineer H. J. Round in 1907, during the period from 1906 to 1940s, various crystalline materials, such as, germanium (Ge), silicon (Si), carborundum (SiC), and copper oxides (CuO and Cu_2O), were observed to exhibit rectifying behaviour applying a sharp metal point contact to the surface [2]. During the period from 1923 to the early 1940s, Russian scientist Lossev rediscovered this same electroluminescence in both forward and reverse-biased point-contact diodes made by single-crystal SiC and made extensive studies of the characteristics of such diodes [2]. However, physics related to modern day direct-bandgap semiconductors was not well understood. In early 1940's, after the development of knowledge of quantum physics, the semiconductor properties of these materials such as Ge, Si etc. were understood. In the 1940's, Russel Ohl of Bell Lab, USA identified p- and n-type properties of Si which led to the finding of similar properties in GaAs later in the 1960's, and this can be considered as the preliminary stages towards p-n junction LEDs. This development of the quantum theory of solids was an important and mandatory element for the understanding of the theory of p-n junction, the properties of light-emission in semiconductors, and ultimately for the development of high-

efficiency LEDs [2]. In 1945, the understanding of minority carrier injection started and the invention of transistor led to a better understanding of p-n junction properties like carrier mobility, injection etc. which paved the way to modern LEDs.

Nick Holonyak Jr, of General Electric, gave the first practical demonstration of LEDs in 1962 [13]. The first commercial LEDs was introduced by HP in 1968 [2,13], and since then the progress of LEDs has proceeded progressively. For the first few years, their colour was limited to red, the material was GaAsP/GaAs, and the light output was in the milli-lumen (mlum) range, suitable only for indicators and alpha-numeric displays. Over the next twenty years, conversion efficacy from electrical current to visible light flux improved by more than 10 times per decade [17], eventually enabling outdoor applications. At the same time, through the use of second-generation GaAsP/GaP:N materials, the colour range expanded from 650 nm deep-red to 635 nm red, 590 nm yellow, 570 nm yellow-green, and the third-generation GaAlAs materials enabled 120 mlum of luminous flux in the red spectrum at a drive current as high as 20 mA [17]. In the 1990's, two major breakthroughs in LED science took place when HP invented AlInGaP high-brightness red and amber LEDs and Shuji Nakamura developed high-brightness GaN- and InGaN-based green and blue LEDs at Nichia [13,17]. Along 1980's and 1990's, the development of OLED came up [13] and also steadily improved simultaneously.

1.2.2 Materials for LEDs

After the Second World War, the semiconductor research started in a broad way. The early investigation was mainly about silicon (Si) and germanium (Ge) and also binary alloys such as GaTe, GaSe. The early materials used for light generation commercially were direct-bandgap gallium arsenide (GaAs) and indium arsenide

(InAs), though in infrared spectra, because gallium phosphide (GaP) with visible spectrum emission was of indirect-bandgap and was unsuitable for high-efficiency light emission [2]. With continuous improvement, GaAs LED emitting in infrared spectrum, achieved good efficiency (EQE ~6%) in the decade of 1960 [1,2]. After the 1962's solid state device research conference (SSDRC), many research groups began to focus on making an infrared laser based on direct-bandgap semiconductor GaAs [2]. Afterwards, ternary alloys such as GaAsP was developed for red emission by several groups [2]. Later on, vapour phase epitaxy (VPE) and liquid phase epitaxy (LPE) techniques were developed and amber, yellow, and yellow-green GaAsP:N LEDs were produced. However, the quantum efficiency was very limited because of limited control of thickness of layers grown by VPE or LPE [2]. Further, AlGaAs and AlGaAs/GaAs double heterostructure were developed for ~750 nm laser fabrication. Later on, more GaAsP, AlGaAs, InGaAs, InAlAs, InGaP, AlAsP, etc. alloys were investigated for light-emitting applications [2,18–21]. Even now-a-days, most commercial yellow and red LEDs are fabricated from InAlGaP [1,22]. They have been used in the red DVD lasers and for all high-power signaling applications. InGaAsP alloy systems have been used for all communications lasers. After the successful application of metalorganic chemical vapour deposition (MOCVD) to the epitaxial growth of injection lasers composed of Al-containing materials in 1977, MOCVD became an obvious choice for the mass production of InAlGaP lasers and LEDs at the beginning of the 1990's [2]. During that period, Mg was established as an acceptor for p-type III-V's and Ikeda and co-workers at Sony Corporation demonstrated the first room-temperature CW operation of InAlGaP injection lasers emitting red. After that dramatic result, the MOCVD-based material production technologies for red, orange and yellow high-brightness LEDs have been developed

for mass production. Figure 2 shows evolution in luminous efficacy of conventional

lighting sources and visible LEDs. A dramatic increase in commercial LED efficiency
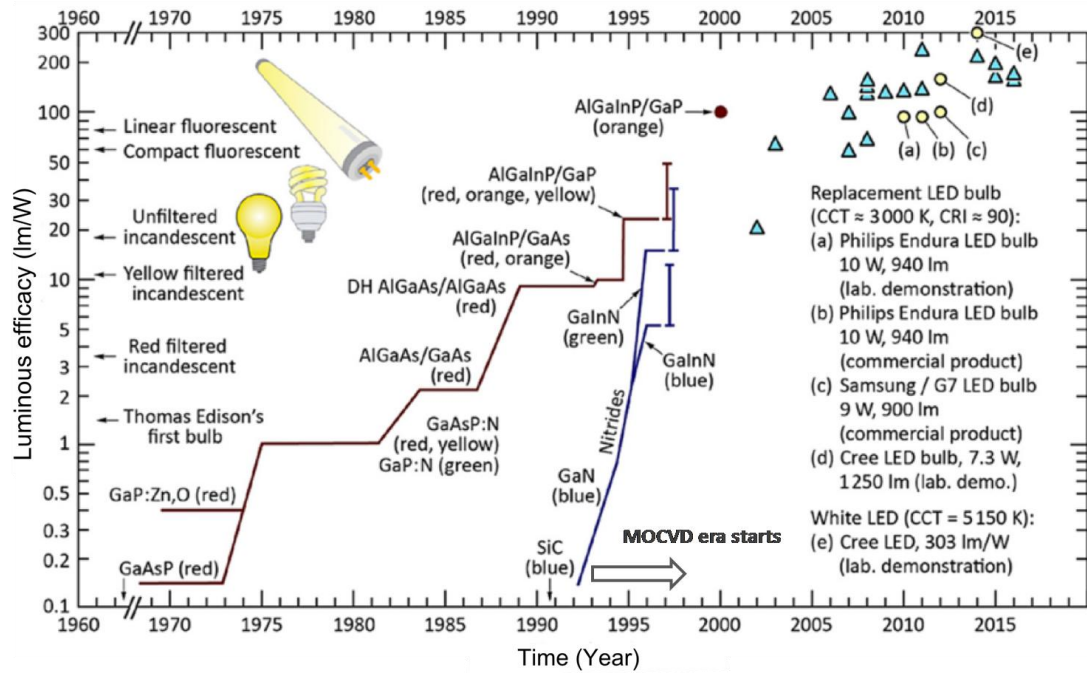
Figure 2: Development of LED materials and evolution of LED efficacy (adapted and updated from [2,12,21]).

upon the development of MOCVD technology for the production of InAlGaP LEDs

emitting in the red, orange, and yellow spectra and InGaN LEDs emitting in the blue-

green spectral regime is noticeable. However, still cost per lumen needed to be

reduced. In the mid 1980's, companies like *Cambridge Instruments*, *Emcore*, *Aixtron*,

Spire etc. started developing commercial large-area MOCVD production reactors that

could address this market and thus provide a viable epitaxy platform for the rapidly

growing high-performance LED market. Moreover, scientific and industrial efforts for

increasing internal quantum efficiency and extraction efficiency and improved

packaging got priority to compete with conventional lighting. Device and epitaxy

improvement by scientists of HP led to red LED with a luminous output greater than

50 lm/W. These device technology and vapour phase epitaxy material growth

technology were important events in the development of high-brightness LEDs and paved the way to make LEDs become a competitive light source.

After J. Pankove and co-workers at RCA Labs began the study of GaN heteroepitaxial films grown on sapphire by VPE, GaN started to take its place in the group of potential LED materials. During that time different groups demonstrated epitaxial growth of GaN and AlN on sapphire aiming at light emission, mostly in near UV spectra [2]. However, no device was demonstrated because p-type GaN could not be achieved. In 1986, Akasaki and co-workers at Nagoya University described a two-step MOCVD epitaxial process for the growth of GaN on sapphire using an AlN low-temperature buffer layer which resulted in much higher quality GaN material [16]. Later, they also successfully demonstrated a GaN p-n junction [2] by using magnesium (Mg) as a dopant, and acceptor-activation using electron beam irradiation [23]. In 1990, Amano and Akasaki demonstrated lasing emission from GaN heteroepitaxial films grown on sapphire, opening the door to use this heteroepitaxial approach to produce LEDs [24]. Shortly thereafter, in 1991, Shuji Nakamura, working at Nichia Corporation, in Japan, demonstrated GaN blue LED using the same Mg dopant for p-GaN and low-temperature buffer layer [25–27]. In the next few years, InGaN and GaN based blue and green LEDs started to generate a high level of scientific and commercial interest. Apart from different optoelectronic research labs around the world, companies such as *Nichia, Cree, Osram, Philips Lumileds* etc. developed research and high-volume production systems for the growth of hetero-structures for high-performance blue and green LEDs [2]. Phosphor-coated blue LEDs are being used commercially to produce white light for general lighting applications and the improved efficacy and luminescence quality have already

achieved competing performance. The latest development of white LEDs by *Nichia*, *Osram*, *Cree* etc. have touched the luminous efficacy of ~300 lm/W (Figure 2).

1.3 III-nitride materials

After the inception of III-nitride (III-N) LEDs, over the past few decades, scientific research and commercial interest have resulted in demonstration of blue and green laser diodes (LDs) [2,28], and blue, green, red, and white LEDs [29–32]. Apart from LEDs and LDs, high electron-mobility transistors [33–38], solar cells [39], sensors [40] and UV photo detectors [41–43] have been realized with III-N semiconductors. The main advantage of III-N semiconductors such as aluminium nitride (AlN), gallium nitride (GaN), indium nitride (InN), is that these semiconductors and their alloys have wide bandgap (ranging from 0.65 eV to 6.05 eV) and except BN all other binary and ternary alloys have direct bandgap that gives them the suitability for light-emitting applications.
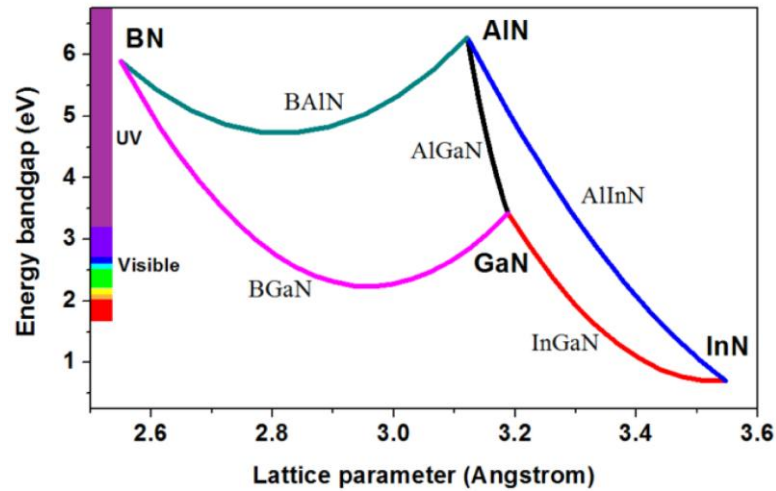
Figure 3: Bandgap energies of different III-nitrides and their alloys showing the suitability of light-emission from infrared to ultraviolet spectra [44].

They can cover spectral range from the near infrared to the entire visible, and also the near and deep ultraviolet. III-nitrides also display high chemical, mechanical, and

thermal stabilities, high thermal conductivities, high carrier saturation drift velocities, and high radiation hardness, making devices suitable for harsh environment, long lifetime, and reliable [28].

1.3.1 Crystal structure of III-nitrides

There are two main polytypes for group III-nitrides: hexagonal wurtzite and cubic zincblende, among which the hexagonal wurtzite structure is thermodynamically stable for bulk III-nitrides. In this thesis work, the crystal structure of all the samples was of wurtzite type. Such a crystal structure has a hexagonal unit cell and therefore is described by the lattice constants a (in-plane) and c (out-of-plane) [46]. Figure 4 shows the GaN crystal structure. The wurtzite structure consists of two inter-penetrating hexagonal close packed (HCP) sub-lattices, each with one type of atoms. They are offset along the c-axis by 3/8 of the cell height, i.e. 3c/8 [45]. Group-III elements alloying occurs within the plane of cations.
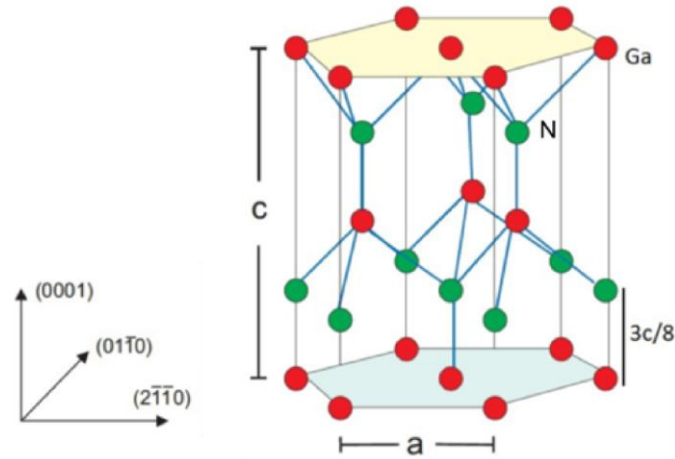
Figure 4: Wurtzite crystal structure of GaN [45].

1.3.2 Strain

Strain is a common phenomenon during epitaxial growth of heterostructures with different lattice constants and thermal expansion coefficients of the different layers [46]. In particular, a heterostructure is strained when an epi-layer is grown on a substrate with different in-plane lattice parameter. Small amount of in-plane strain is accommodated by small deformation of the lattice in the out-of-plane direction [45]. During the epitaxial growth of a thin layer with moderate lattice mismatch, the in-plane lattice constant of the epi-layer (a_e) is forced to stay very close to that of the substrate layer (a_o). This represents the so-called pseudomorphic growth regime. The resulting biaxial in-plane strain can be defined as [46],

$$\varepsilon_x = \frac{a_o - a_e}{a_e}$$

And the out-of-plane strain can be defined as [46],

$$\varepsilon_z = \frac{c_o - c_e}{c_e}$$

If $a_o < a_e$, compressive strain is caused, if $a_o > a_e$, tensile strain is caused and for $a_o = a_e$, no strain happens (Figure 5).

In both the strain cases, the strain in the epi-layer can generate misfit dislocations, if the epi-layer thickness is beyond the critical thickness associated with epi-layer/substrate combination of materials [46]. The ε_x and ε_z are related by,

$$\varepsilon_z = -\frac{2\nu}{1-\nu}\varepsilon_x$$
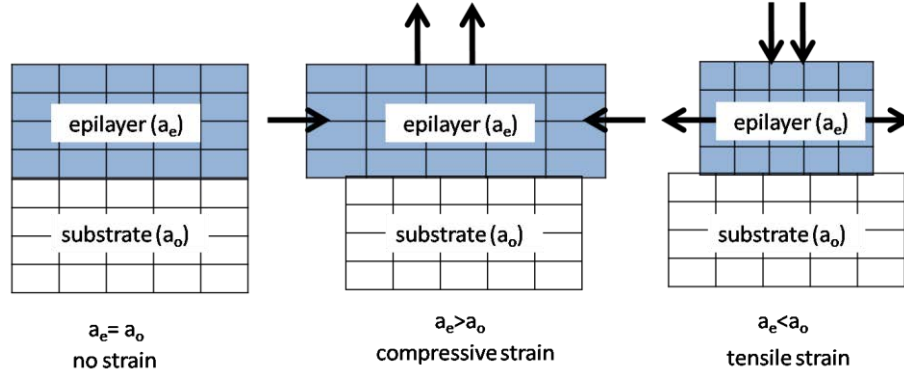
Figure 5: Pseudomorphic strain scenario of a lattice matched or mismatched epilayer (schematically).

Here, ν is the Poisson ratio. In the pseudomorphic growth regime, these relations can be used to determine the composition of materials from the symmetric 2θ-ω scan data on the (002) reflection in X-ray diffraction. The Poisson coefficients of III-nitrides are tabulated in Table 1.

Table 1: Poisson coefficients of III-nitrides (after ref. [28])

	GaN	AlN	InN
ν	0.212	0.203	0.272

For ternary alloys, the Poisson coefficient is usually approximated by linearly interpolating the Poisson coefficients of the end-point binaries. For example, the Poisson coefficient ν_{ABN} of the ternary alloy $A_xB_{1-x}N$ is given by [28],

$$\nu_{ABN} = x\,\nu_{AN} + (1-x)\,\nu_{BN}$$

The stress components of an elastically deformed body in equilibrium can be expressed by two in-plane and one out-of-plane components in each dimension (Figure 6). The stress components are therefore expressed as a 3×3 tensor [45],

$$\begin{pmatrix} \sigma_{11} & \sigma_{12} & \sigma_{13} \\ \sigma_{21} & \sigma_{22} & \sigma_{23} \\ \sigma_{31} & \sigma_{32} & \sigma_{33} \end{pmatrix}$$
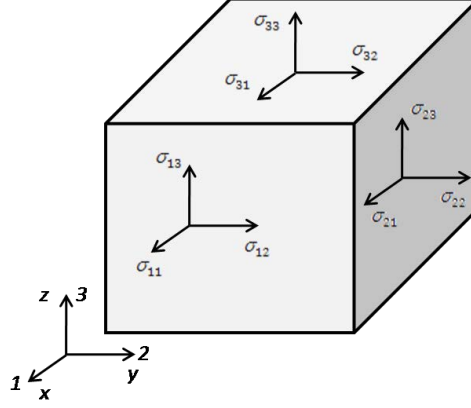
Figure 6: Graphical interpretation of all the stress components with one element.

Strain ε can also be expressed similarly with a 3×3 tensor and linked to stress σ by Hooke's law of elastic deformation [45],

$$\sigma = C.\varepsilon$$

Here, C is a tensor of 4th order with 34 components which contains material specific elastic constants. The simplified form of Hooke's law for the wurtzite crystal can be obtained by the use of symmetry constraints and Voigt's notation [45],

$$\begin{pmatrix} \sigma_{11} \\ \sigma_{22} \\ \sigma_{33} \\ \sigma_{12} \\ \sigma_{23} \\ \sigma_{31} \end{pmatrix} = \begin{pmatrix} C_{11} & C_{12} & C_{13} & 0 & 0 & 0 \\ C_{12} & C_{22} & C_{13} & 0 & 0 & 0 \\ C_{13} & C_{13} & C_{33} & 0 & 0 & 0 \\ 0 & 0 & 0 & C_{44} & 0 & 0 \\ 0 & 0 & 0 & 0 & C_{44} & 0 \\ 0 & 0 & 0 & 0 & 0 & C_{66} \end{pmatrix} \times \begin{pmatrix} \varepsilon_{11} \\ \varepsilon_{22} \\ \varepsilon_{33} \\ \varepsilon_{12} \\ \varepsilon_{23} \\ \varepsilon_{31} \end{pmatrix}$$

Where $C_{66} = \frac{1}{2}(C_{11} - C_{12})$. If only biaxial stress is considered ($\sigma_{11} = \sigma_{22}$, $\sigma_{33} = 0$), e.g. in the case of the c-plane GaN layer grown on sapphire, all the shear stress components which have mixed subscript in 1, 2 and 3 vanish to zeros and the free-

surface boundary condition $\sigma_{33} = 0$ is applicable [45]. Elastic constants of III-nitrides are shown in Table 2.

Table 2: Elastic constants of III-nitrides (After references [47–49])

Elastic constant (GPa)	GaN	AlN	InN
C_{11}	390	396	223
C_{12}	145	137	115
C_{13}	106	108	92
C_{33}	398	373	224
C_{44}	105	116	48
C_{66}	123	297	141

1.3.3   Polarization

Polarization is an important feature of III-nitride materials that differs them from many other semiconductors such as silicon (Si). The total polarization vector ($\vec{P}$) in the wurtzite III-N semiconductors has two components, spontaneous polarization ($\vec{P}_{sp}$) and piezoelectric polarization ($\vec{P}_{pz}$), while cubic semiconductors have no spontaneous polarization [46].

$$\vec{P} = \vec{P}_{sp} + \vec{P}_{pz}$$

Spontaneous polarization:

The partial ionic chemical bond in GaN creates dipole moment between two nearest atoms pointed from N to Ga. Due to the attraction between third neighbouring atoms in the wurtzite crystal structure, these dipole moments do not cancel out as they do in the case of cubic crystals. The 3D density of electric momentum in the

unstrained material is called the spontaneous polarization $\vec{P}_{sp}$ [45]. Wurtzite GaN has no inversion-symmetry, which means that the directions ⟨0001⟩ and ⟨000$\bar{1}$⟩ are not equivalent. Thus, there are two different orientations of the (0001) faces: the Ga-face and the N-face with Ga and N atoms in the top position of the bilayer, respectively, resulting in different chemical properties (Figure 7).
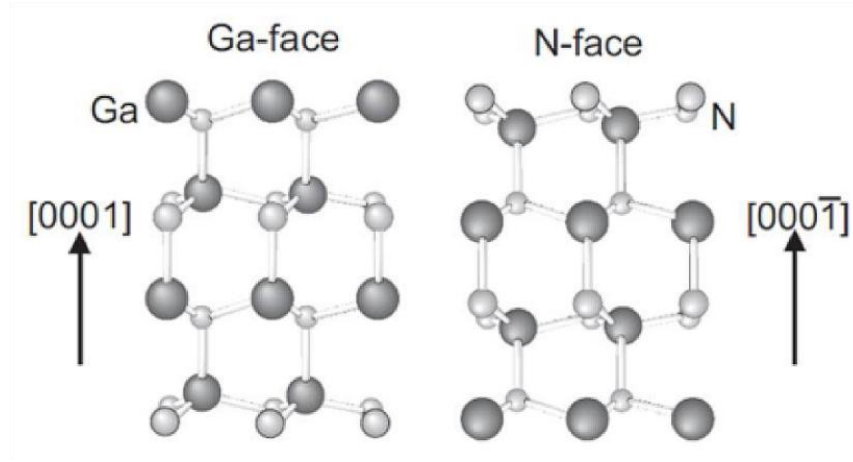
Figure 7: The two different faces of GaN: Ga-polar and N-polar [50].

For Ga-polar GaN, the $\vec{P}_{sp}$ points opposite to the growth direction, that means the ⟨000$\bar{1}$⟩ direction. Several groups have calculated theoretically the $\vec{P}_{sp}$ for III-nitrides, however, the article by Bernardini and Fiorentini [52] provides the most accepted values, shown in Table 3.

Table 3: Spontaneous polarization in some III-nitrides (Data from [52,53])

Spontaneous polarization (Cm^{-2})	GaN	AlN	InN
P_{sp}	-0.034	-0.09	-0.042

The spontaneous polarization in nitride ternary alloys can be modeled [53] almost perfectly using a linear interpolation with a quadratic correction term involving the bowing parameter,

$$P_{sp}^{ABN} = xP_{sp}^{AN} + (1-x)P_{sp}^{BN} + bx(1-x)$$

Where, b is the bowing parameter.

The electrostatic field $\overrightarrow{E_{sp}}$ induced by spontaneous polarization is [45],

$$\overrightarrow{E_{sp}} = \frac{P_{sp}}{\varepsilon_r \varepsilon_o}\hat{z}$$

Where P_{sp} is the spontaneous polarization coefficient, ε_r is the relative dielectric constant of the material for which the field is calculated, ε_o is the electrostatic dielectric constant of free space and $\hat{z}$ is the unit vector along the positive c-axis of the hexagonal crystal. For InGaN/GaN-based QWs, this value depends on the InGaN composition [54]. The positive sign indicates the direction $\langle 0001 \rangle$.

Piezoelectric polarization:

Piezoelectric polarization is induced by strain and can be related to stress σ_{jk} or strain ε_{jk} via piezoelectric modulus tensor d_{jk} or e_{jk}, respectively, using the following equations [45],

$$P_{pz,i} = d_{jk,i}\sigma_{jk} = e_{jk,i}\varepsilon_{jk}, \text{ where, } i=1, 2, 3$$

Where $P_{pz,i}$ with $i = 1, 2, 3$ are the piezoelectric polarization components along the x, y and z axes respectively. Making simplification for GaN hexagonal crystal structure by Voigt's notation [45],

$$
e = \begin{pmatrix} 0 & 0 & 0 & 0 & e_{15} & 0 \\ 0 & 0 & 0 & e_{15} & 0 & 0 \\ e_{31} & e_{31} & e_{33} & 0 & 0 & 0 \end{pmatrix}
$$

or

$$
d = \begin{pmatrix} 0 & 0 & 0 & 0 & d_{15} & 0 \\ 0 & 0 & 0 & d_{15} & 0 & 0 \\ d_{31} & d_{31} & d_{33} & 0 & 0 & 0 \end{pmatrix}
$$

Hooke's law is also valid and $e = dC$, where C is the tensor of elastic constants. In the general case for the wurtzite crystal structure, the piezoelectric polarization vector is only dependent on e_{31}, e_{33}, e_{15} and the strain status is,

$$
\begin{pmatrix} P_{pz,1} \\ P_{pz,2} \\ P_{pz,3} \end{pmatrix} = \begin{pmatrix} 0 & 0 & 0 & 0 & e_{15} & 0 \\ 0 & 0 & 0 & e_{15} & 0 & 0 \\ e_{31} & e_{31} & e_{33} & 0 & 0 & 0 \end{pmatrix} \cdot \begin{pmatrix} \varepsilon_{11} \\ \varepsilon_{22} \\ \varepsilon_{33} \\ \varepsilon_{12} \\ \varepsilon_{23} \\ \varepsilon_{31} \end{pmatrix}
$$

And finally,

$$
\begin{pmatrix} P_{pz,1} \\ P_{pz,2} \\ P_{pz,3} \end{pmatrix} = \begin{pmatrix} e_{15}\,\varepsilon_{23} \\ e_{15}\,\varepsilon_{12} \\ e_{31}\,\varepsilon_{11} + e_{31}\,\varepsilon_{22} + e_{33}\,\varepsilon_{33} \end{pmatrix}
$$

Similar as spontaneous polarization, the electrostatic field $\overrightarrow{E_{pz}}$ induced by piezo-electric polarization is,

$$
\overrightarrow{E_{pz}} = \frac{P_{pz}}{\varepsilon_r \varepsilon_o}\,\hat{z}
$$

Where P_{pz} is the piezoelectric polarization coefficient. The values of the piezoelectric coefficients of GaN, AlN, and InN are summarized in Table 4.

Table 4: Piezoelectric coefficients of some III-nitrides (Data from [52,53])

Piezoelectric polarization (Cm^{-2})	GaN	AlN	InN
e_{31}	-0.338	-0.533	-0.412
e_{33}	0.667	1.505	0.815
e_{15}	0.398	0.480	0.400

<u>Piezoelectric polarization in In$_x$Ga$_{1-x}$N/GaN system</u>

The net piezoelectric polarization in the ternary is obtained from the weighted sum of the piezoelectric polarizations of the binaries. For pseudomorphic In$_x$Ga$_{1-x}$N in-plane lattice-matched on GaN , the in-plane strain is [28],

$$\varepsilon_x = \frac{a^{GaN} - a_x}{a_x}$$

Where a_x is the relaxed lattice parameter of In$_x$Ga$_{1-x}$N. Using Vegard's law the expression can be rewritten as,

$$\varepsilon_x = \frac{x(a^{GaN} - a^{InN})}{xa^{InN} + (1-x)a^{GaN}}$$

And hence the piezoelectric polarization for In$_x$Ga$_{1-x}$N alloy is calculated by [28],

$$P_{pz}(\text{In}_x Ga_{1-x}N, \varepsilon_x) = xP_{pz}(InN, \varepsilon_x) + (1-x)P_{pz}(\text{GaN}, \varepsilon_x)$$

For In$_x$Ga$_{1-x}$N, pseudomorphically strained with respect to GaN, the magnitude of this piezoelectric field can be expressed as [46],

$$E_{pz} = \frac{P_{pz}}{\varepsilon_r \varepsilon_o}$$

Where also ε_r is the relative dielectric constant of the material for which the field is calculated and ε_o is the electrostatic dielectric constant of free space.

General theory of dipole momentum shows that a 3D distribution of dipoles with polarization vector $\vec{P}$, within a 3D volume limited by a 2D surface border, has electrostatic effect similar to that of a 3D density of virtual "polarization" charges $\rho = -div(\vec{P})$, together with 2D "polarization" charge density $\rho_s = \vec{P}.\vec{n}$, at the surface (where, $\vec{n}$ is the vector normal to the surface). For a uniform polarization in the material, the 3D charge density vanishes and the surface charges can describe the electrostatic state of the material. For two different piezoelectric materials, the difference of total polarization gives rise to interface sheet electric charge σ_s,

$$\sigma_s = P_{tot}^{top} - P_{tot}^{bottom}$$

Generally, the strength of the polarization-induced electric field along [0 0 0 1] in layer j of thickness l_j of a N-layered structure is given by,

$$E_j = \frac{\sum_{k=1}^{N} \frac{P_k l_k}{\varepsilon_k} - P_j \sum_{k=1}^{N} \frac{l_k}{\varepsilon_k}}{\varepsilon_j \sum_{k=1}^{N} \frac{l_k}{\varepsilon_k}}$$

Where ε_j is the dielectric constant of the jth layer. This is in accordance with the continuity of the normal component of the electric displacement D at the interfaces,

$$\vec{D} = \varepsilon_o \vec{E} + \vec{P}$$

Where ε_o is static vacuum dielectric constant and,

$$D_{j+1} - D_j = \sigma_k$$

Where σ_k is the density of virtual polarization charges at the kth interface between layers j and $j+1$.

In the simulation of structure in this thesis work, the polarization related quantities were calculated using the Silvaco TCAD by ATLAS software suite where the numerical simulations have been conducted using material parameters from [53].

1.3.4 Quantum well

Quantum wells are commonly used in modern hetero-junction compound semiconductor LEDs. In a multi-heterostructure system, if the active region material (with low bandgap energy) is sandwiched between two barrier layers (with wider bandgap energy), a type-I heterostructure is formed. Type-II heterostructure is formed when the bandgaps overlap, but ΔE_c and ΔE_v have opposite signs. For the active layer thickness comparable to de Broglie wavelength of the carriers (electrons and holes), quantum confinement happens and carriers occupy discrete energy levels. The carriers are potentially confined along the QW growth direction, i.e. x-direction as shown in Figure 8, within the QW. Since the band gap of InGaN is smaller than that of GaN, InGaN acts as the active region with GaN as the barriers in InGaN/GaN QWs [45]. A type-I heterostructure is formed because of the affinity values of GaN and InGaN. The envelope carrier wave function $\Psi(x)$ can be found as a solution of time-independent Schrödinger equation. $\Psi^2(x)$ represents the probability to find a carrier at a certain location x. When the thickness of the active region becomes comparable to the de Broglie wavelength of the carriers, the energy is quantized within QWs [45]. The time-independent Schrödinger equation for a typical single finite QW is,

$$-\frac{\hbar^2}{2m^*}\frac{d^2\psi}{dx^2} + V_0\psi = E\,\psi$$

Where, E represents the particle energy, m^* is the effective mass of electron or hole and V_0 is the potential barrier height.
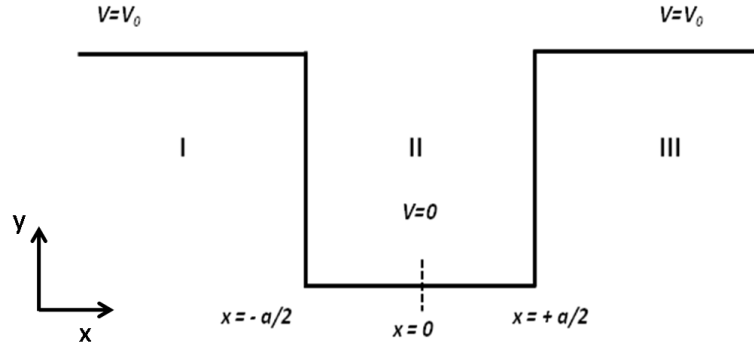
Figure 8: Typical single quantum well (schematically, electron band diagram is shown).

For region I and III (Figure 8), the solutions are,

$$\psi_1 \sim e^{k_1 x} \text{ and } \psi_3 \sim e^{-k_1 x}$$

Where $k_1 = \sqrt{\frac{2m^*(V_0 - E)}{\hbar^2}}$.

For region II, the solution is, $\psi_2 = Ce^{ik_2 x} + De^{-ik_2 x}$, where $k_2 = \sqrt{\frac{2m^*E}{\hbar^2}}$ and C, D are constants.

Using continuity theory and boundary conditions, and putting in trigonometric forms,

$$k_1 = k_2 \tan\frac{k_2 a}{2} \text{ and } -k_1 = k_2 \cot\frac{k_2 a}{2}$$

k's are functions of E and V_0 and solving these two equations numerically, the energy E can be calculated.

This solution method can be extended for multiple-quantum-well. In addition, in the case of thin barrier the quantum mechanical tunneling effect cannot be ignored and this coupling effect has to be taken into account.

As the energy is quantized in the quantum well, it is impossible for electron to be at the bottom of the conduction band or at the top of the valence band, as a result, the effective bandgap of the QW ($E_{g,qw}$) is higher than the active region bandgap ($E_{g,active}$) and can be expressed as [45],

$$E_{g,qw} = E_{g,active} + E_{o,e} + E_{o,h}$$

Where $E_{o,e}$ and $E_{o,h}$ are the 0th energy level of electron in the conduction band and the hole in the valence band, respectively. The effective bandgap of InGaN decreases with increasing In content [45]. This is the reason why high In content results in longer wavelength emission, as in our blue-green LEDs.

1.3.5 Quantum confined stark effect (QCSE)

The use of QWs in LEDs provides carrier confinement into a small fraction of the device, as well as tuning of the emission energy by tuning the alloy composition of the confinement layer. In InGaN/GaN QWs, the strong spontaneous and piezoelectric polarization results in charge accumulation at the hetero-interfaces, which results in large electric fields, in the range of 1.5-3 MVcm^{-1} [47,55,56]. The relation between this electric field and polarization is,

$$F_{qw} = \frac{P_{sp,b} - P_{sp,qw}}{\varepsilon_{e,qw}\,\varepsilon_o} - \frac{P_{pz,qw}}{\varepsilon_{e,qw}\,\varepsilon_o}$$

Where, $P_{sp,b}$ is the spontaneous polarization of the barrier, $\varepsilon_{e,qw}$ is the relative dielectric permittivity of the QW material.

This equation is valid for a QW with unstrained barriers. However, for GaN/In$_x$Ga$_{1-}$$_x$N/GaN system with strained barriers, the additional piezoelectric polarization of the barriers and in the case of thin barriers, the additional spontaneous polarization of the barriers must also be considered.

Figure 9: Quantum confined stark effect: QW without electric filed (left) and with electric field (right).

The polarization induced electric field leads to an inclination of valence band and conduction band edges in the QW. As a result, electrons are driven to the upper surface of the conduction band and holes to the lower surface of the valence band. This spatial separation of carriers decreases the overlap of the respective wave functions and thus reduces the recombination probability in the active region which is the so called quantum confined stark effect (QCSE) [46]. This effect is shown schematically in Figure 9. With higher indium content, the strain increases and so does the piezoelectric field. This makes the fabrication of InGaN-based efficient longer wavelength (for example, green) LEDs challenging. Increase of carrier density in the well can screen the electric field and thus can reduce the QCSE to some extent and can cause a blue-shift in the emission [47,57–61].

1.3.6   Recombination mechanisms in multiple quantum well

Radiative and non-radiative recombination

Electron leaving the higher energy conduction band in order to fill a hole of the lower energy valence band corresponds to a process called recombination. The release of excess energy is either in the form of photons which is radiative recombination, or is not associated with photon generation, which is non-radiative recombination.

There are three types of radiative recombination.

• **Band-Band recombination:** An electron from the conduction band directly recombines with the hole in the valence band and thus photon is emitted, with the energy equal to the bandgap energy E_g (in the case of bulk material) or $E_{g,qw}$ (in the case of QWs) [46].

• **Exciton recombination:** An exciton (X) is a bound state of an electron and a hole which are attracted to each other by electrostatic Coulomb force. The exciton has slightly lower energy than the unbound electron and hole [45]. The exciton may combine with a donor or an acceptor atom forming the donor-bound exciton (D^oX) or the acceptor-bound exciton (A^oX), respectively and thus reducing the total energy further lower. In excitonic recombination, the energy of the emitted photons is smaller than the bandgap energy [45].

• **Donor-acceptor pair (DAP) recombination:** Sometimes, if optically excited at a low temperature, electrons can be trapped forming neutral donors and holes can be trapped forming neutral acceptors. Most of these sites will lead to DAP recombination [45].

Different types of radiative recombination are shown in Figure 10.

Figure 10: Different types of radiative recombination.

There are mainly two types of non-radiative recombination [46].

• **Trap-assisted or Shockley-Read-Hall (SRH) recombination:** Electron and hole are trapped in an intermediate energy level in the bandgap caused by impurity atoms or some structural defects. The released energy is absorbed in phonons or multiple phonons plus photons [46]. This process is governed by the minority carrier concentration and the recombination rates can be expressed as,

$$R_p = \frac{\Delta p}{\tau_p} \text{ (for } n \gg p\text{), and } R_n = \frac{\Delta n}{\tau_n} \text{ (for } n \ll p\text{)}$$

Where Δn, Δp are number of excited minority carriers (electrons and holes, respectively), and τ_n, τ_p are minority carrier lifetimes (for electrons and holes, respectively).

• **Auger recombination:** The electron in the conduction band is recombined with a hole in the valence band and the released energy is transferred to another electron as kinetic energy which electron, then, is excited to higher energy state [45]. Since, three particles are involved, the recombination rate can be expressed as,

$$R_{auger} = (C_n.n + C_p.p)(pn - n_i^2)$$

Where C_n, C_p are Auger coefficients for Auger electrons or holes, respectively; n and p are electron and hole concentrations, respectively; and n_i is the intrinsic carrier concentration. For excess electron concentration, $\Delta n \gg n, p$ and it can be written,

$$R_{auger} = C_n.\Delta n^3.$$

Figure 11: Different types of non-radiative recombination.

Different types of non-radiative recombination processes are shown in Figure 11.

1.4 GaN-based light-emitting diode (LED)

In principle, LED is a p-n junction diode, which can be a homo-junction formed by the same semiconductor materials with n- and p-doping or hetero-junction formed by two same or different semiconductors one with larger bandgap and one with smaller bandgap, joined together forming an abrupt junction. In a forward biased homo p-n junction, electrons are injected or diffused from n-side to p-side and holes in the opposite way. At the junction or near the junction, the electrons and holes can recombine and emit photons [46]. In addition to minority carrier recombination, there is also minority carrier diffusion [45]. On the other hand, in the multi-heterojunction, where a thin layer of semiconductor with a smaller bandgap is sandwiched between

two wider bandgap semiconductors of p-type and n-type, a quantum well based LED is formed, and electrons and holes injected across the p-n junction are confined within the well. Since the carrier concentration is higher due to the confinement in a thin well with barrier layers on two sides, the chance for recombination and emitting photons is higher compared to homo-epitaxial p-n junction [45]. Moreover, multiple number of QW also increases the amount of confined carriers and results high optical output power for LEDs [62]. This is why most present III-V or III-N LEDs are based on MQW.

The typical GaN-based basic LED structure is shown schematically in Figure 12.

Figure 12: Typical GaN-based basic LED structure.

Typical LED consists of GaN template on foreign substrate mainly sapphire (or Si). On top of this, there are n-doped GaN (with typical carrier concentration in the order of $\sim 10^{19}$ cm^{-3}), active region (MQW), p-doped GaN (with typical carrier concentration in the order of $\sim 10^{17}$ cm^{-3}), and p- and n-contacts.

Conception and fabrication steps of GaN-based LEDs

GaN-based LED fabrication is a long value chain. The LED conception starts with the design and simulation of the materials, LED structure and the whole device. After the design, first, the semiconductor material layers (as shown in the preceding paragraph) are epitaxially grown on foreign substrates by material growth techniques such as metalorganic vapour phase epitaxy or molecular beam epitaxy. Then the LED epi-wafer is technologically processed to make LED chips. The process basically includes dielectric deposition, lithography, mesa etching, junction passivation, n- and p-contact metal deposition and lift-off. The processed LED chips are diced and the micro-scale chips are then encapsulated in the package with wire bonding and afterwards the packaged final LEDs are ready for use or sale.

Figure 13: Typical LED fabrication steps: from epitaxy to final packaging (adapted from Aixtron's data sheet[1])

Figure 13 shows the LED anatomy in a compact way from epitaxy to processing and final packaging. All the three steps: epitaxy, device processing and packaging require intensive study, optimization, and scientific and technological advancement. This

---

[1] www.aixtron.com

thesis work is concerned with only epitaxial growth of LED structures and technological processing of epi-wafer LEDs.

LED electrical characteristics

The ideal p-n junction diode current equation is [1],

Figure 14: Homo-junction and hetero-junction LEDs (schematically).

$$I = I_s \left(e^{\frac{V}{V_t}} - 1 \right)$$

Where I_s is the reverse bias saturation current or "dark current", $V_t = \frac{kT}{q}$ is the thermal potential (V_t = 25.9 mV at 300 K), k is the Boltzmann constant and q is the charge of electron. However, practical diode has recombination current in the depletion region in addition to carrier diffusion current [45]. So the diode equation becomes,

$$I = I_{recombination} + I_{diffusion}$$

A typical diode *I-V* curve is shown in Figure 15.

Diode turn-on voltage and resistance

The voltage at which the diffusion current starts to dominate or LED starts emitting light is called the diode turn-on voltage [45]. This voltage is different with

52

Figure 15: Typical diode *I-V* curve [45].

different bandgap materials and hence for different emitted light wavelengths. Ideally, the turn-on voltage V_o can be approximately expressed by the equation,

$$E_{bandgap} = eV_o$$

However, at high temperature the turn-on voltage of LED is reduced due to the fact that at higher temperature, for a given bias voltage, more carriers can reach the opposite side [63]. Furthermore, with the presence of defects, the turn-on voltage of LED might slightly be reduced [63].

Practically, LED has series and parallel resistance effect. High series resistance is observed due to the barrier at the InGaN/GaN interface, or at the p-side ohmic contact, or at the p-GaN contact layer, or at the lateral access distance to the p and n contacts [64]. The parallel conductance may be a result of defects, which causes paths that bypass the p-n junction [63]. Therefore, low series resistance and high parallel resistance are required for realizing better LED electrical performance. However, with the presence of defects, the reverse leakage current also increases due to trap-assisted

tunneling [63], which has a severe detrimental effect on device performance and lifetime.

The diode current equation can be re-expressed taking series and parallel resistance into account [45],

$$I - \frac{V - IR_s}{R_p} = I_s \left(e^{\frac{q(V - IR_s)}{nkT}} - 1 \right)$$

Where R_s and R_p are the series and parallel diode resistances, respectively, k is Boltzmann constant, T is temperature in K, and n is the ideality factor.

Contact resistance: ohmic and Schottky contact

Metal-semiconductor contact can behave either as a Schottky barrier or as an ohmic contact depending on the characteristics of the interface. Contacts which satisfy Ohm's law are called ohmic contacts (Figure 16).

Figure 16: Typical *I-V* curves of metal / semiconductor / metal structures, illustrating the ohmic and Schottky types of contacts.

A good ohmic contact is expected to have the smallest parasitic voltage drop possible at the contact, and the voltage drop occurring across the contact has to be proportional

to the current, so that the contacts do not introduce uncontrollable and unexpected nonlinear elements into the circuit [45]. Typically a metal-semiconductor contact behaves as a Schottky barrier. However, in the case of highly doped semiconductor, the depletion region becomes very thin. At very high doping levels, a thin depletion layer becomes quite transparent for electron tunneling [45]. The band diagram in Figure 17 shows the majority current flow in the block of uniformly heavily doped semiconductor material of length l with ohmic contacts at each end. The applied voltage V drives a uniform current I through the bulk semiconductor and ohmic contacts of cross sectional area A.

Figure 17: Ideal contacts to a heavily doped semiconductor with uniform current density [45].

Then, under the low-current assumption that the voltage drop across both metal-semiconductor contacts is identical, the *I-V* relation becomes [45],

$$V = V_{bulk} + 2V_{contact} = (R_{bulk} + 2R_{contact})I$$

Where, $\qquad R_{bulk} = \dfrac{dV_{bulk}}{dI} = \dfrac{\rho l}{A}$ and $R_{contact} = \dfrac{dV_{contact}}{dI} = \dfrac{\rho_c}{A}$

Here l is the length of the bulk semiconductor, A is the cross-sectional area, ρ is the bulk resistivity, and ρ_c is the specific contact resistivity. Since the voltage required to

drive current through a good ohmic contact is small, the definition of ρ_c can be restricted to zero applied voltage [45],

$$\rho_c = \lim_{V \to 0} \frac{dV_{contact}}{dJ}\ \Omega.cm^2$$

Where, J is the current density ($=I/A$).

Schottky contact and ohmic contact realization

In a Schottky contact, the main conduction mechanism at moderate bias is thermionic emission over the metal-semiconductor junction barrier (Figure 18). The contact resistivity can be given by the equation [45],

$$\rho_c = \frac{k}{qAT}\left(e^{\frac{2\,\Phi_B}{kT}}\right)\Omega.cm^2$$

Where A is the Richardson's constant, k is Boltzmann constant, T is temperature in K, A is cross-sectional area, and Φ_B is the lowest barrier height.

Figure 18: Thermionic emission for Schottky contact (left) and field emission (tunneling) for ohmic contact (right), where Φ_B is the metal-semiconductor barrier [45].

Schottky contacts are formed, when,

- Doping in the semiconductor is not very high (maximum 10^{17} to 10^{19} cm^{-3}, depending on semiconductor bandgap) [45]

- The metal work function is greater than the n-type semiconductor and lower than the p-type semiconductor work function

- Very high density of surface states induced "pinning" of the Fermi level at the surface with respect to the conduction band

Ohmic contacts can be realized by,

- Band alignment by using a metal with a work function Φ_m, which is equal to or smaller than the work function of the semiconductor Φ_s. However, this is hard to realize, especially in GaN based LEDs due to Fermi level "pinning" and surface states [65].

- High doping in the semiconductor so that carriers can pass by tunneling through the barrier due to increased concentration leading to thinner depletion region.

By optimizing the structure design and the epitaxial growth conditions, the internal quantum efficiency of LED can be improved. Further improvement in the external quantum efficiency can be done by high quality n-type and p-type ohmic contacts having low contact resistance and high reflectivity (to increase light extraction efficiency). For p-contact, different metal alloys with large work functions have been investigated by researchers worldwide. We have optimized our p-GaN and p-contact layer to get maximum EQE for our particular high In-content LEDs. This will be discussed in details later in this thesis.

LED efficiency

In LEDs, the electrical energy is converted to optical energy and like every energy conversion process, it generates energy losses. At different stages of the conversion and emission process, the efficiencies are termed differently. IQE (η_{IQE}) is defined as the ratio of the number of photons generated inside the QWs to the total number of electrons injected into the QWs [1]. When external current is applied, not all the carriers generated can really reach the active region. The effectiveness of carriers reaching the active region is described by the term injection efficiency η_{inj}. Hence IQE is actually [46],

$$\eta_{IQE} = \left(\frac{I_{radiative}}{I}\right)\left(\eta_{inj}\right)$$

Here, I is the total current fed to the LED, $I_{radiative}$ is the current associated with radiative recombination. However, all generated photons cannot leave the crystal finally. Particularly, those which hit the crystal surface at an angle equal to or larger than the critical angle will be reflected back to the crystal due to total internal reflection, and might be re-absorbed and lost. Considering this light extraction efficiency $\eta_{extraction}$, the EQE is finally [46],

$$\eta_{EQE} = \eta_{IQE} \cdot \eta_{extraction}$$

The wall-plug efficiency, η_{wpg} is defined as the ratio of optical output power P_{light} and the electrical input power $P_{electric}$ (=IV) [18],

$$\eta_{wpg} = \frac{P_{light}}{P_{electric}}$$

For GaN-based LEDs, the efficiency reduces at high operating current, a phenomenon which is called the "efficiency-droop". The origin of efficiency droop might be carrier delocalization effect [66], enhanced Auger recombination [67], and electron leakage [68]. The total current is actually the summation of carrier loss current I_{loss} and radiative current $I_{radiative}$ [45],

$$I_{total} = I_{radiative} + I_{loss}$$

The I_{loss} component comprises of defect-related SRH recombination current I_S and Auger recombination current I_A (both are associated with carrier loss inside the QWs). The current associated with carrier recombination outside the QWs is $I_{leakage}$. Hence, the total loss can be expressed as,

$$I_{loss} = I_S + I_A + I_{leakage} = I_{loss,QW} + I_{leakage}$$

The QW loss current $I_{loss,QW}$ can be expressed by the polynomial [9],

$$I_{loss,QW} = qV_{QW}(An + Bn^2 + Cn^3)$$

Where, V_{QW} is the active volume of all QWs and *A, B, C* are SRH parameter, radiative recombination parameter and Auger coefficient, respectively.

For commercial LEDs, we are concerned about luminous efficacy or lumen per watt (lm/W). The output power P_{light} can be expressed in terms of emitted photons [46],

$$P_{light} = \int \Phi(v).hv\,dv$$

Where $\Phi(v)$ describes the number of emitted photons at a given wavelength per time unit. The brightness of the LED can be measured taking the human eye sensitivity into account, and can be expressed as luminous flux [46],

$$\Phi = 683 \, \frac{lumen}{watt} \int V(\lambda)P(\lambda)d\lambda$$

Where, $V(\lambda)$ is the eye sensitivity and $P(\lambda)$ is the spectral power density in W/nm. Thus the luminous efficacy can be expressed in unit of lm/W.

1.5 Motivation and goal of the thesis

GaN-based light-emitting diodes (LEDs) have already been commercialized for solid-state lighting [2], since the tunable bandgap of InGaN/GaN MQW-based LEDs makes it possible to produce light in the entire visible spectral range [19]. Over the past decades, GaN growth on foreign substrates has been fairly optimized by growth techniques such as the use of AlN nucleation layer, low temperature GaN buffer layer [2], selective area growth (SAG) and epitaxial lateral overgrowth (ELOG) [46]. There are mainly two approaches to produce white light emission for lighting applications: the first involves monolithic integration of multi-chip red (R), green (G), and blue (B) LEDs and the other approach uses mostly cerium-doped yttrium-aluminum garnet (Ce:YAG), a yellow phosphor coating on the surface of blue LEDs [3,12] (Figure 19).

Figure 19: Generation of white light by monolithic RGB combination (left) and phosphor coating on blue LED (right) [Figure courtesy: Osram].

However, phosphor-based down-conversion, either full conversion or partial conversion of the primary blue light, results in low efficiency due to Stokes loss [4], and also yields low CRI [3], and poor colour temperature due to the little emission of red light from single phosphor [12]. Therefore, to obtain high efficiency and high CRI white light with better colour temperature, generation of white light by multi-chip monolithic RGB combination is necessary.

InGaN-based conventional blue LEDs have achieved IQE of 86.9% with light output power of 47.1 mW at 50 mA, developed by *Nichia*; IQE of more than 90% at 50 mA and 83% at ~300 A/cm^2, developed by *Osram*. III-phosphides (for example, AlInGaP system) based red LEDs have also reached high efficiency (EQE > 70%) [4]. On the other hand, green LEDs have achieved improved performance as well, recent report by UCSB has shown emission at 527 nm spectrum with 30% EQE at 20 A/cm^2 current density [69], and *Osram* has reported 540 nm emission with 50% EQE for converted green and 20% for direct green LEDs [12,70]. However, at typical LED operating current density of 100 to 300 A/cm^2, EQE of the true green (520 nm to 540 nm) LEDs are still below 20% and this so called "green-gap" (Figure 20) is the main obstacle to achieve phosphor-free white LEDs by RGB combination [4]. Over the past decades, efficiency improvement of blue and green LEDs has resulted in white LEDs with high luminous efficacy. In 2006, Narukawa *et al*. [71] reported white LED efficacy of 174 lm/W at a current density of ~2 A/cm^2 and 138 lm/W at a current density of 20 A/cm^2. Most recently reported white LEDs have luminous efficacy of 249 lm/W developed by *Nichia*, 215 lm/W with colour temperature of 3000 K, by *Osram*, and 303 lm/W at an injection current of 350 mA with a colour temperature of 5150 K, by *Cree* [12].

Figure 20: Maximum EQE of different commercial nitride and phosphide LEDs , illustrating the "green-gap" problem (spheres and stars are data points taken from [4,72–74]).

However, for intermediary wavelength green emission from InGaN-based MQW, the efficiency of devices with epitaxial structure grown in the commonly used +c-direction of GaN decreases with increasing indium content in the active region [6]. First, this phenomenon is due to the built-in piezoelectric field in the biaxially compressively strained InGaN quantum wells (QWs), which leads to a local separation of electrons and holes within the QWs (discussed in details in section 1.3.5), and consequently to a decreased emission efficiency due to a lower recombination probability between electrons and holes [6]. The second reason is the degraded InGaN crystal quality with high In-content due to In segregation that can change the potential profile of the InGaN/GaN MQW resulting in reduced overlap of electron-hole wave function [75]. Indium phase separation due to solid phase miscibility gap between GaN and InN is also an important factor for efficiency decrease in green-light-emitting devices [9].

InGaN QWs with a higher In-content are required to be grown at a lower growth temperature (~650 ^{o}C - 750 ^{o}C) which is not in favour of high InGaN crystal quality [7]. In order to minimize the polarization problem, non- or semi-polar LED structures could be a solution where selective area growth technique with optimized epitaxial growth parameters allows to grow stable semi-polar or non-polar facets [10]. However, good crystal quality, better In incorporation efficiency and fewer processing steps make (0001-Ga) direction growth still industrially interesting and optimized structure design to alleviate polarization and enhance optical emission regarding (0001) direction growth is still important. While the conventional InGaN MQW-based LED structures are grown on GaN buffer and use GaN as barrier layer, our objective has been to grow high In-content MQW with InGaN barrier on our novel so-called "semi-bulk" InGaN buffer. Silvaco TCAD simulation results predicted that if GaN was replaced by In$_{0.08}$Ga$_{0.92}$N on the n-side of the structure and for the barriers around the QWs, homogenous radiative rates and more homogeneous repartition of the carriers would be achieved compared to the structure with GaN on the n-side and GaN barriers [16]. While inhomogeneity of carriers and carrier overflow restricts the IQE of MQWs with GaN barrier and GaN buffer, homogenous radiative rates between 1×10^{26} cm^{-3}s^{-1} and 2×10^{27} cm^{-3}s^{-1} were calculated in the QWs with InGaN barrier and InGaN n-side [16]. In addition, the electron overflow is then strongly reduced leading to a strong increase of the IQE, reaching a value of 65% for a current density of 50 A/cm^2 [16]. However, epitaxial growth of reasonably thick InGaN buffer with single phase In and with good crystal quality is challenging. In this thesis work, the goal was to design, simulate, to grow by MOVPE and process LED structures with high In-content (15% -28%) in the QWs with InGaN barriers grown on a high quality InGaN buffer. The InGaN buffer was realized by "semi-bulk" approach instead of bulk

InGaN approach. The objective was, first to optimize the LED with blue (~450 nm) emission and then to push the emission wavelength to cyan and green spectra (up to ~520 nm) by adjusting the In-content in the MQW.

CHAPTER 2.   EPITAXIAL GROWTH AND CHARACTERIZATION TECHNIQUES

2.1   Epitaxial Growth: Metal Organic Vapour Phase Epitaxy (MOVPE)

MOVPE is a crystal-growth technology that allows the growth of layers of high quality semiconductor crystal with very precise thickness, composition control and reproducibility, in the nanometer range, even near atomic-layer precision. MOVPE is also known as MOCVD (Metal Organic Chemical Vapour Deposition) or OMVPE (Organo Metallic Vapour Phase Epitaxy) or OMCVD (Organo Metallic Chemical Vapour Deposition). In MOVPE technique, the liquid or solid metalorganic compounds which have fairly low vapour pressure can be used as gaseous precursor along with group-V hydrides by using bubbler and carrier gas technology. The up-scalability, excellent control, and relatively high growth rate (higher than MBE) have made MOVPE the first choice for III-nitride epitaxy in electronic and optoelectronic industries. The organometallic compounds of group-III metals and hydrides of group-V elements are transported in vapour phase into a reaction chamber where they react. The global reaction can be generalized as,

$$R_3M_{(gas)} + EH_{3(gas)} \rightarrow ME_{(solid)} + 3RH_{4(gas)}$$

Where M and E symbolize the group-III and group-V elements respectively, R is the type of organic radical (typically an alkyl) the group-III element is attached to, and H is elementary hydrogen. For example, GaN is typically formed by the reaction between trimethylgallium (TMGa) or $(CH_3)_3Ga$ and ammonia (NH_3),

$$(CH_3)_3Ga_{(gas)} + NH_{3(gas)} \rightarrow GaN_{(solid)} + 3CH_{4(gas)}$$

And the formation of $In_xGa_{1-x}N$ requires the additional precursor trimethylindium (TMIn) or $(CH_3)_3In$, together with TMGa and NH_3.

Typically, metalorganic (MO) precursors' temperatures of use range from -10 ^{o}C to 50 ^{o}C. Each precursor is stored in a sealed metal container called "bubbler". Within the bubbler, the precursor, either liquid or solid, remains at equilibrium with its vapour. Bubbler temperature is controlled by placing the bubbler in a temperature-controlled water or glycol bath. This temperature controls the liquid-vapour or solid-vapour equilibrium, hence the partial vapour pressure of the precursor in the bubbler. Elements like Oxygen (O), Sulphur (S) etc. would lead to a contamination in the epitaxial layers and Chlorine (Cl) could possibly change the growth regime and favour corrosion of the reactor metallic pieces and should therefore be avoided in the MO molecule [46]. The vapour pressures of some MOs used in this thesis work are shown in Figure 21.

The precursor molar flow rate Φ_m can be expressed in relation with the precursor partial pressure $P_{mo,partial}$, the total pressure P_{tot}, the bubbler temperature T, and the total volumetric flow of gas in the bubbler $\Phi_{v,tot}$,

$$\Phi_m = \frac{1}{RT}\frac{P_{mo,partial}}{P_{tot}}\Phi_{v,tot}$$

Where, R is the molar gas constant for ideal-gas. The units of molar and volumetric flow rates are $\mu molmin^{-1}$ and sccm (standard cubic centimeter per minute). Finally, the partial pressure of the precursor depends on the bubbler temperature according to following equation,

Figure 21: Temperature dependent vapour pressure data of some metalorganic precursors used in this thesis work (after [17]).

$$P_{mo,partial} = 10^{a-\left(\frac{b}{T}\right)}$$

The values of the parameters *a* and *b* for the organometallic precursors used in this thesis work are given in Table 5.

Table 5: Parameters for computation of the partial pressures of metalorganic precursors [49]

Precursor	*a*	*b* (K)	Boiling temperature (°C)	Melting temperature (°C)
TMGa	8.07	1703	56	-15
TMIn	10.52	3014	134	88

Hydride precursors of group-V elements are typically gaseous at room temperature and atmospheric pressure. The amount of those elements is controlled by controlling the precursor gas flow injected into the main stream of carrier gas H_2 and / or N_2. From the calculated debits of precursors flow rates, the V/III ratio and the III/(III+V) ratio can be calculated.

The basic components of an MOVPE system are (Figure 22) [46]:

- Channels connected with metalorganic sources that provide the controlled flow of a carrier gas carrying an intended amount of precursor material. The carrier gas can be switched from the bubbler to the by-pass channel in order to keep the carrier gas flowing in a stand-by mode.

Figure 22: General schematic of an MOVPE system [46].

- Channels and sources for the controlled flow of required group-V hydrides.

- For each source, automatic (2/3/5-way) valves, allowing access either to the reactor chamber or to the vent line. The switching is optimized so that the gas

flow coming from a precursor source is stable all along the period of use of the precursor.

- Reactor chamber (horizontal or vertical) usually made of quartz or surrounded by quartz or stainless steel, where the epitaxial growth takes place. This chamber is fed by precursor gases and also by inert carrier gases.

- Programmable logic control (PLC) unit with software that controls the gas and precursor flows and injection timing, the temperature and the pressure. The flow of the carrier gas is controlled by electronic mass flow controllers (MFCs). The carrier gas can be switched from the bubbler to the by-pass channel in order to keep the carrier gas flowing in a stand-by mode [46].

- Vacuum system (pump, pressure controller, valves etc.) to control and stabilize the pressure during growth.

- Exhaust system where the toxic exhaust gases are purified to remove any toxic fractions before releasing it to the atmosphere.

- A susceptor in the reactor chamber (usually made of graphite with SiC coating) where the substrate is placed and the epitaxial growth takes place on the substrate.

The growth rate explicitly depends on the reactor temperature and can be related to three temperature regimes [46]. In the low temperature regime, the growth rate is limited by the chemical reaction (decomposition or desorption on the surface) rate which depends on the temperature according to the Arrhenius law: $R = Ae^{-E_a/kT}$, where A is the pre-exponential factor, R represents the chemical reaction rate, E_a is the activation energy, k is Boltzmann constant and T is the temperature in K. In the medium temperature range (800 $^{\circ}$C to 1200 $^{\circ}$C for GaN epitaxy from TMGa and

NH$_3$), the growth rate is dependent on precursor supply and almost independent of temperature. Growth in MOVPE reactors takes place in this so called "mass transport limited" regime [46]. For the epitaxy of most III-V compounds, including GaN, since group-V elements are much more volatile than group-III ones, the growth rate is mostly controlled by the partial pressure of group-III elements in the reaction chamber. In the high temperature regime (>1200 ^{o}C), thermodynamic factors, such as desorption and dissociation of the crystals, tend to limit the growth rate with increasing temperature. In order to grow the epi-layers stoichiometrically, it is necessary to control the ratio of the precursors, e.g. V/III ratio.

Figure 23: Growth rate (log scale) as a function of inverse temperature (schematically).

2.1.1 *Basic growth principle*

The epitaxial growth in MOVPE is governed by diffusion processes that rely on the vapour transport of precursors in a heated zone, and it is conducted under near thermodynamic equilibrium conditions [44]. After the carrier gas being mixed with vapours of the precursors and being transported close to the heated substrate surface, surface chemical reactions take place. The schematic of different reactions during III-nitride epitaxial growth process is illustrated in Figure 24.

Figure 24: Illustration of epitaxial growth by MOVPE [44].

The heated organic precursor molecules then decompose in the absence of O_2 or any halogen (pyrolysis) [44]. The resulting species diffuse through the boundary layer to the growth surface and attach onto the substrate by physisorption [44]. The species can desorb, migrate, or react with other surface species at this moment. To form a new layer, the species can diffuse on the surface and bound tightly at the bottom of a growth step, or nucleate at other positions to form islands [44]. The by-products from the chemical reactions are flowed out of the reaction zone to the exhaust by the carrier gas. There are also parasitic reactions that take place between precursors in the gas phase that can reduce the incorporation efficiency. Moreover, the particles of the by-products may fall on the substrate surface and thus impede the formation of single crystal and therefore degrade the crystal quality.

MOVPE growth includes mass transport, hydrodynamics, thermodynamics and kinetics. Typically, the growth rate and the quality of the III-nitride epitaxial layers depend mainly on four parameters: temperature, pressure, V/III ratio (the ratio of NH_3 flow rate to the total flow rate of III and V precursors) and total group-III flow. Moreover, the choice of carrier gas (H_2 or N_2) has also an impact on the growth result.

Growth temperature should be optimized. Sufficient growth temperature is required to give enough energy for the pyrolysis of precursors, the diffusion of the atoms on the substrate surface and activation of the reactions which controls the growth rate and surface structural properties. However, too high temperature can initiate desorption and decomposition. In addition, growth temperature also affects the amount of indium incorporation in III-nitride alloys, such as, in our case, in InGaN. To reduce the parasitic reactions, the growth pressure is kept low (15-400 mbar) [76]. For low V/III ratio, background doping would be increased possibly due to nitrogen vacancy which acts as an acceptor [29,77,78]. On the other hand, for high V/III ratio, parasitic reactions would be aggravated and surface mobility of adsorbed atoms would be hindered.

For GaN growth, H_2 is used as carrier gas because it has good thermal conductivity, enables faster diffusivity of precursor species and has better carbon-radical furbishing properties compared to those of N_2. However, for InGaN growth, N_2 is used since the presence of H_2 enhances indium desorption. Moreover, in H_2 environment, Mg-H complexes are formed during the growth of Mg doped p-type GaN.

2.2 Experimental Setup

2.2.1 T-shape MOVPE reactor

The samples for this thesis work were grown in a T-shape MOVPE reactor [76]. The design of this reactor is a combination of vertical loading and horizontal quartz tube: allowing the advantage of laminar flow along with loading distribution vertically. The schematic of the T-shape reactor chamber is shown in Figure 25.

Figure 25: Schematic structure (cross-section) of the T-shape MOVPE reactor chamber.

An RF induction-heated graphite susceptor is used to heat samples up to the target temperature (for example, 1040 ^{o}C for typical GaN growth). Several numbers of thermocouples are set around the reactor chamber to measure temperatures of different zones. A high vacuum and pumping system controls the pressure inside the reactor between 60 torr to 750 torr.

Photographs of the actual reactor and reaction chamber are given in Figure 26.

a) reactor quartz tube

b) complete reactor with gas panels and bubblers

Figure 26: Photographs of the reactor quartz tube (a) and the complete T-shape MOVPE reactor with gas panels (b).

An *Epieye*[®] reflectometry setup was used to i*n-situ* monitor epi-layer thickness during the growth. The principle is to measure the intensity of a laser beam that is reflected off the sample.

Figure 27: Typical *in-situ* reflectometry for GaN growth by MOVPE.

This intensity oscillates over time as a result of interferences because of the difference of the refractive index between the nitride films and the sapphire substrate (Figure 27). The laser of 633 nm wavelength is placed vertically on top of the metal cover of the reactor. The growth rate can be calculated by the following equation,

$$growth\ rate = \frac{\lambda}{2n\varDelta t}$$

Where, λ is the wavelength of the laser beam, n is refractive index of the epi-layer and $\varDelta t$ is the time interval between two maxima or two minima of oscillations.

The intensity of the laser reflection is the measure of the film quality as well, governed by the equation [44],

$$R = R_o e^{-(4\pi\sigma/\lambda)}$$
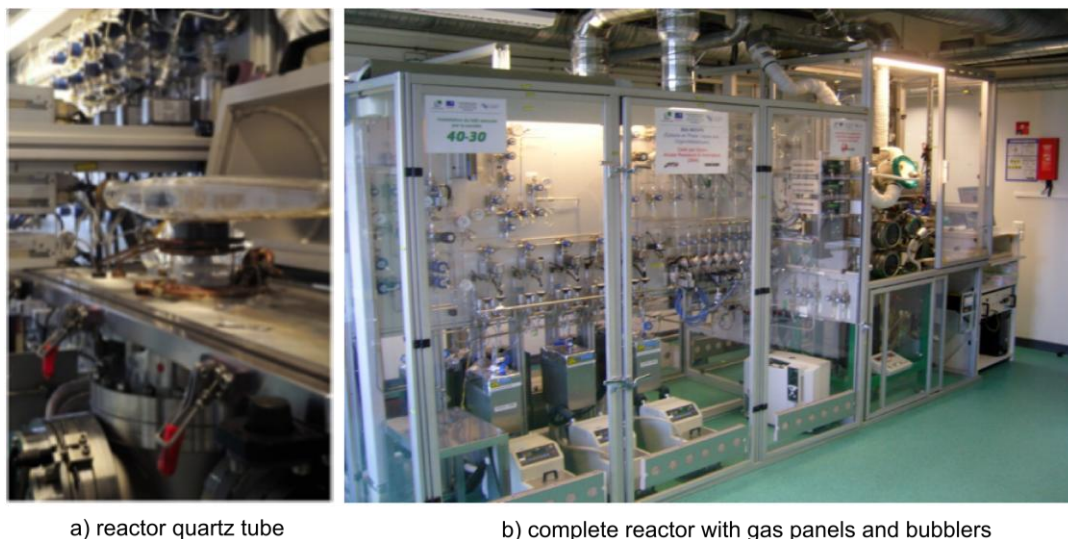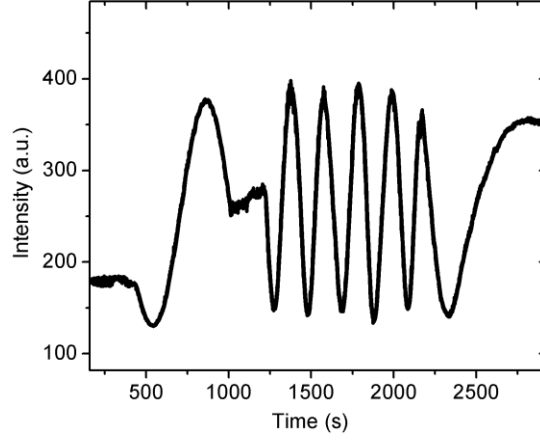
74

Where R is the mean value of reflectance oscillations, λ is the used wavelength and σ refers to the root mean square of roughness. A reduction of the ratio between maxima and minima of the reflection intensity indicates the increase of surface roughness. Detail of the T-shape reactor can be found in [76].

2.2.2 *Aixtron*® *Close Coupled Showerhead (CCS) 3 × 2" reactor*

The *Aixtron*® CCS reactor was used basically to grow the GaN templates on sapphire substrates. Moreover, growth optimization of some of the MQW structures was also carried out in the CCS. The sketch and actual photograph of the CCS reactor in our lab are shown in Figure 28.
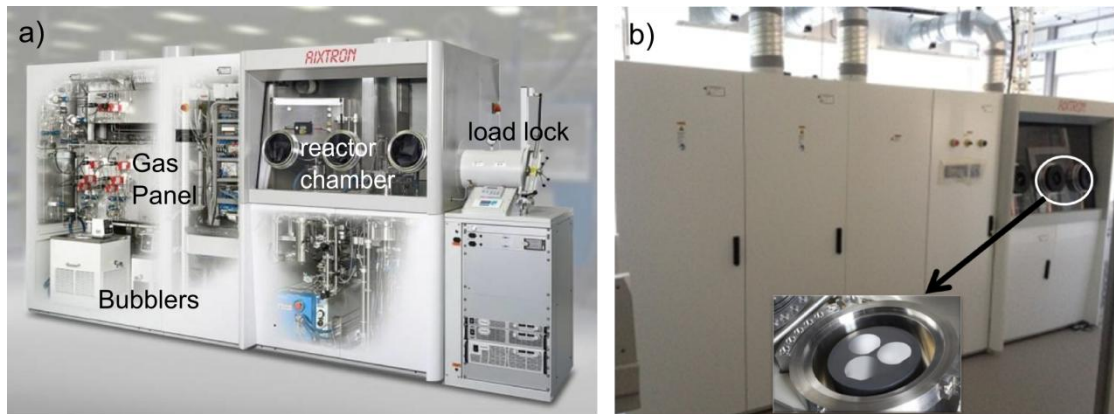
Figure 28: Sketch of *Aixtron*® CCS 3 × 2 inch reactor (a) (courtesy: Aixtron) and the photograph of *Aixtron*® CCS reactor system in our lab (b).

The surface temperature of substrates in this reactor can reach up to 1300 °C. The growth rate of GaN is controlled principally by mass transport to the substrate as well. The showerhead reactor is an intrinsically very uniform reactor - practically and in simulation and the showerhead design avoids jetting or turbulence, and minimizes pre-reactions[2]. The *in-situ* sensor is the *Laytec*® *epiTT* system that measures reflectance at three wavelengths (950 nm, 633 nm and 405 nm) and monitors the

---

[2] www.aixtron.com

75

growth process and properties of growing layers such as growth rate, film thickness, stoichiometry changes, and morphology.

2.3 Characterization techniques

Various morphological, material, optical and electrical characterizations are required to measure the epitaxially grown thin film quality and device performance.

In this thesis work, high resolution X-ray diffraction measurements were performed in a *Panalytical X'pert Pro MRD* system with Cu-Kα radiation (Cu-Kα_1: 1.5405 Å). The height of X-ray beam from hybrid monochromator was 1.2 mm and the resolution was ~ 12 arcsec. Generally, in this thesis work, symmetric (002) and asymmetric (102) omega (ω) or rocking curve scans, symmetric (002) 2theta-omega (2θ-ω) scans and asymmetric (114) reciprocal space mapping (RSM) were carried out by XRD to investigate the material quality, percentage of In incorporation in InGaN layers and relaxation amount of InGaN layers on GaN for MQWs and "semi-bulk" (SB) InGaN layers.

The atomic force microscope images in this thesis work were obtained by *Veeco 3100 Dimension* atomic force microscope in tapping mode.

The scanning electron microscope images were obtained by *Zeiss supra TM 55VP*. The main elements of the SEM equipment were: electron source, magnetic focusing lenses, the sample vacuum chamber, imaging system and control panel.

In this thesis work, a cathodoluminescence spectroscopy integrated with SEM system was used to study the optical properties of the samples. Both room-temperature (290 K) and low-temperature (77 K) CL investigations were performed in the digital SEM. The CL emission was detected by a parabolic mirror collector and

analyzed by a spectrometer with a focal length of 320 mm using a 1200 grooves/mm grating and a spectral resolution of 0.06 nm. The signal was then recorded by a liquid N_2-cooled *Horiba Jobin Yvon Instruments Symphony* 1024×256 CCD detector [79].

Low temperature (15 K) PL was used to identify the MQW emission and also to calculate the room temperature IQE by taking the ratio of integrated intensities at room temperature (290 K) and at 15 K. Temperature-dependent PL spectra were measured in a helium cryostat (vacuumed at 2 - 4 mbar) at temperature from 15 to 300 K using a 375 nm diode laser as excitation source. The excitation power was varied from 0 to 48 mW and the excitation beam diameter was 100 μm. To avoid wafer non-uniformity, similar points at the center region on the wafers were measured in the PL study.

SIMS experiments were carried out to find out the impurity concentration (such as H, C, O), as well as Ga, In and, most importantly, the Mg concentration in our p-GaN layers. The primary ions were O_2^+ and Cs^+. The impact energy, sweep area and analyzed surface diameter were 3 keV, 125×125 μm^2, 30 μm, respectively for Mg, In, and N detection; and 14.5 keV, 40×40 μm^2, 30 μm, respectively for H, C, O, Si, and Ga detection. H, C and O were analyzed via the detection of negative ions with sputtering cesium (Cs). For silicon, medium mass resolution conditions were necessary to avoid mass interference between ^{28}Si and ^{14}N$_2$. Mg, In, Zn and Al were analyzed in MCs$^+$ mode. Mg was taken up by sputtering to have a better detection limit. Deep calibration was obtained from the measurement of the craters by profilometry with stylus. The variation in speed of sputtering between the different materials was taken into account. Quantification of H, C, O and Si was obtained from

our previous standards in the same session. A gold deposit prevented charging problems on the samples.

By Hall measurement (van der Pauw method), the carrier concentration (Hall concentration), carrier mobility (Hall mobility) and the resistivity of the n-GaN and p-GaN layers were measured.

All high angle annular dark field images presented in this dissertation were taken at laboratory of photonics and nanostructures (LPN), Paris, using a dedicated aberration-corrected *JEOL 2200FS* scanning transmission electron microscope. The electron-beam acceleration voltage was 200 kV, the current was 150 pA and the probe size was 0.12 nm at FWHM. All the STEM images were taken perpendicular to the $\langle 1\,1\,\bar{2}\,0 \rangle$ zone axis. Electron dispersive X-ray spectroscopy was carried out in the same microscope using the same probe conditions as for imaging. Quantitative measurements of the indium composition from the EDX spectra were obtained from the intensity ratio of the *Lα* line of indium (3.290 keV) to the *Kα* line of gallium (9.770 keV). The acquisition time for each EDX spectrum was 60 s. The EDX spectra were acquired using a *JEOL 2300D* detector and the accompanying *JEOL* software [28].

CHAPTER 3.   DESIGN AND SIMULATION OF MQW AND LED STRUCTURES

3.1   Simulation method

The LED structures were simulated by commercial Silvaco TCAD software by Atlas. The self-consistent Schrödinger-Poisson solver with drift-diffusion carrier transport model was used for calculating quantum well bound state energy. The band structures, wave functions and spontaneous emission rate were obtained by developing effective mass approximation using the *k.p* theory [80]. The interface and surface charge and carrier screening effects were considered and material parameters were taken after Bernardini and Fiorentini *et al.* [53]. The band offset was calculated for InGaN/GaN or InGaN/InGaN interfaces by different affinity values calculated for different In contents for InGaN well and GaN or InGaN barrier [80]. The screening of polarization by dislocations and free-carriers was considered to be 30%, which was a value taken based on the result of excitation power dependent PL experiment and literature [81–83]. The n-GaN and p-GaN doping were 1×10^{19} cm^{-3} and 1×10^{19} cm^{-3} (typical values in our experimental samples). The InGaN well, barrier and buffer were considered as unintentionally doped with doping concentration of 1×10^{17} cm^{-3}. The electron and hole mobility were 200 cm^2/V.s and 8 cm^2/V.s, respectively [80]. The Shockley-Read-Hall (SRH) carrier lifetime was set to 30×10^{-9} s [84,85]. For GaN, the radiative recombination rate was set to 1×10^{-11} cm^3/s, the Auger coefficient for electron and hole was 1×10^{-31} cm^6/s [84,86]. The valence band and conduction band degeneracy factors were both 2, the acceptor and donor energy levels were 0.2 eV and 0.03 eV, respectively [80]. The electron effective mass was taken to be $0.2m_o$ [87] and

the hole effective mass was m_o, where m_o is the free electron rest mass (= 9.11×10^{-31} kg). The temperature was 300 K for all temperature-dependent equations. The simulation was carried out for a bias from 0 V up to different final voltages of 1 to 6 V with a step of 0.1 V. The current density was up to 1000 A/cm^2, covering the typical LED operating current density of 30 to 200 A/cm^2. Moreover, the difference in indium (In) content was very small in the three comparing LED structures leading to very similar current densities for the three structures for the same voltage.

The internal quantum efficiency (IQE) was defined as $R_{rad} /(R_{rad} + R_{non\_rad})$ [80]. The radiative rate (R_{rad}) is the total radiative rate which mostly comes from the quantum wells and the non-radiative rate (R_{non_rad}) is the sum of SRH and Auger recombination rates. The simulation parameters and the positions of the discrete energy levels of electrons and holes inside the QWs were validated in previous work [16].

3.2   Simulation of LED structures

Our final designed LED structure was simulated along with comparable reference structures. The structures simulated in Silvaco are shown in Figure 29. Structure A had In$_{0.15}$Ga$_{0.85}$N MQW structure with GaN barrier on ~70 nm thick GaN buffer, and structure B and C both had In$_{0.15}$Ga$_{0.85}$N MQW with In$_{0.05}$Ga$_{0.95}$N barriers whereas structure B was on ~70 nm thick GaN buffer and structure C was on ~70 nm thick "semi-bulk" In$_{0.05}$Ga$_{0.95}$N buffer. The well thickness was chosen to be 3 nm as per our previous work [16], considering that well thickness thicker than this will provide difficulties in hole transport and increase QCSE [88–90]. Our previous simulation work showed no change in IQE for barrier thickness of 5 nm to 10 nm range for MQW on InGaN buffer, hence 5 nm barrier has been chosen to avoid In

Figure 29 : The simulated LED structures: reference structures a: with GaN buffer and GaN barrier (sample A), b: with GaN buffer and In$_{0.05}$Ga$_{0.95}$N barrier (sample B); and final structure c: with "semi-bulk" In$_{0.05}$Ga$_{0.95}$N buffer and In$_{0.05}$Ga$_{0.95}$N barrier.

segregation related defects in our InGaN barriers. All the three structures had 250 nm p-doped GaN on top of the MQW separated by 2 nm GaN cap.

3.2.1   Simulation and comparison of InGaN barrier and GaN barrier

First, the MQW structures with GaN barrier and InGaN barrier were compared to investigate the effect of indium in barrier layer on efficiency and wavelength of InGaN MQW. Moreover, the effect of InGaN barrier on the emission wavelength and intensity of MQW structure with and without InGaN "semi-bulk" buffer particularly for intermediary wavelength "green-gap" spectra emission was studied. The optimum In content in the barrier was obtained from simulation. Figure 30 shows the room temperature IQE and *I-V* curves for different In content in a 3-period MQW with 3 nm well and 5 nm barrier. The best IQE was observed for 5% In in the barrier. In content more than this resulted in deterioration of IQE modeled by more leakage

observed above 5% of In in the barrier, because of lack of confinement. In experimental result, consistently, indium content more than 5% caused worse crystal
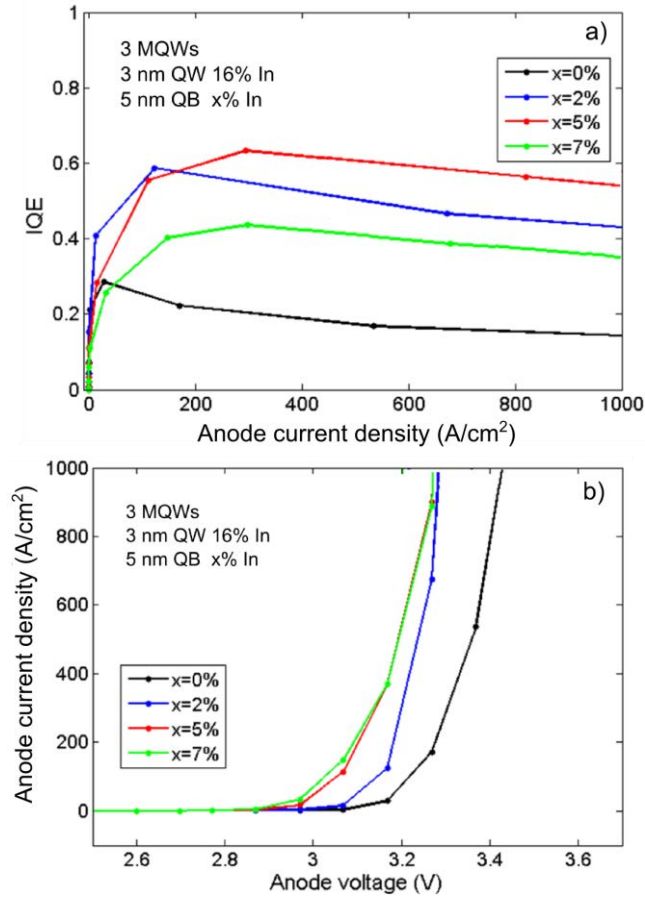
Figure 30 : Effect of different In contents in the barrier: IQE (a) and *I-V* curves (b).

quality due to In desorption at InGaN growth temperatures of 780 - 800 $^{\circ}$C, leading to more structural defects related non-radiative recombination centers [91]. The turn-on voltage was ~0.1 V lower in the case of 5% In in barriers compared to that for GaN barriers (Figure 30b).

Simulation was performed for different numbers of quantum wells for sample A with GaN barriers and sample B with $In_{0.05}Ga_{0.95}N$ barriers. The comparison of IQE is shown in Figure 31 and *I-V* characteristics in Figure 32. InGaN barrier gives ~170% improvement of IQE for 3 QWs at current density of 200 Acm^{-2}.
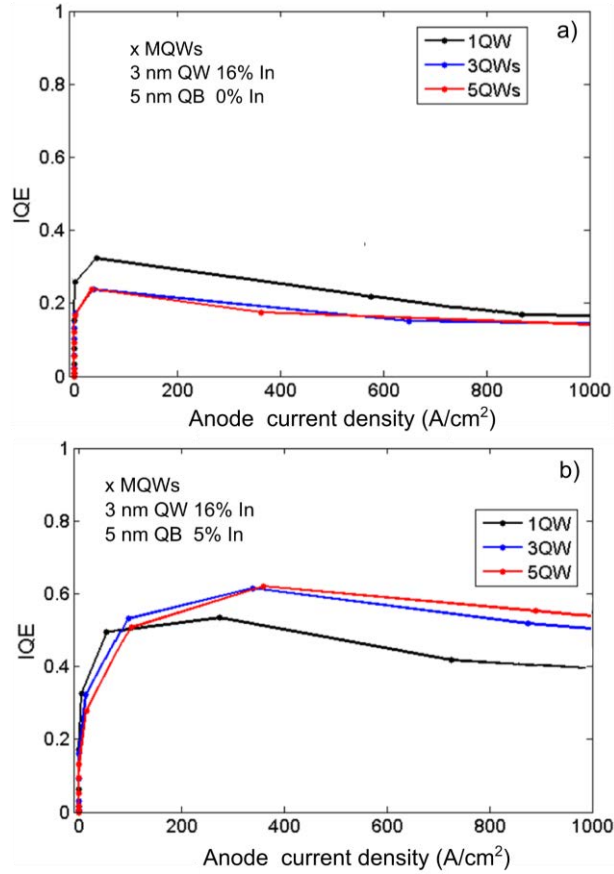
Figure 31 : Simulated IQE comparison of sample A with GaN barrier (a) and sample B with In$_{0.05}$Ga$_{0.95}$N barrier (b).

Multiple QWs are required to get maximum radiative output. However, 3 to 5 is the optimum number of QWs to get the maximum efficiency, number of QWs greater than this might increase defect formation by strain relaxation. The turn-on voltage has also improved for InGaN barrier (Figure 32) and is lower than 3 V for optimal number of QWs. Since, the luminous efficacy is the ratio of the light output power to the electrical power consumed (=*IV),* this lower turn-on voltage will increase the luminous efficacy for the same light output power. This improvement in turn-on voltage is attributed to the improved hole injection or the more transfer of holes from the last QW (nearest the p-side) to the next ones due to reduced potential barrier [92]. To further investigate the improved IQE for MQW with InGaN barriers, the calculated radiative recombination rates were plotted and compared.
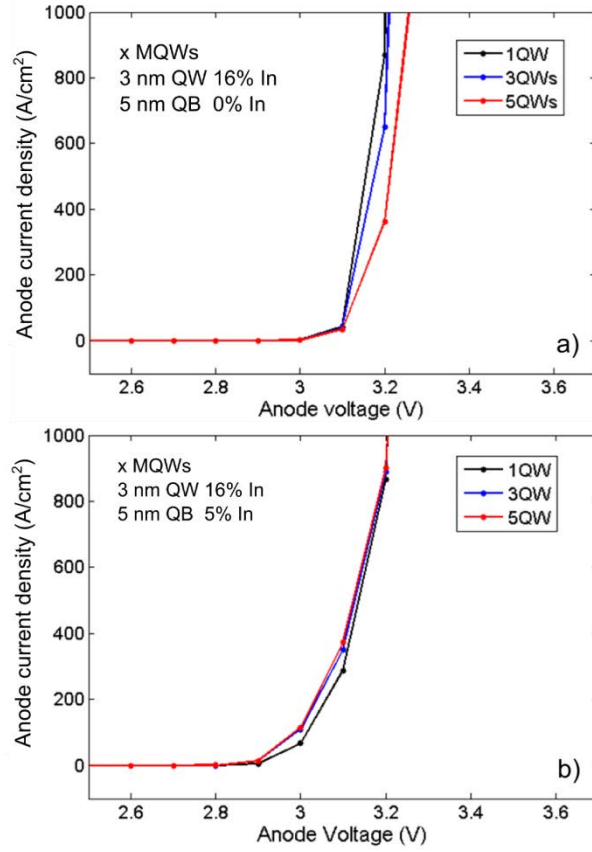
Figure 32 : Simulated *I-V* curves for sample with GaN barrier (a) and In$_{0.05}$Ga$_{0.95}$N barrier (b).
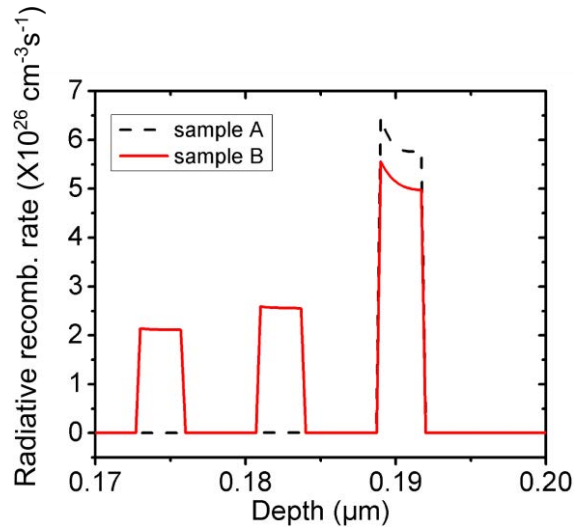
Figure 33: Simulated radiative recombination rate in MQW with GaN barrier (sample A) and In$_{0.05}$Ga$_{0.95}$N barrier (sample B).

Figure 33 shows the radiative recombination rate for sample A and sample B. With

InGaN as barriers, radiative recombination takes place in all the wells rather than

mostly in the last (closest to the p-side) and the total radiative recombination rate

increases by $\sim 5.8 \times 10^{26}$ cm^{-3}s^{-1}. Figure 34 shows the electron and hole concentrations
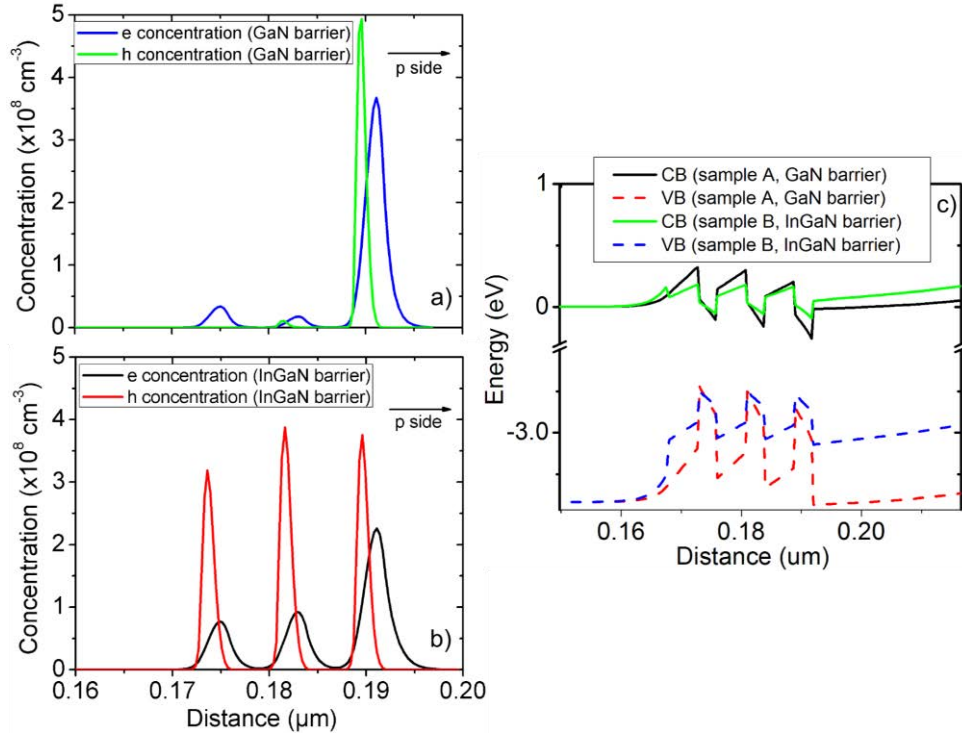
Figure 34 : Simulated electron and hole concentrations for MQW with GaN barrier (a), with In$_{0.05}$Ga$_{0.95}$N barrier (b) and band diagram comparison for MQW with GaN barrier and In$_{0.05}$Ga$_{0.95}$N barrier (c).

for GaN barrier (Figure 34a) and for InGaN barrier (Figure 34b) in the otherwise

same MQWs. It can be easily observed that the electrons are more uniformly

distributed in all the wells and the total electron concentration has also increased for

InGaN barrier. Moreover, in the MQW with GaN barrier, holes are only gathered in

the last QW (closest to the p-side) due to the depth of the confined levels. In contrast,

in the MQW structure with InGaN barrier, due to lower potential barrier height, holes

are evenly distributed in all the wells (Figure 34b).

Due to the higher effective mass of the heavy holes, there are discrete levels only for

the holes. For electrons, there is more some kind of continuum of states located over

the top of the MQW structure. This electrons can escape easily and result high leakage, specially at high current density [93]. Absorption dominates in this continuum of states and emission occurs in the localized states of lower energy , and this causes the difference in emission and absorption spectra which is the so called Stokes shift [94].

In the simulated band diagram, shown in Figure 34c, the band offset is smaller for InGaN barrier and this reduced energy barrier for holes is the cause for more uniform carrier distribution in wells. This homogeneous distribution results in reduced overflow of the electrons that can recombine radiatively in all the QWs. There is more overlapping of electron-hole wave function and consequently more radiative recombination.

3.2.2 Simulation of improvement of optical emission and efficiency-droop of InGaN/InGaN multiple quantum well grown on "semi-bulk" InGaN buffer

As discussed in the previous paragraph, InGaN barriers improve the IQE. InGaN on the n-side as buffer will also improve the IQE [16]. However, it is difficult to grow good quality reasonably thick InGaN buffer in epitaxy. In this thesis work, we proposed the use of InGaN "semi-bulk" layers for the growth of high quality InGaN buffer layer, in addition to InGaN barriers in MQW. The SB structure on a standard (STN) n-GaN template is schematically shown in Figure 35. This "semi-bulk" approach (4 periods of 15 nm InGaN and 2 nm GaN layers in between two successive InGaN layers) for InGaN growth allows to have a higher quality thick InGaN buffer compared to bulk InGaN [95]. In such SB buffer, the inserted thin GaN layer between two successive InGaN layers absorbs excess In and helps to avoid phase separation and quality degradation of the final thick InGaN buffer [95].
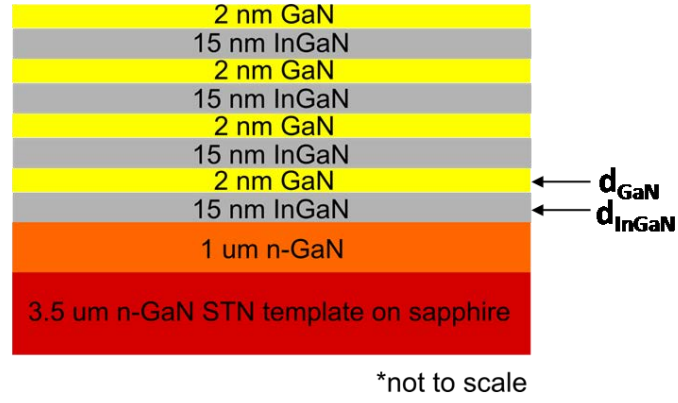
Figure 35: Schematic of the "semi-bulk" InGaN structure.

The thickness d_{InGaN} of the InGaN layer was chosen based on the previous simulation and experimental works, and estimated from HAADF-STEM images [28,96]. This thickness was the thickness for which the 2D to 3D growth transition just started in our bulk InGaN calibration samples. The GaN interlayer thickness was thin enough to allow carrier transport through tunneling and estimated by numerical simulation done by previous colleagues in our lab [28,96]. In this thesis work, the number of period was 4 to keep the total InGaN SB thickness below critical thickness to avoid relaxation. The estimation of the critical thickness was taken from previous studies [28]. To reduce strain induced piezoelectric field, it might be interesting to make the InGaN buffer sufficiently thick to be relaxed on the GaN template underneath. However, the relaxation of the InGaN buffer and the MQW on top could induce misfit dislocations that could act as non-radiative recombination centers. This has detrimental effect on light-emitting device performance. This type of behaviour was also observed in the InGaN/GaN superlattice prelayer study of W.C. Lai *et al.* [97]. Recently, a strain-relief InGaN underlayer has been employed by several groups [98,99] to reduce the compressive strain when growing InGaN/GaN MQWs pseudomorphically. M. J. Davies *et al.* [98,100] reported a blue-shift by using a 24 nm thick Si-doped InGaN (5% In) interlayer which was well below critical

thickness and concluded that the decrease in built-in electric field and hence decrease in QCSE were responsible for this shift. On the other hand, D. M. Van Den Broeck *et al.* [101] reported the realization of a fully relaxed 180 nm thick InGaN (8% In) with good surface quality (realized by periodic growth of 2 nm GaN / 20 nm InGaN, followed by an anneal at 1000 °C) and grew an InGaN/GaN MQW on this buffer for balancing strain and reducing piezoelectric field [99]. Y. Xia *et al.* [102] reported neither a wavelength shift nor any strain relaxation when using a 130 nm bulk InGaN prelayer prior to InGaN/GaN MQW emitting in green spectrum and they attributed their improved light output power to the "optical or excitonic excitation-transfer" to the MQW when the excitation reaches the underlayer. Since relaxation of the active region would cause significant material degradation and inhomogeneous In composition [97,100], and a relaxed InGaN buffer layer would have worse material quality due to In phase separation, we proposed to grow an active region with minimum or no relaxation, emitting in blue-green spectra on a fully-strained InGaN (5% -12% In) buffer layer on n-GaN.
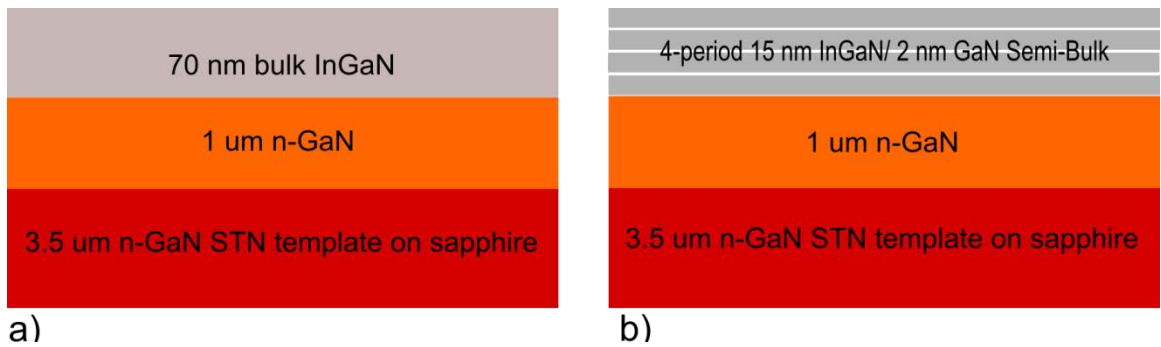
Figure 36: Structure comparison of bulk InGaN (a) and "semi-bulk" InGaN (b).

Since, the bulk InGaN has inferior material quality and surface with more clusters, inclusion defects and higher RMS roughness from AFM scan than those of the "semi-bulk" InGaN [28,95], the InGaN buffer layer was grown using "semi-bulk" approach

[95] to obtain a high quality single phase InGaN layer. Figure 36 schematically shows the comparison between bulk and "semi-bulk" InGaN buffer structures.

According to the simulation studies, the In content required in the "semi-bulk" buffer was around 5-7% for a well In content of 15-16% to get emission in ~460 nm spectrum and 12-15% for a well In content of 25-28% to get emission in ~520 nm spectrum. The InGaN SB buffer was investigated to achieve the optimum In content and thickness. The "critical thickness" limits the thickness of the epitaxially grown bulk InGaN layer [28], however, by "semi-bulk" approach, good quality thicker InGaN templates with higher In content can be grown [28,95] .
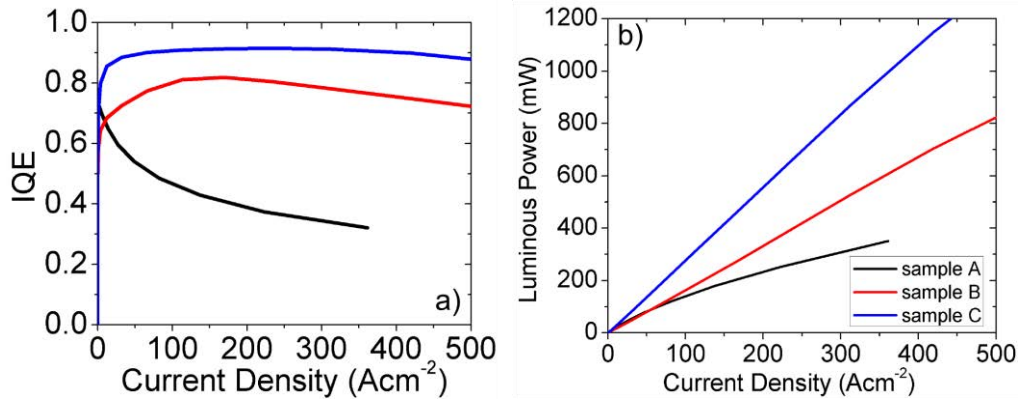
Figure 37 : Calculated IQE (a) and luminous power (b) comparison of sample A, sample B and sample C.

We have shown that the simulation predicts improvement of optical output power and reduction of efficiency-droop at blue to green emission wavelength (450 nm to 520 nm) for our designed InGaN/InGaN MQW structure on InGaN SB buffer (sample C, Figure 29). Internal quantum efficiency and luminous output power were calculated and plotted. They are shown in Figure 37. At a current density of 200 A/cm^2, 130% improvement of room temperature IQE, compared to that of sample A, and 15% compared to that of sample B have been obtained (Figure 37a). Moreover, there is no

predicted efficiency droop for sample C at this current density, in contrast to sample A and B. The calculated luminous power for sample C is doubled compared to sample A and ~60% improved compared to sample B at the same current density (Figure 37b).
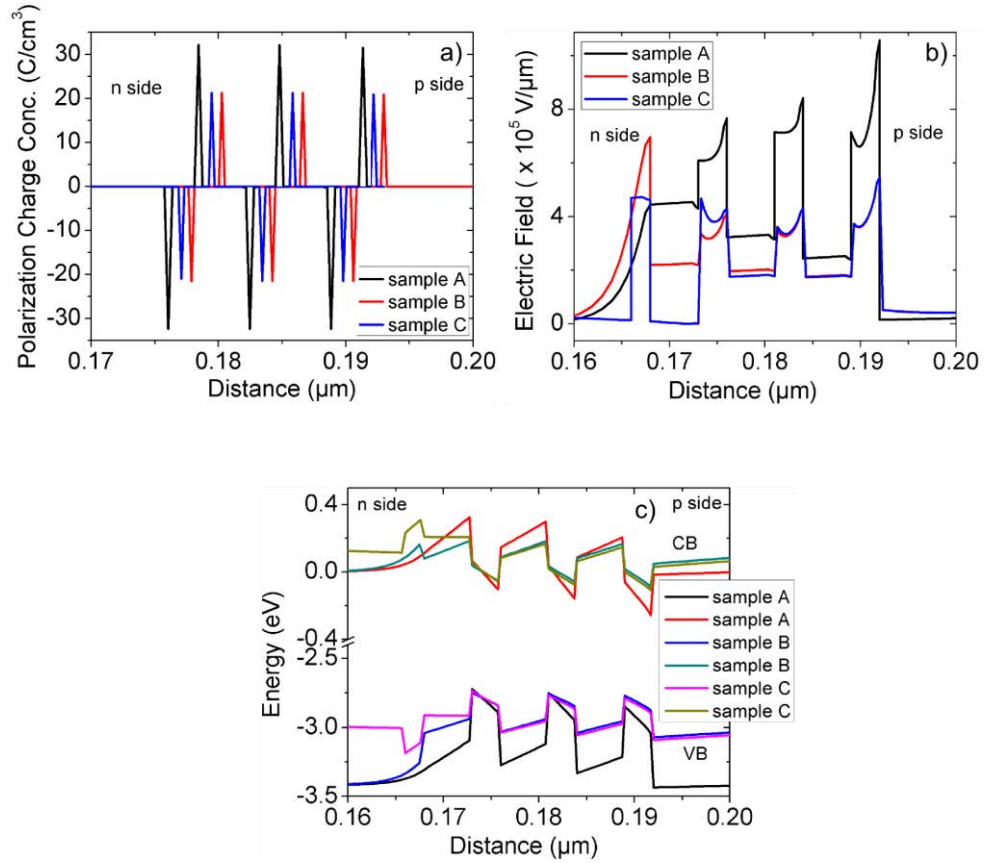
Figure 38: Polarization charge concentration (a), internal electric field (b) and valence and conduction band structure (c) for the samples under study. Please note that, in (a), the distance scale has been shifted for sample A and B for better visibility.

This predicted improvement is attributed to the reduction of net electric field in sample C. Use of InGaN as barrier reduces the polarization charge (Figure 38a) and also the built-in electric field (Figure 38b). It was also due to a better repartition of the holes in the quantum wells. Further reduction in the average electric field in the three wells was mainly due to the use of SB InGaN buffer, because the reduction of the spontaneous polarization in the buffer and of the piezoelectric polarization in the

wells reduces the net built-in electric field [103]. For sample C, 1.5 times lower electric field was calculated compared to sample A and the average electric field in the wells was 0.1 MV/μm weaker compared to that of sample B (Figure 38b).
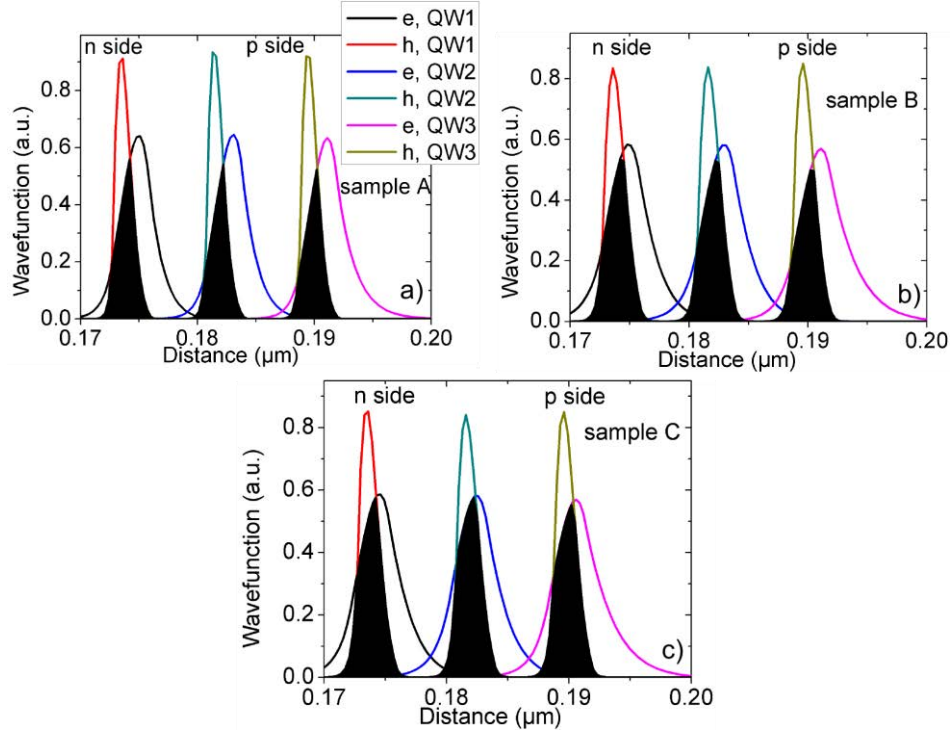
Figure 39: Electron-hole wave function overlap for reference sample A (a), reference sample B (b), and our final structure sample C (c).

The polarization charge concentration was half in the structure with InGaN barrier (sample B), as shown in Figure 38a compared to that of the reference structure (sample A). Hence, the reduction in polarization charge has direct impact on the improvement of IQE.

The reduction in net electric field when using SB InGaN as buffer resulted in reduced band bending (Figure 38c). As a result, the QCSE was reduced and there was more overlap of electron-hole wave function (Figure 39) for the final structure of sample C. In fact, 38.7% more overlap compared to sample A and 9% more overlap compared to sample B was obtained.

Simulation of 3 QWs with different well thickness and In content of 20% in well and 10% in barrier and in "semi-bulk" InGaN showed the best result of 72% IQE at 250 A/cm^2 driving current for a well thickness of 3 nm (Figure 40). However, the efficiency drops beyond 4 nm of well thickness where the longer wavelength related droop phenomenon dominates, which recovers a bit at 6 nm width due to the increase of active region volume.
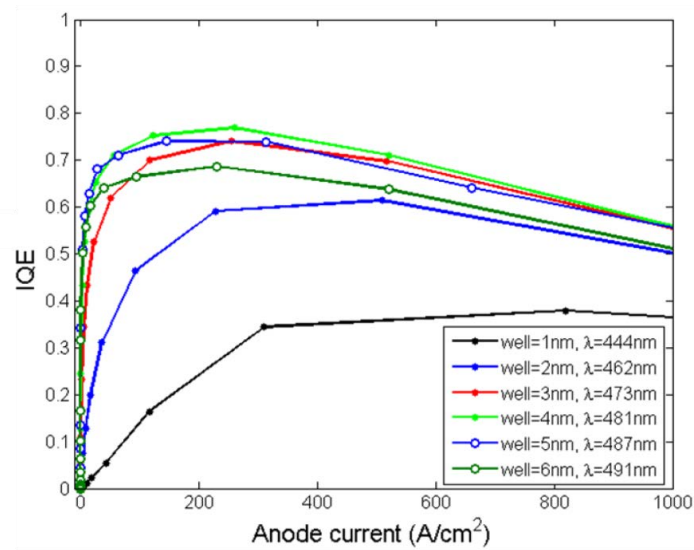
Figure 40 : Simulated IQE for different well thicknesses for a MQW with 20% In in well and 10% In in barrier and in "semi-bulk" InGaN.

CHAPTER 4.   EPITAXIAL GROWTH AND

CHARACTERIZATION OF MQW AND LED STRUCTURES

4.1   Final design of LED on InGaN "semi-bulk"

Based on the simulation result discussed in CHAPTER 3, final design of our final LED structure for epitaxial growth consisted InGaN SB buffer and 3 periods of 3 nm InGaN well and 5 nm InGaN barrier, on n-GaN templates. The total p-GaN was consisted of 150 nm thick nominally doped and 50 nm thick highly doped p-GaN. The designed complete LED structure is shown in Figure 41.
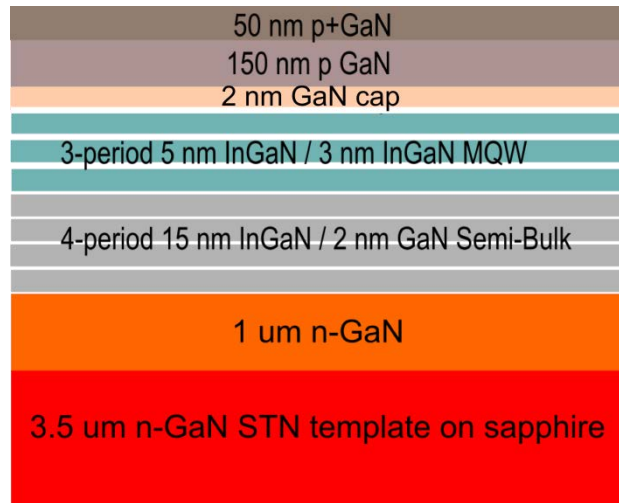
Figure 41: Final design of complete LED structure on "semi-bulk" InGaN buffer.

We used 3.5 μm thick n-type commercial GaN templates (with carrier concentration of 1.7×10^{18} cm^{-3} and dislocation density of 4×10^{8} cm^{-2}) to overgrow the LED layer stacks. The target carrier concentration in n-GaN was 4×10^{18} cm^{-3} and that in p-GaN was 4.8×10^{17} cm^{-3}. Indium content was targeted to be 5% in barriers and SB InGaN and 15% in InGaN wells for blue emission and 25% for green emission. Epitaxial growth parameters for each building block such as the InGaN "semi-bulk" buffer,

InGaN/InGaN MQW and p-GaN were optimized individually, and finally combined to realize the full LED structure.

Growth of n-GaN is straightforward; carrier concentration in the n-GaN linearly varies with silane (SiH_4) doping. For InGaN epitaxial growth, to study the solid-phase incorporation of In at different growth temperatures, several InGaN growth runs were carried out at different temperatures, and by varying In partial pressure (TMIn/III ratio). Variation of solid phase In-content with respect to TMIn/III ratio at different growth temperatures is shown in Figure 42. This plot is beneficial to extract growth conditions to incorporate the desired In-content in the various constituent InGaN layers of the final LED structure.
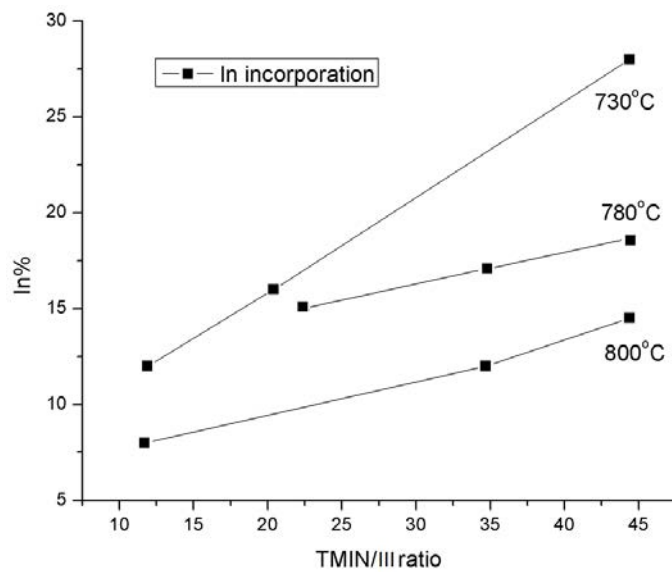
Figure 42: The dependence of solid phase In incorporation on TMIn/III ratio at growth temperatures mainly used in this thesis work.

The In content increases linearly with TMIn/III ratio, however, the slope is higher at 730 °C growth temperature compared to that at 780 °C or 800 °C growth temperature, indicating higher In incorporation efficiency at this lower growth temperature range.

4.2   Epitaxial growth optimization of the "semi-bulk" InGaN buffer

Epitaxial growth of thick high quality InGaN buffer was challenging. InGaN epitaxy has to be performed in a temperature range much lower (650 ^{o}C to 850 ^{o}C) than the conventional GaN growth temperature (~1000 ^{o}C) to avoid desorption of indium, which is not in favour of good crystal quality. Moreover, thickness of the InGaN buffer is crucial. The thickness of the "semi-bulk" buffer layer needed to be redesigned and grown carefully in the case of this thesis work to avoid relaxation of the InGaN SB buffer and also relaxation of the QWs grown on top.

First, two sets of InGaN SB buffer layer were investigated on top of the commercial 3.5 μm thick n-GaN on sapphire templates.

| 2 nm GaN cap |
| 6-period 24 nm InGaN/ 2 nm GaN Semi-Bulk |
| 1 um n-GaN |
| 3.5 um n-GaN STN template on sapphire |

a)

| 2 nm GaN cap |
| 4-period 24 nm InGaN/ 2 nm GaN Semi-Bulk |
| 1 um n-GaN |
| 3.5 um n-GaN STN template on sapphire |

b)
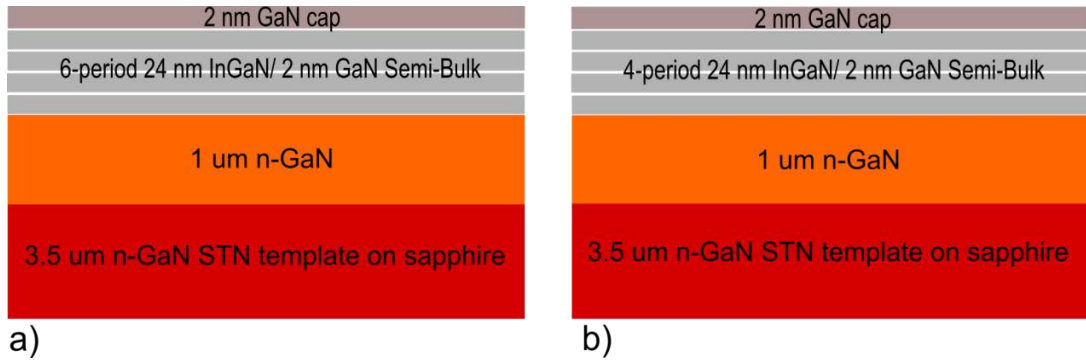
Figure 43: Schematic of the "semi-bulk" sample sets with different thicknesses, sample A (a) and sample B (b).

The growth temperature was 800 ^{o}C for both the samples. Sample A had 6 periods and sample B had 4 periods of 24 nm InGaN layers and 2 nm GaN interlayers in between two successive InGaN layers. Both the structures were terminated with a 2 nm GaN cap. The structures of the sample sets are shown in Figure 43.
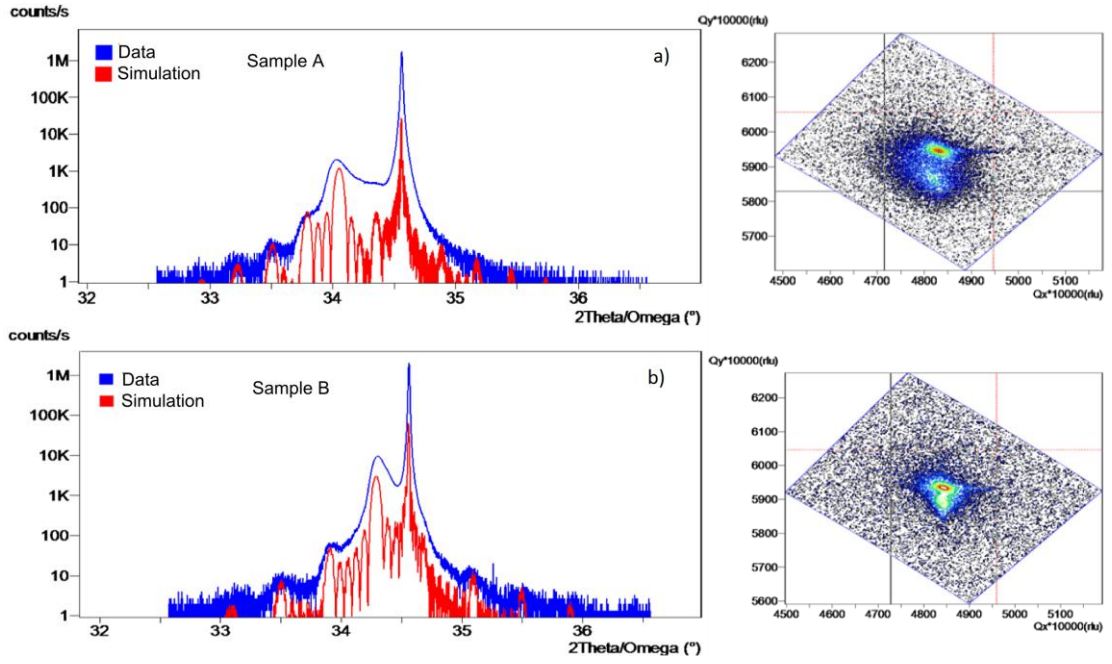
Figure 44: XRD *2θ-ω* scans of sample A (155 nm SB) and sample B (105 nm SB). (RSMs are shown on the right).

Sample A was ~156 nm and sample B was ~105 nm thick. The XRD symmetric (002) *2θ-ω* scan showed average In incorporation of 8±1% and 6±1% obtained from the fitting of data for sample A and sample B (Figure 44, left), respectively. The reciprocal space maps are also shown in Figure 44 (right). It was obtained from the RSMs that sample A was ~30% relaxed whereas sample B had ~8% relaxation. The excess indium in sample A was attributed to more relaxation induced higher In incorporation.

The surface morphology was observed by SEM and AFM. Sample A had much rougher surface with 3D like structures and sample B had better surface morphology with 2D surface, however still with large number of big V-pits and clusters (Figure 45).
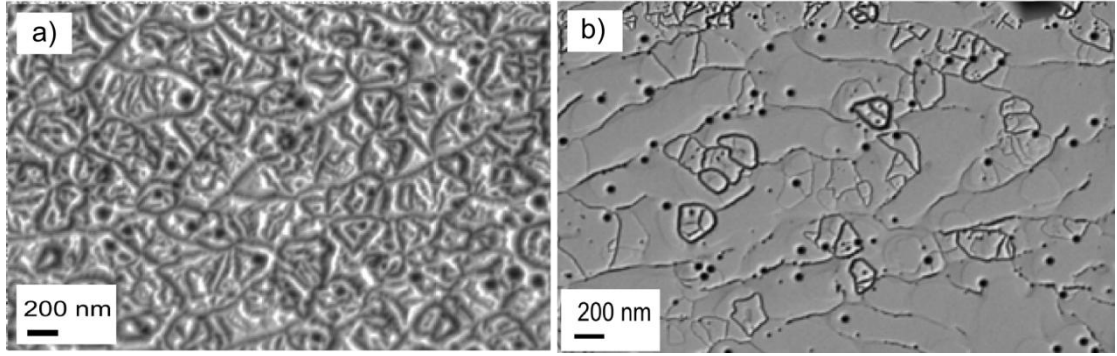
Figure 45: SEM surface morphology of sample A (156 nm SB) (a) and sample B (105 nm SB) (b).

The AFM scan showed RMS roughness of 25.3 nm and 4.74 nm for sample A and sample B, respectively for a $5 \times 5\ \mu m^2$ scan area (Figure 46). Though sample B had
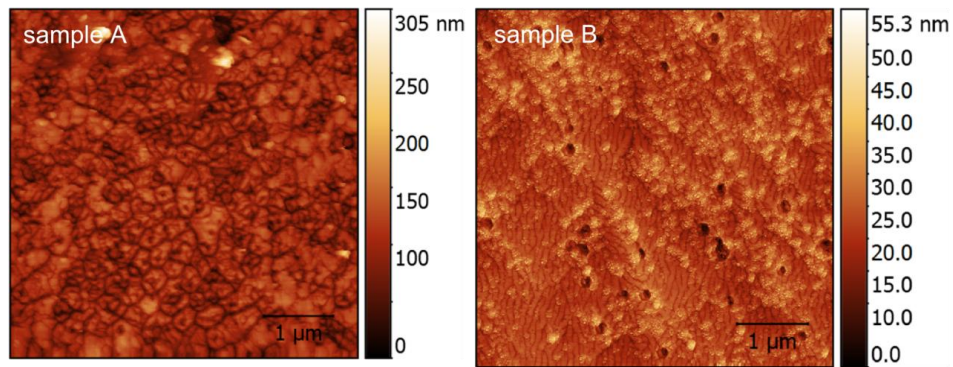
Figure 46: AFM surface morphology of sample A (156 nm SB) (left) and sample B (105 nm SB) (right).

better material quality than sample A, it had dense V-pits and inclusion defects. This implied that the thickness was close to the critical thickness for which relaxation might occur, and making the InGaN SB buffer thicker would significantly degrade the crystal quality by increasing surface roughness and relaxation induced defects that could create leakage current path for LEDs grown on top. Therefore, we decided further reduce the SB buffer thickness to the required ~70 nm to have single phase fully strained InGaN SB buffer.

The optimized "semi-bulk" InGaN buffer

An optimized ~70 nm thick SB InGaN structure, with a target indium content of 6±1%, was grown at 800 °C, to be used as buffer. The XRD 2θ-ω scan of the optimized SB buffer is shown in Figure 47. The fitting of data by simulation confirms 6±1% of average In incorporation in the InGaN SB. The RSM shows (Figure 47, inset) only ~8% relaxation.
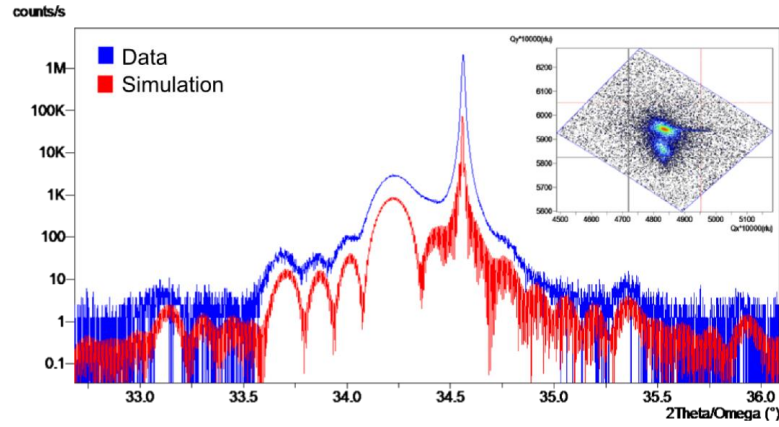
Figure 47: XRD 2θ-ω scan of the optimized SB buffer sample with 6±1% In and ~70 nm thickness.
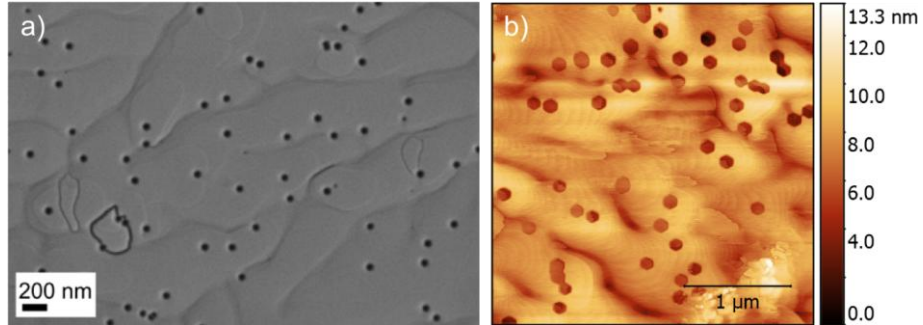
Figure 48 : SEM morphology (a) and AFM 3 × 3 μm² scan (b) of the optimized SB buffer sample with 6±1% In and ~70 nm thickness.

The SEM (Figure 48a) and AFM (Figure 48b) surface morphology of the optimized SB buffer are shown in Figure 48. The V-pit density of the SB sample was 7.5×10^{8} cm^{-2} with significantly lower inclusion defects and clusters compared to those of the 105 nm thick SB sample as shown in Figure 45b. The RMS roughness of a 3 × 3 μm²

AFM scan was ~3.0 nm. LTCL experiment was carried out and the result confirmed single phase indium in the InGaN SB buffer without any phase separation related multiple peaks visible in the LTCL spectrum.
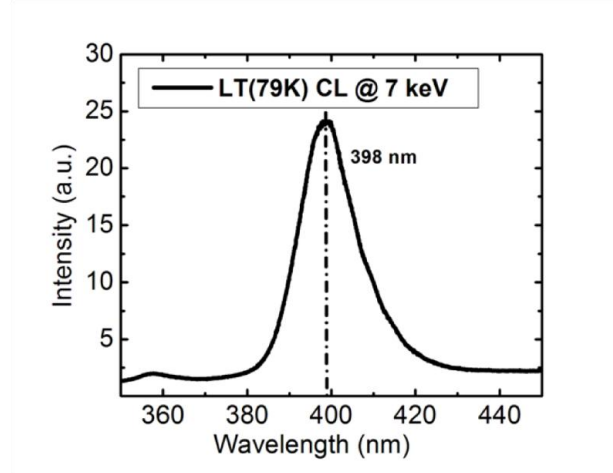
Figure 49 : LTCL of the optimized SB buffer sample with 6±1% In and ~70 nm thickness.

The emission spectrum is shown in Figure 49. Electron beam energy of 7 keV was chosen, which was sufficient to reach and excite the carriers in SB InGaN [39]. A single emission peak at ~398 nm, that corresponds to ~6% In in strained InGaN, estimated from calibration samples in our previous work [104], confirmed single phase indium in the SB InGaN. FWHM of ~13 nm confirmed good crystal quality.

4.3 Optimization of InGaN/(In)GaN multiple quantum well (MQW)

4.3.1 Effect of growth temperature, thickness and TMIn/III ratio on the characteristics of MQW emitting in blue and cyan spectra

We compared four sets of InGaN/InGaN MQW samples to study the effect of well growth temperature, well thickness and TMIn/III ratio for the growth of wells on the surface morphology and emission characteristics of the MQW. The MQW structure studied is shown in Figure 50.
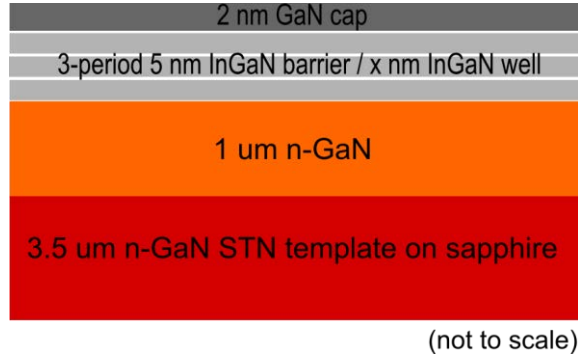
Figure 50: InGaN/InGaN MQW structure for the study of varying growth temperatures, well-thicknesses and TMIn/III ratios for the growth of wells.

The target In incorporation was ~5% in the 5 nm thick barriers and 15% to 18% in the wells for blue and cyan emission. The well-thickness (x) was varied from 2 to 3 nm and the TMIn flow rate was adjusted during the growth of wells. The average well In content was extracted from XRD 2θ -ω scan, surface morphology was studied by SEM and AFM, and the emission spectra were observed by low temperature CL. The sets of samples are summarized in Table 6.

Table 6: Sample sets for the study of growth temperature, thickness and TMIn flow rate of wells of MQW

Sample set	Well Growth temperature	Well thickness	TMIn flow rate for well growth	In%
Sample A	800 ^{o}C	2 nm	6.60 μmolmin^{-1}	10%
Sample B	780 ^{o}C	2 nm	6.60 μmolmin^{-1}	15%
Sample C	780 ^{o}C	3 nm	6.60 μmolmin^{-1}	15%
Sample D	780 ^{o}C	3 nm	12.12 μmolmin^{-1}	18%
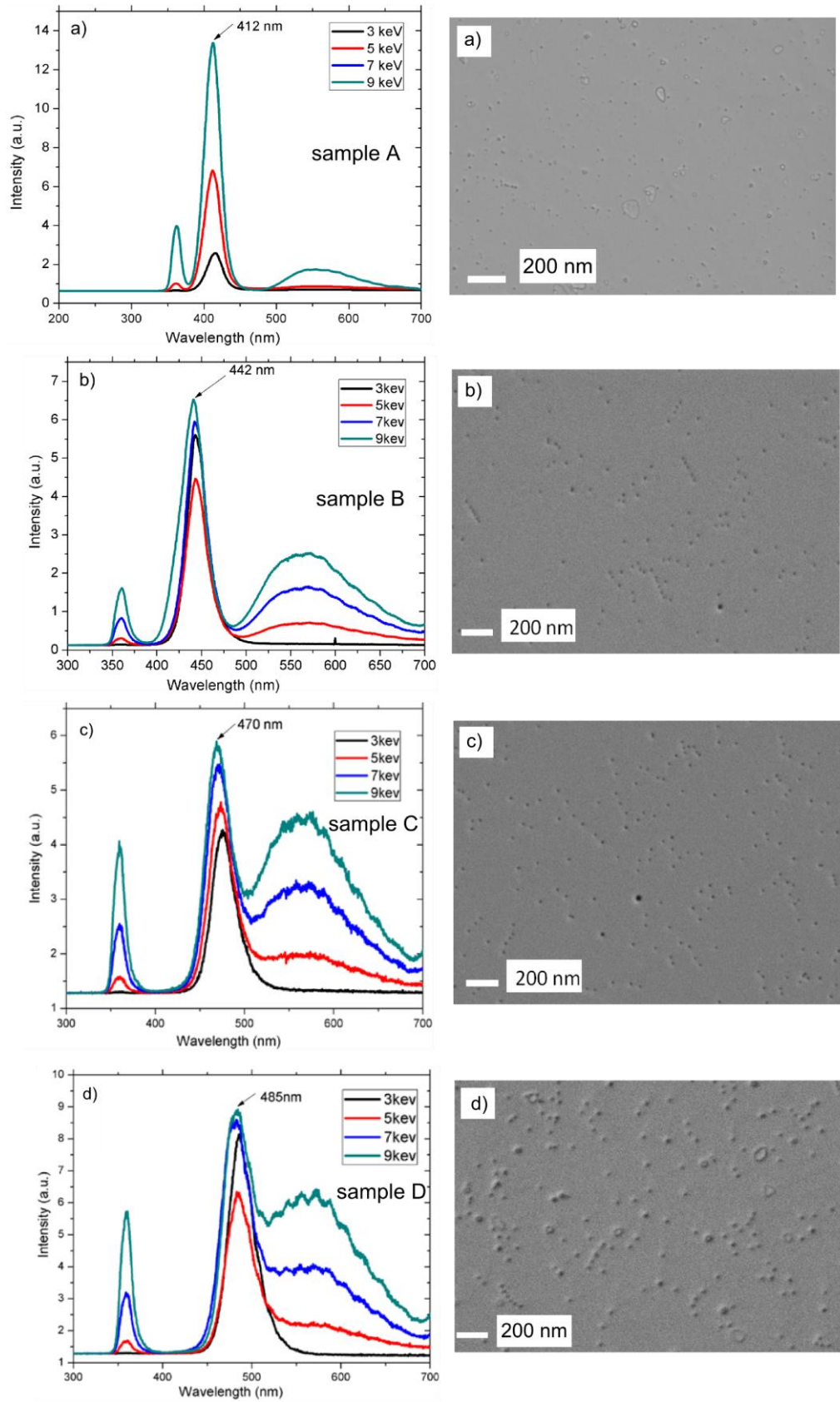
Figure 51: LTCL (left) and SEM images (right) of sample sets for the study of growth temperature, thickness and TMIn flow rate for the growth of wells of MQW.

Reducing the growth temperature from 800 $^{\circ}$C for sample A to 780 $^{\circ}$C for sample B resulted 5% more In incorporation (from 10% to 15%), as lower growth temperature incorporates more In by minimizing In desorption and mobility of In atoms [105]. However, the lower growth temperature resulted in more density of V-pits in sample B (5.7 $\times$ 10^9 cm^{-2}) compared to that of sample A (4.8 $\times$ 10^8 cm^{-2}) (Figure 51b, right). Increasing the well thickness from 2 nm (sample B) to 3 nm (sample C) increased the emission wavelength from ~442 nm to ~470 nm (Figure 51c, left), presumably due to the reduction of effective bandgap energy and increase of QCSE. The pit density of sample C was (7.1 $\times$ 10^9 cm^{-2}). Further, keeping the growth temperature and thickness of sample D the same as those of sample C but doubling the TMIn flow rate from 6.60 μmolmin^{-1} to 12.12 μmolmin^{-1}, for a fixed TMGa flow rate of 5.06 μmolmin^{-1}, increased the In content from 15% to 18%, therefore, the emission wavelength increased from 470 nm to 485 nm (Figure 51d). However, the SEM surface morphology showed bigger pits (Figure 51d, right) resulted from more-In related increase in localized strain, though there was not a dramatic change in pit density (~8 $\times$ 10^9 cm^{-2}) compared to that of sample C [105].

4.3.2   *Growth of InGaN as barrier layers of InGaN MQW emitting in blue-cyan spectra*

Since simulation results showed improved emission intensity and better efficiency for InGaN barrier instead of GaN barrier (chapter 3), MQWs with both GaN barrier and InGaN barrier were epitaxially grown and compared experimentally. Three-period 3 nm In$_x$Ga$_{1-x}$N wells and 5 nm GaN or In$_y$Ga$_{1-y}$N barriers ($x > y$) were grown. Here x varied from 0.15 to 0.28 and y from 0.05 to 0.12 to have blue to green spectra emission. The growth temperature was 1000 $^{\circ}$C for GaN and 780 - 800 $^{\circ}$C for InGaN. The TMIn flow was controlled to get the desired In incorporation, the

TMIn/III ratio was 10 for barrier growth and 45 for well growth. The growth pressure was 100 torr.
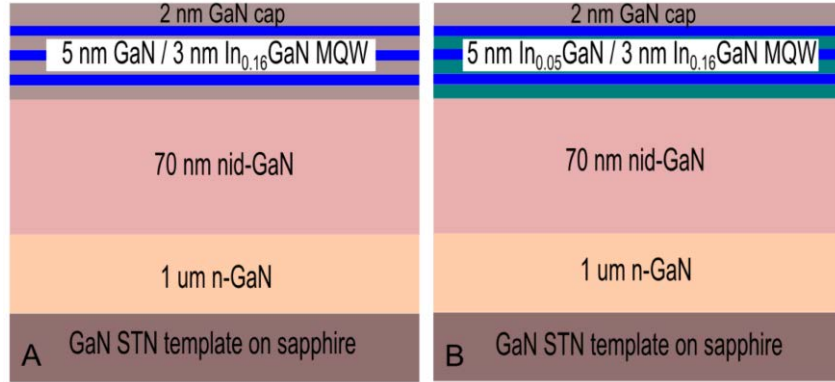
Figure 52 : Structure schematic of MQW sample A with GaN barrier and sample B with In$_{0.05}$Ga$_{0.95}$N barrier.

The schematic of MQW structures with GaN barrier (let, sample A) and In$_{0.05}$Ga$_{0.95}$N barrier (let, sample B) are shown in Figure 52. Surface morphology study of sample A and sample B were carried out by SEM. It was observed that sample with InGaN barrier had increased V-pit density and inclusion defect density (Figure 53).
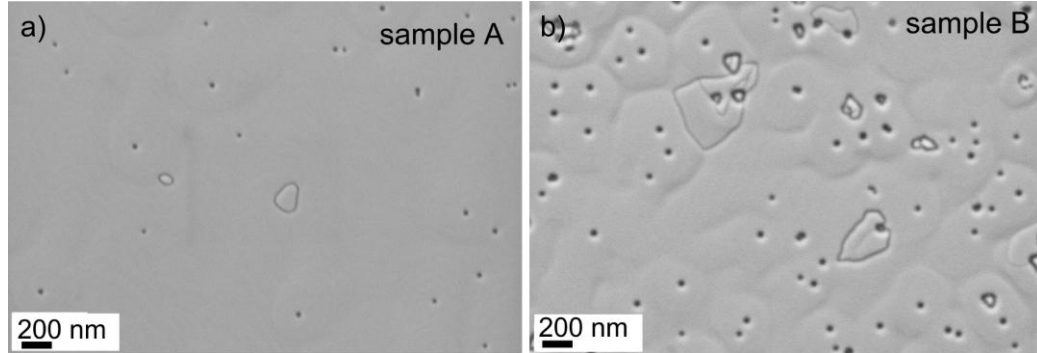
Figure 53 : SEM surface morphology of MQW sample A with GaN barrier (a) and sample B with In$_{0.05}$Ga$_{0.95}$N barrier (b).

However, the RMS roughness of the surface was still good and was 2 nm for a 20 μm × 20 μm scan area in AFM. Excess In content would create In desorption and aggregation related defects and thus more non-radiative recombination centers, and

therefore it was necessary to get the optimal In content to get the maximum IQE for our MQW.

Extracted from the fitting of the XRD 2θ-ω scan data (shown in Figure 54), the average In incorporation in the wells was ~18% for sample A, and ~16% for sample B. The average In incorporation in the barrier of sample B was ~5%. Both the structures were fully strained on the n-GaN templates underneath, as confirmed from the XRD RSMs around the asymmetric (114) plane (Figure 54, right).
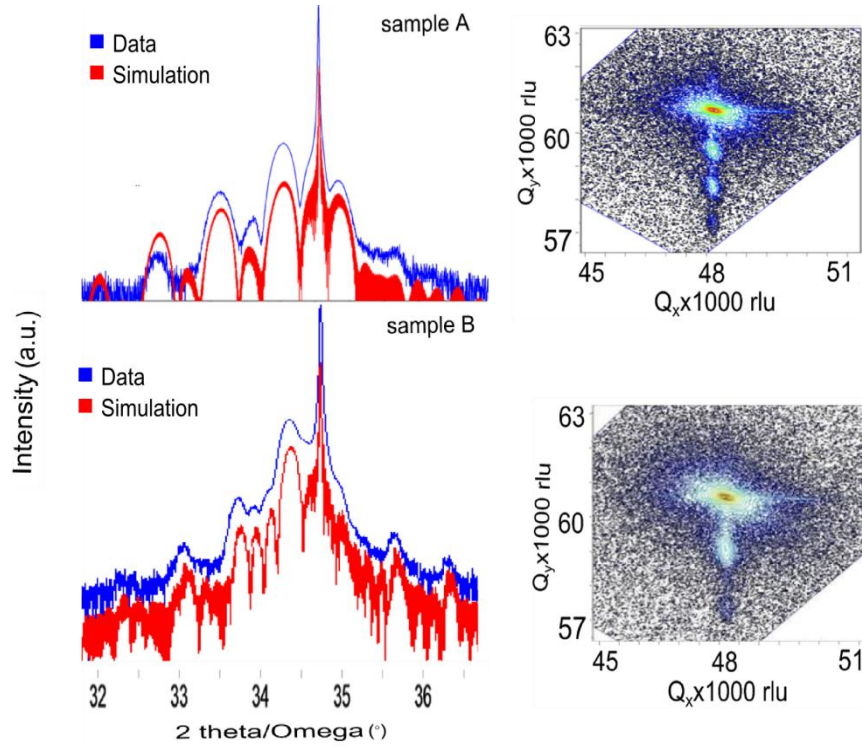
Figure 54: XRD 2θ-ω scans of sample A (MQW with GaN barrier) and sample B (MQW with In$_{0.05}$Ga$_{0.95}$N barrier) (insets show the RSMs).

The lower In content in the well of sample B is presumably the result of In out-diffusion from the well because of the lower abruptness in well/barrier interface in the case of InGaN barrier compared to that in the case of GaN barrier [106]. CL emission spectra for sample A and sample B at electron beam energy of 3 keV are shown in Figure 55. The emission from the MQW with GaN barrier is at 480 nm. The relative

emission intensity got doubled with improved FWHM for InGaN barrier compared to those for GaN barrier and the emission wavelength was blue-shifted by ~30 nm. We attribute this blue-shift to the increased effective bandgap, reduced polarization and reduced QCSE in the active region, and 2±1% lower In incorporation in the well. Because the CL measurement was carried out in room temperature (290 K), the emission peak around 550 nm represents the defect-related yellow band emission from the template which was not suppressed at this measurement temperature.
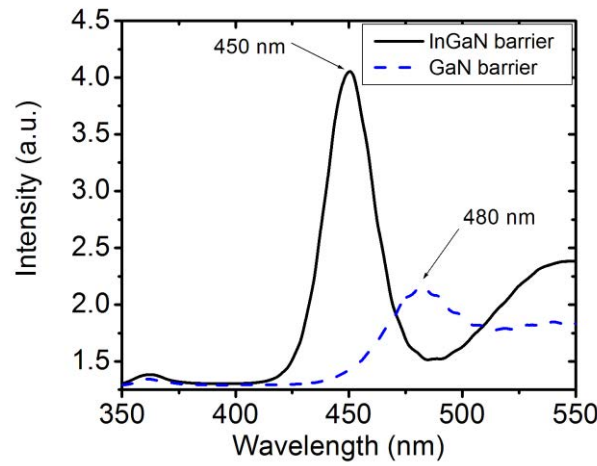
Figure 55 : Room temperature CL spectra of MQW sample A with GaN barrier and sample B with In$_{0.05}$Ga$_{0.95}$N barrier.

Sets of samples with the same structure but with higher In-content in the well with a target emission in longer wavelength "green-gap" spectra, were epitaxially grown and studied by low temperature (15 K) PL. The growth temperature of the well was 730 $^{\circ}$C and TMIn/III ratio was 45. The average well In-content was 25±1% for both the samples and the average barrier In was 5±1% for the sample with InGaN barrier, extracted from the fitting of XRD 2θ-ω scan data.

The LTPL result is shown in Figure 56. The same trend as lower In content samples was observed where a blue-shift of ~35 nm was experimentally obtained with more than three-fold increase in emission intensity and improved FWHM.
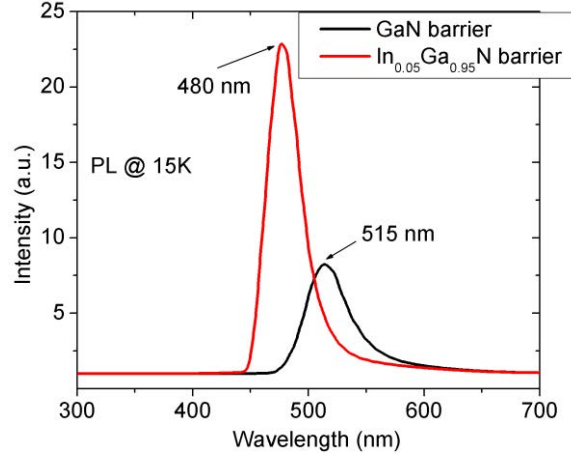
Figure 56 : Low temperature photoluminescence of 25% In-content MQW sample with GaN barrier and with In$_{0.05}$Ga$_{0.95}$N barrier.

4.3.3   Epitaxial growth of InGaN/InGaN MQW on "semi-bulk" InGaN buffer

We epitaxially grew InGaN/InGaN MQW on SB In$_{0.05}$Ga$_{0.95}$N buffer (sample C), and compared this MQW structure with reference InGaN/InGaN MQW structure grown on GaN buffer (sample B).
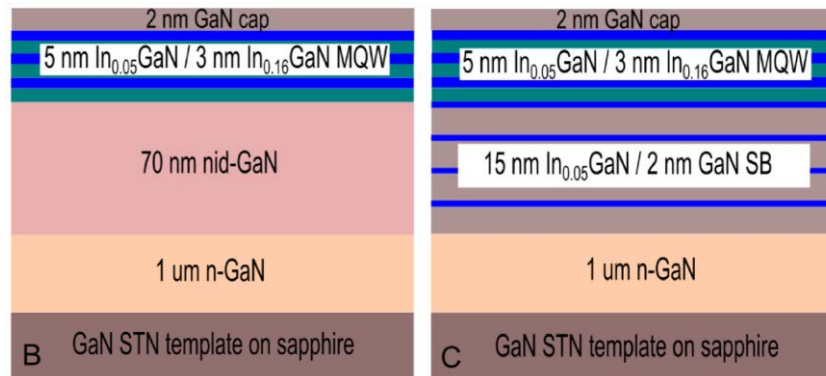
Figure 57: Structure schematic of MQW sample with In$_{0.05}$Ga$_{0.95}$N barrier on GaN buffer, sample B (left) and on SB In$_{0.05}$Ga$_{0.95}$N buffer, sample C (right).

The MQW structures are schematically shown in Figure 57. Sample B had 1 μm n-GaN on GaN template, followed by 70 nm nid-GaN buffer and then 3 periods of 5 nm $In_{0.05}Ga_{0.95}N$ barrier and 3 nm $In_{0.15}Ga_{0.85}N$ well and finally capped by 2 nm GaN. Sample C had similar structure, except that the 70 nm nid-GaN buffer was replaced by SB $In_{0.05}Ga_{0.95}N$ buffer. InGaN MQWs with average well In content of 16±1% were grown on top of the buffers in case of both sample B and sample C.
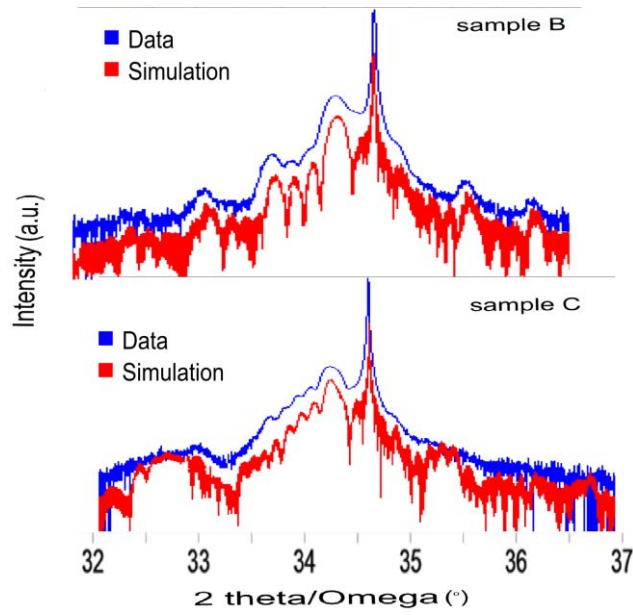
Figure 58: XRD 2θ-ω scans of sample B (MQW with $In_{0.05}Ga_{0.95}N$ barrier on GaN buffer) and sample C (MQW with $In_{0.05}Ga_{0.95}N$ barrier on SB $In_{0.05}Ga_{0.95}N$ buffer) .

Figure 58 shows XRD symmetric (002) 2θ-ω scan data for sample B and sample C which fits well with the simulation with average well indium of 16±1% in both the samples. Sample C had ~20% relaxation, whereas sample A and B were fully strained on n-GaN templates, derived from XRD RSMs around the asymmetric (114) plane. Details of the RSM images of sample B and sample C are shown and the effect of this partial relaxation is discussed in the upcoming paragraphs. The SEM surface morphology of sample B and sample C are shown in Figure 59.
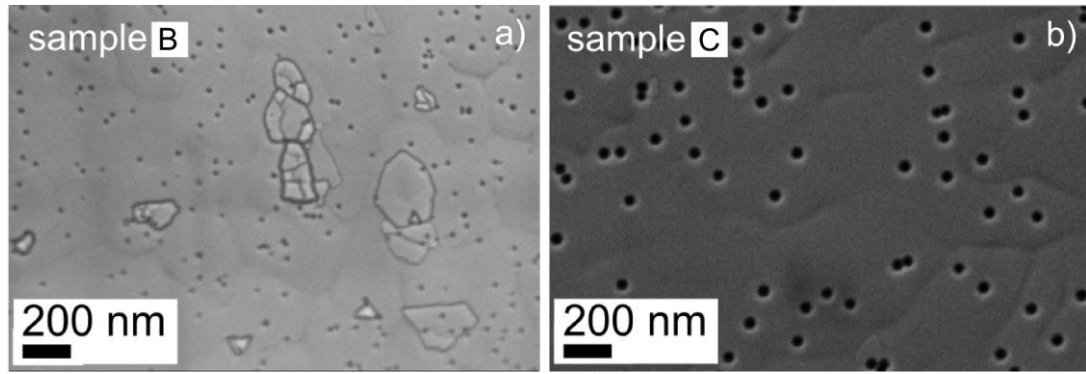
Figure 59: SEM images of MQW sample with In$_{0.05}$Ga$_{0.95}$N barrier on GaN buffer (a) and on In$_{0.05}$Ga$_{0.95}$N SB buffer (b).

The V-pit density of sample B and sample C were 7.1×10^8 cm^{-2} and was 8×10^7 cm^{-2} respectively, counted from the SEM images. The RMS roughness of sample B and sample C were 1.8 nm and 3 nm respectively for AFM 5×5 μm^2 scan area. Though using InGaN SB buffer in sample C increased the width and depth of the V-pits, the lower pit density and the absence of inclusion defects were the results of strain relief and hence partial reduction of strain energy [107]. Lower V-pit density and inclusion defects made the surface morphology quality of sample C quite acceptable.

4.3.4   Photoluminescence study of the MQW samples

The three sets of MQW samples discussed in the preceding paragraphs were characterized by temperature and excitation power dependent PL. The structures of the sample sets are summarized in Table 7.

Table 7: MQW samples studied and compared in photoluminescence study

Sample name	Buffer	Barrier	In% in well	In% in barrier/SB
Sample A	GaN	GaN	16±1%	-

| Sample B | GaN | InGaN | 16±1% | 6±1% |
| Sample C | SB InGaN | InGaN | 16±1% | 6±1% |
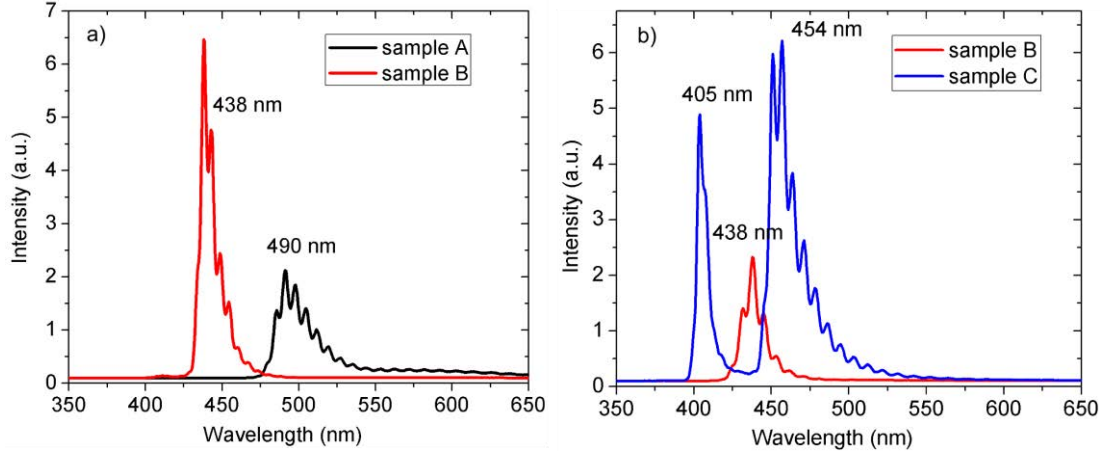
Figure 60: Low temperature (15 K) PL spectra comparison of sample A and B (a) and sample B and C (b).

In low temperature (15 K) PL experiment, sample A showed an emission peak at 490 nm and B showed an emission at ~438 nm (Figure 60a). More than three-fold improvement in emission intensity for sample B compared to that of sample A is attributed to the reduction in potential barrier height and more homogeneous repartition of carriers in the wells owing to the presence of indium in the barrier. Moreover, part of it might be due to the fact that higher PL intensity is always observed at shorter wavelength. LTPL for the MQW of sample C (Figure 60b) yielded an emission at ~454 nm with a FWHM of ~20 nm. The InGaN "semi-bulk" emission peak was also visible at ~405 nm. Even though the internal electric field was predicted to be lower in MQW of sample C compared to that in MQW of sample B, as

already had been shown in the simulation result in CHAPTER 3, the ~15 nm red-shift in emission wavelength for sample C is attributed partially to the increase of well thickness and In-content variation induced by partial strain relaxation and In pulling also. The relative PL emission intensity, when using the SB InGaN as buffer, got doubled compared to sample B in spite of the fact that the PL emission was slightly red shifted compared to sample B, and showed six-fold increase compared to sample A (Figure 60). This improvement can definitely be attributed to the insertion of the SB buffer layer as both sample B and sample C had the same MQW structure except that sample C had InGaN SB buffer beneath the MQWs. From the measured integrated PL intensity at different laser excitation power levels and from 15 K to 290 K temperature range, and using power normalized integrated intensity, the room temperature IQE was calculated to be 67.5% by taking the ratio of the PL integrated intensity at 290 K and 15 K. Based on the assumption that at this low temperature of 15 K, the thermal agitation was not enough to give carriers the energy to be trapped in the defects and to result non-radiative recombination, the radiative recombination efficiency was considered to be 100% at 15 K [108,109].

From the integrated PL intensity versus $1/T$ plots for sample A, B and C, it was observed that the thermal quenching of non-radiative recombination process was worse for sample A and B compared to that of sample C and the shapes of these curves suggested that the intensity decrease was more prominent at high temperature range for sample A and B than that of sample C. The shapes of these curves showed the earliest saturation of integrated PL intensity with decreasing temperature for sample C revealing the reduced effect of non-radiative recombination channel for sample C [110].

The oscillations or fringes in the PL spectra are due to the Fabry-Perot optical interferences within the layers in the structures [111,112].

4.3.5   *Emission wavelength red-shift by using "semi-bulk" InGaN buffer*

Emission wavelength red-shift was experimentally obtained both in CL and PL, for the same InGaN/InGaN MQW grown on "semi-bulk" InGaN buffer (sample C) compared to the reference InGaN/InGaN MQW grown on GaN buffer (sample B). The two structures have already been shown for comparison in Figure 57. This red-shift is in contradiction with the expected blue-shift effect related to the reduction of built-in electric field, and hence reduced band bending, as predicted by simulating the structures. We can suppose that reduced electric field is actually obtained in sample B, since our experimental result showed higher emission intensity, which is very probably due to the reduced QCSE, in coherence with the previously reported results [113]. The red-shift could possibly be related to the decrease of the heights of the barriers on the sides of the wells, leading to reduced localization or quantum confinement effect affecting the positions of the discrete levels within the MQW structure.

The layers stack with optimal number and thickness of quantum wells was not sufficiently thick to relax when grown on GaN buffer (sample B). However, when grown on the SB $In_{0.05}Ga_{0.95}N$ buffer, the structure started to relax partially. We did XRD asymmetric (114) reciprocal space mapping to get the relaxation status of the two samples. The RSMs are shown in Figure 61. Sample C had ~20% relaxation (Figure 61, right) whereas sample B was fully strained on GaN template (Figure 61, left).
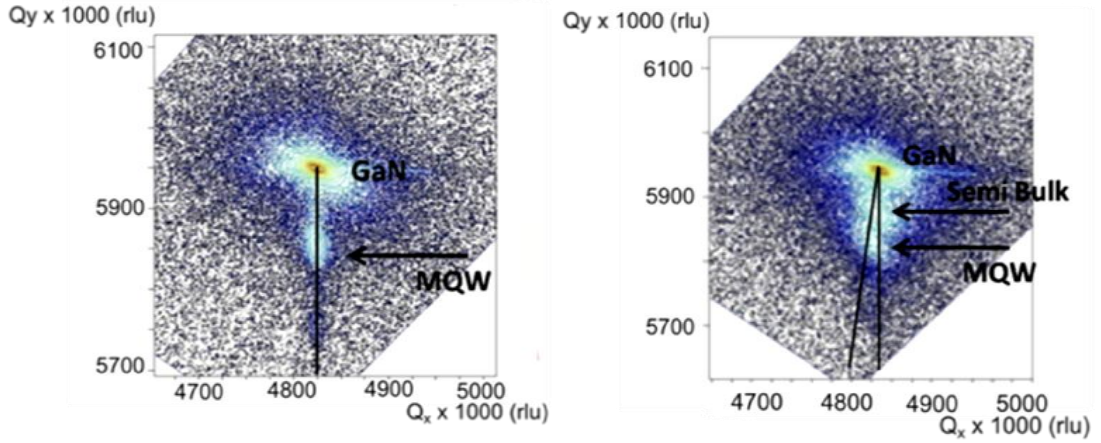
Figure 61 : Reciprocal space mappings (RSMs) of sample B (left) and of sample C (right).

It has already been shown (Figure 58), that the average In incorporation in the wells of both the samples B and C was ~15%, extracted from the XRD 2θ-ω scan. There was no higher In incorporation on average in the wells of sample C beyond the error bar of ±1%. The average In content in the barriers was ~5% in both sample B and C, also extracted from XRD 2θ-ω scan.
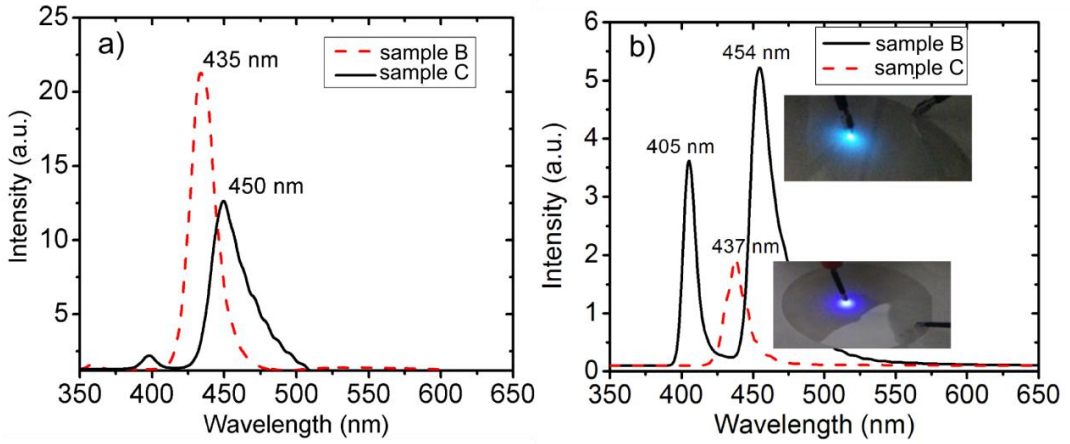
Figure 62 : Low temperature cathodoluminescence spectra (a) and low temperature photoluminescence spectra (b) of the reference InGaN/InGaN MQW structure on GaN buffer (sample B) and our designed InGaN/InGaN MQW structure on "semi-bulk" InGaN buffer (sample C).

For both the samples B and C, low temperature (77 K) cathodoluminescence (LTCL) and low temperature (15 K) photoluminescence (LTPL) experiments were carried out. The results are shown in Figure 62. Emission wavelength is red shifted by ~15 nm for sample C (Figure 62a) in LTCL experiment. However, FWHM deteriorates due to degradation of crystal quality when MQWs are grown on InGaN SB buffer (the RMS roughness is 3 nm for MQW grown on SB buffer compared to 2 nm of that for reference MQW in AFM 5×5 μm^2 scan). From the LTPL as well, we observed similar red shift of ~17 nm in the emission wavelength (Figure 62b). The emission from "semi-bulk" InGaN is visible at 398 nm in CL and at 405 nm in PL. The difference in emission wavelength is due to the difference in excitation mechanism [114] and the difference in experiment temperature that was 77 K for CL and 15 K for PL. The difference in relative emission intensity between the two samples in CL and PL was due to the difference in excitation area which was 5×5 μm^2 for CL and 2.5×10^5 μm^2 for PL, therefore PL integrated intensity was higher.

Depth resolved CL showed only 3 nm wavelength shift for sample B (Figure 63a) and ~4 nm peak wavelength variation for sample C (Figure 63b) from top to bottom of the QWs. This suggests very low compositional variation in the MQW for sample C along the growth direction. The QCSE can be estimated from the dependence of emission wavelength on the PL excitation power. It can be seen from Figure 63c that the rate of blue-shift of emission wavelength with increasing excitation power is not significantly different for sample B and sample C. This confirms that the QCSE in sample C is equal to or lower than that in sample B.
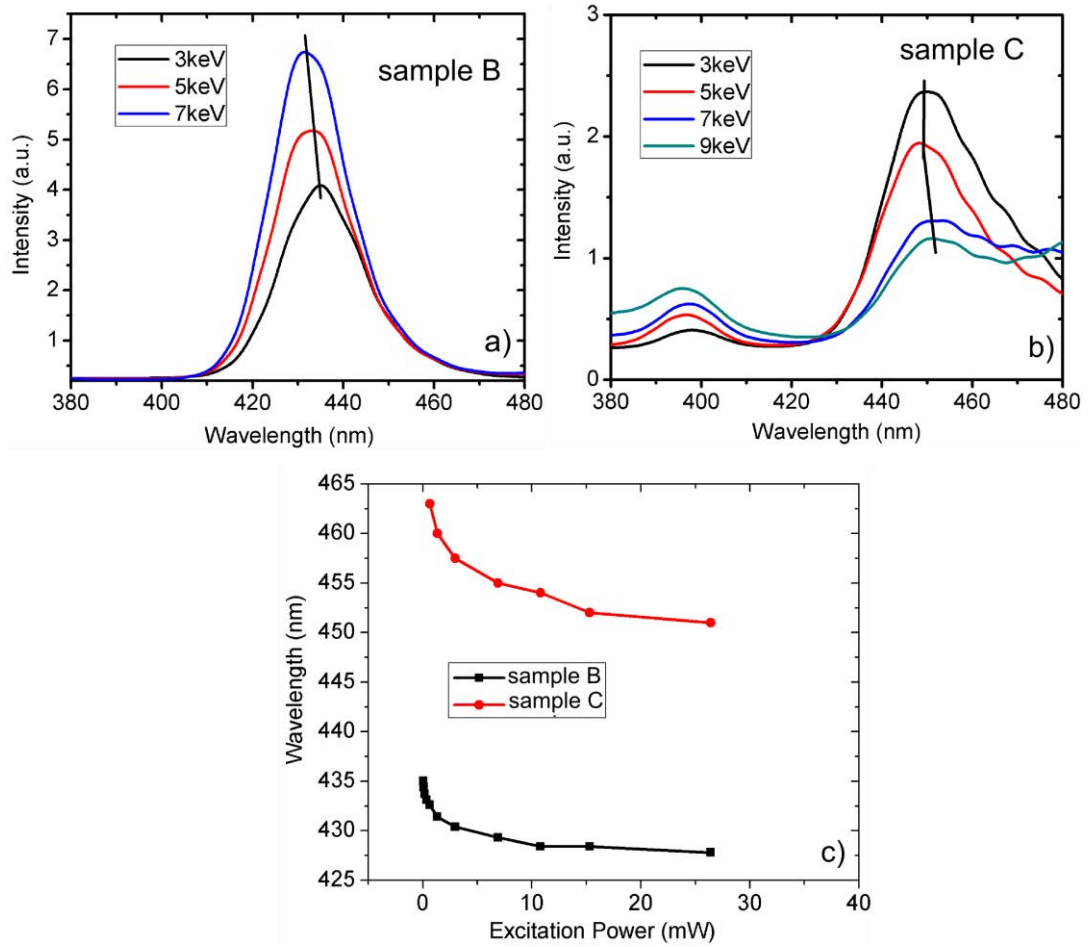
Figure 63 : Depth resolved cathodoluminescence spectra for sample B (a), sample C (b) and dependence of emission wavelength on photoluminescence excitation power for sample B and sample C (c).

However, in the PL experiment, a clear indication of increase in emission intensity has been observed for sample C which is attributed to the reduced electric field and hence reduced band bending, providing more overlap of electron-hole wave function in sample C [113]. Temperature and excitation power dependent PL experiments were carried out for the MQW on "semi-bulk" sample C. The PL integrated intensity was measured at 15 K for different excitation power levels and at 10 mW excitation power for different temperatures. The variations of peak wavelength are shown in Figure 64.
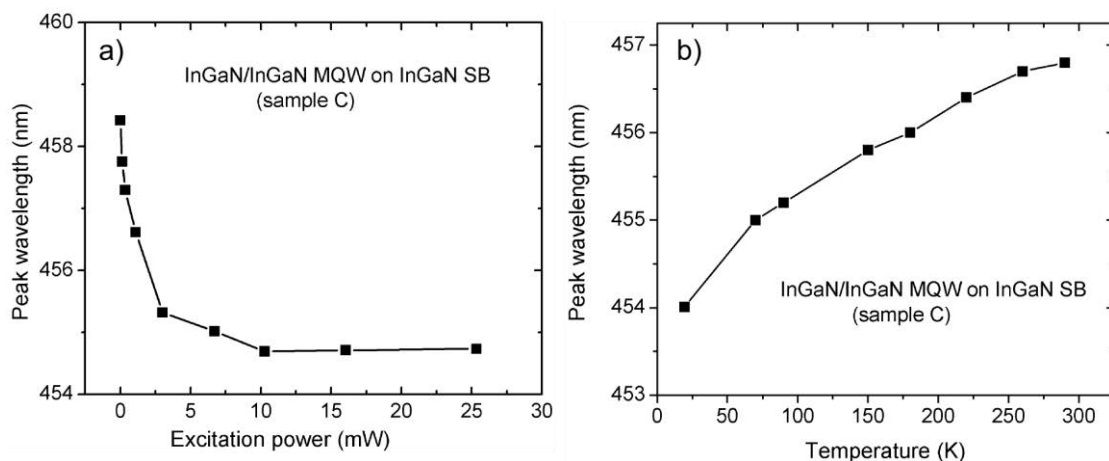
Figure 64: Excitation power versus peak wavelength (a) and temperature versus peak wavelength (b) in PL experiments for our final MQW on SB sample C.

It has been observed that the excitation power dependent blue-shift and temperature dependent red-shift is not very prominent (only ~3 nm) for sample C. This implies that the carrier induced screening of QCSE is not much with increasing excitation power at a fixed low temperature of 15 K (Figure 64a). The blue-shift due to localized states filling by carriers is limited at this excitation power level.

The HAADF-STEM images confirm the that the layers of the MQW stack have thickness in conformity with the design and exhibit clear interfaces between the layers, for both of the samples, sample B and sample C (Figure 65). EDX also confirms homogeneous distribution of indium in the wells and barriers and line scan confirms average In incorporation of 15±1% in the wells and of 5±1% in the barriers (Figure 66). No significant increase in average In incorporation was visible for sample C in EDX scan, which is consistent with the XRD result shown before. In the MQW, it can be seen from the contrast of STEM images that no significant In-rich clusters are visible (Figure 67).
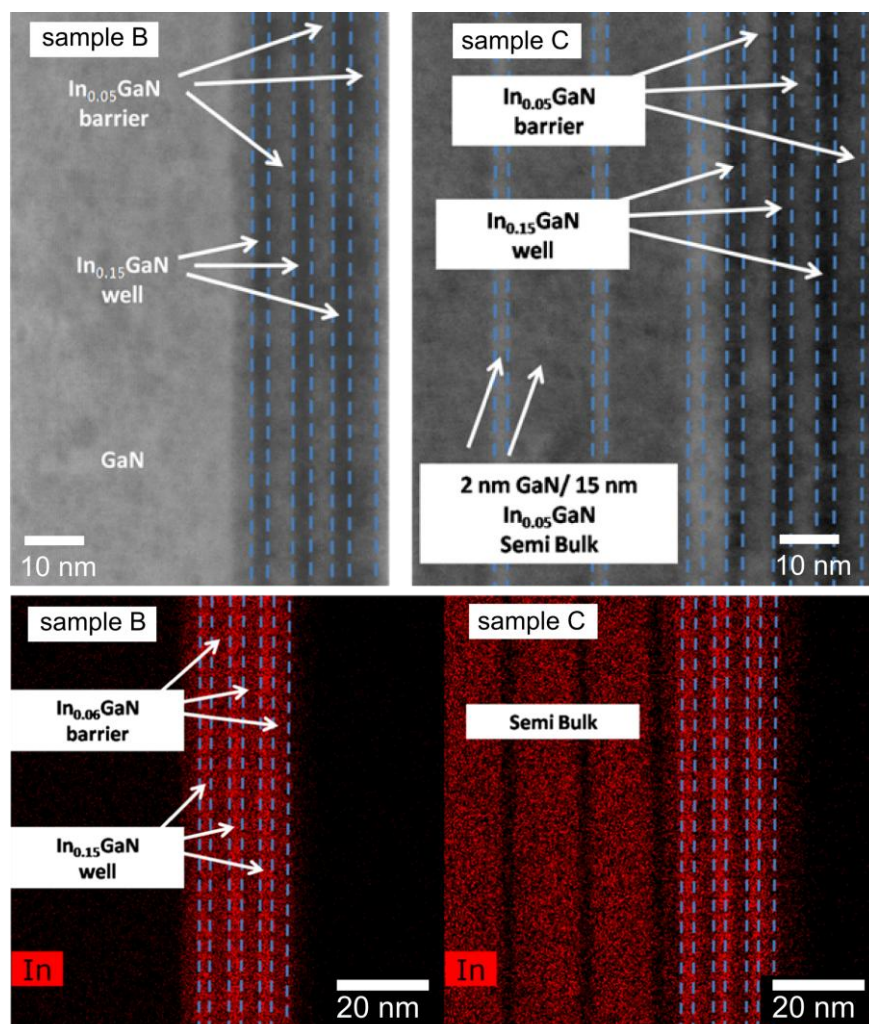
Figure 65 : HAADF-STEM images (top), EDX images (bottom) of sample B and sample C.
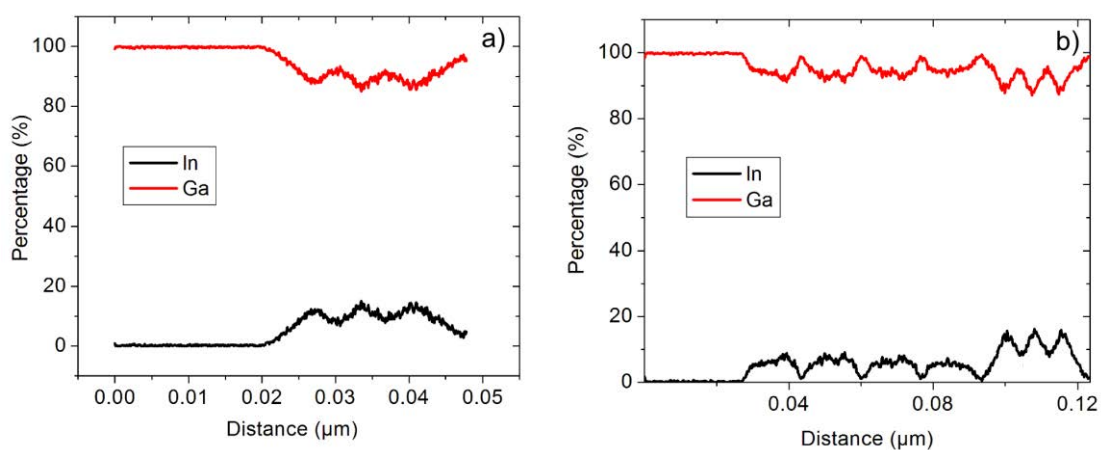
Figure 66 : EDX line scan along growth direction of sample B (a) and sample C (b).
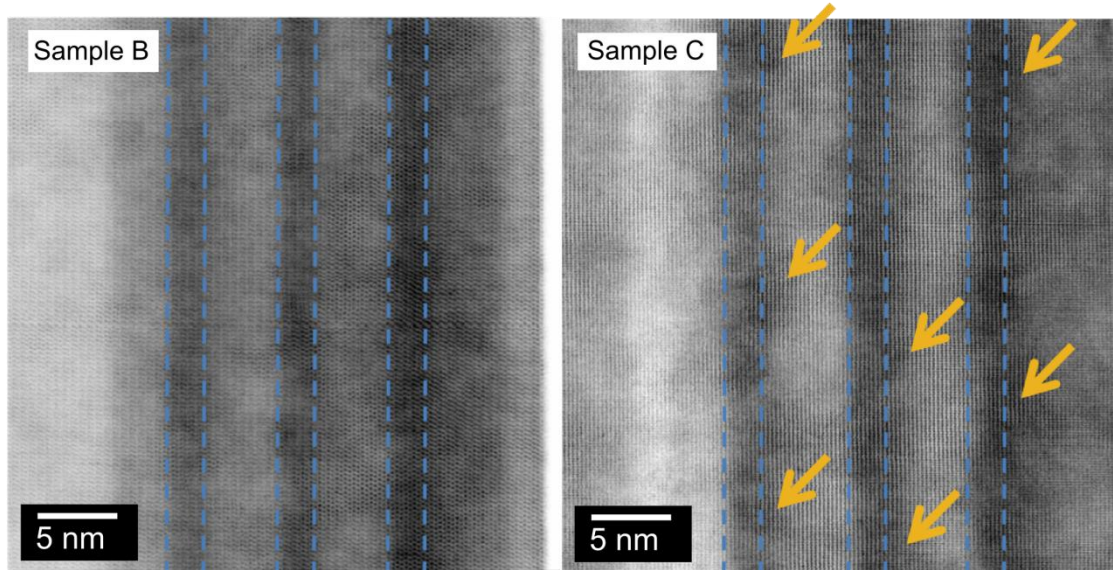
Figure 67 : Investigation of In-rich clusters in reference MQW sample on GaN buffer, sample B (left) and MQW on "semi-bulk" buffer, sample C (right). The arrows show some locations where effective well thickness varies.

It seems that out-diffusion of indium from the well caused slight thickness increase in some locations of wells (yellow arrows in Figure 67), particularly in the last QW, that can be expected to change the confinement energy and partly contribute to the red-shift for our MQW sample with SB buffer.

This out-diffusion of In was probably due to the presence of SB InGaN buffer layer that caused some extent of In variation, induced by compositional pulling, in the wells, particularly in the last one. The effect of thickness variation on emission wavelength was simulated and ±7 nm shift of wavelength has been calculated for MQW structure on SB (sample C) for a well thickness variation from 2.5 to 3.5 nm (Figure 68) around 3 nm design thickness. Similar MQW thickness variation had been reported for a MQW with superlattice prelayer in G. H. Gu *et al.* [115]. Therefore, we estimate that the thickness of our QW might have increased by 0.5 to 1 nm in sample C compared to that of sample B.
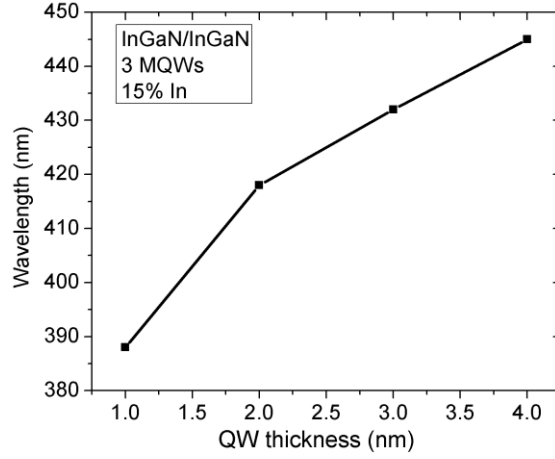
Figure 68: The variation of emission wavelength with the variation of QW thickness simulated for a structure similar to sample C.

Our MQW on SB has presumably higher interface roughness in the last QW, coming from accumulated strain in the growth direction [115], is due to the more numerous InGaN/GaN interfaces in the MQW on SB sample (sample C). From previous studies [116,117], this interface roughness is expected to decrease the non-radiative recombination, due to the tendency of scattering in the interface roughness, which makes the probability of carriers getting trapped in non-radiative recombination centers lower. This was in agreement with our higher PL emission intensity for sample C. Moreover, the simulations, described in previous section 3.2.2, carried out at current density of 200 A/cm^2, have allowed us to compare the polarization charge and electric field for both the structures. It was found that, at this high bias, the electric field in the MQW on "semi-bulk" buffer was lower than that of reference structure and QCSE induced band bending was also reduced. This explains the higher radiative recombination in the case of sample C resulting from the more efficient overlap of electron and hole wave functions [113], as discussed before. Therefore, even though well thickness increase might have separated electron and hole wave functions, however, in our case, the effect of reduced electric field associated with an increase in wave function overlap dominates and brings experimental increase in

118

emission intensity. We assume that, at this high electrical excitation, the band filling caused almost complete screening of QCSE [118].

Three major factors interplay and are governing the emission wavelength: the In composition in the active region, the net polarization (spontaneous and piezoelectric) induced electric field (that creates QCSE), and the screening and band filling effect caused by injected carriers at high current density. In summary, we conclude that the red-shift in the emission wavelength, experimentally observed for sample C, is the result of the combined contributions of 3 effects: the well thickness increase, indium richer regions due to possible compositional pulling in the last quantum well, and higher In incorporation related to some relaxation. The total red shift can be divided as follows,

Total shift (17 nm) ~ well thickness increase (7-8 nm) + 20% relaxation (2-3 nm) + In rich (±4%) regions (5-6 nm).

The first estimate comes from the simulation of emission wavelength dependence on well-width for our particular structure. The second part is in accordance with our previous work [104], and the third part is estimated from our calibration samples grown in the same reactor under similar conditions. Even though the XRD result yielded nearly same In incorporation for MQW with and without InGaN SB buffer, this estimation of In-content was actually the average In% in the wells of the MQW and the localized variation of In-content could still be present in the MQW.

4.4   Epitaxial growth optimization of p-GaN

One of the challenging steps in the growth and fabrication process of LEDs is to achieve ohmic contacts to p-type GaN films with high material-quality [119], good

adhesion and low-resistivity [120,121]. Ohmic contacts to n-GaN are straight forward with metallization schemes like Ti/Au, Ti/Al, Ti/Al/Ni/Au [121]. However, realization of ohmic contacts to p-type GaN is still challenging, mainly due to two factors. First, in order to favour tunnelling through the Schottky barrier, Mg doping needs to be as high as in the order of 10^{19}-10^{20} cm^{-3} which is limited by solubility limit of Mg in GaN [122]. Moreover, to get low enough access resistance, it is necessary to reach a room temperature (290 K) hole concentration in the order of 10^{17} cm^{-3}, which is also limited by the high activation energy of Mg acceptor level in GaN (180 to 230 meV) [123]; and second, the non-availability of suitable metals with high work function and Fermi level close to the valence band maximum [121]. One of the main challenges to grow p-GaN on MQW with high In-content is to avoid phase segregation of In from the MQW due to the effect of high p-GaN growth temperature during the growth [1]. Hence, p-GaN for high In-content LEDs must be grown at temperature lower than the conventional GaN growth temperature. So, the study of p-GaN growth at low temperature; doping, thickness and contact performance of p-GaN for these In-rich InGaN-based devices is still important. In this thesis work, a comprehensive study has been carried out on the epitaxial growth of p-GaN for the realization of a low-resistance p-type ohmic contact that could be suitable for In-rich InGaN-based devices such as green LEDs.

4.4.1 Optimization of thickness, surface characteristics and doping of p-GaN

A sufficient total p-GaN thickness is required to accommodate a very highly doped cap layer with a high density of dopants that will provide barrier lowering [124] and thus reduce the specific contact resistivity. However, further increasing the thickness causes poor material quality and the generation of dislocations and

scattering in carrier transport that increases the resistivity [125]. Two representative samples of p-GaN grown at temperatures of 850 ^{o}C (sample A) and 1000 ^{o}C (sample B), both of 200 nm total thickness (150 nm nominally doped followed by 50 nm heavily doped), were analyzed by SEM and AFM to investigate the surface morphology.
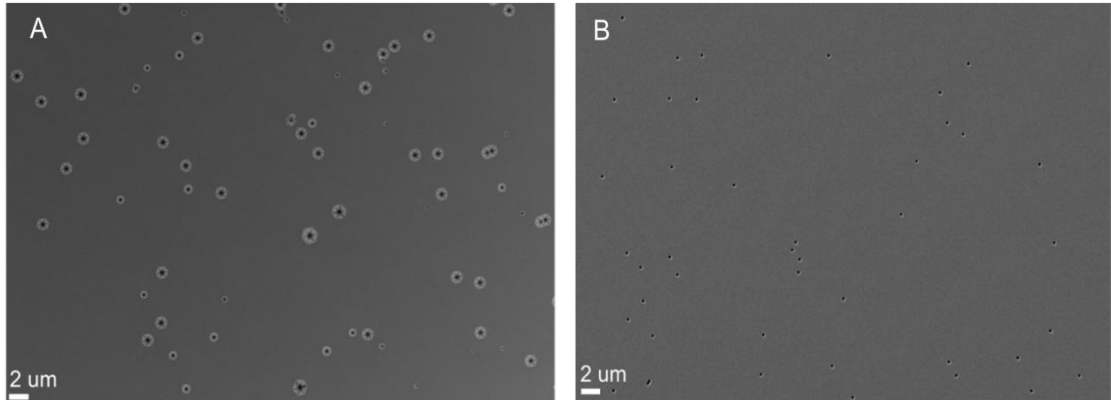
Figure 69 : SEM surface morphology of p-GaN: sample A, 850 ^{o}C growth temperature (left) and sample B, 1000 ^{o}C growth temperature (right).

Figure 69 shows the SEM images of the two samples. It can be clearly seen that sample A has bigger V-pits than sample B, which is attributed to the degraded crystal quality due to lower growth temperature of GaN [123]. The V-pit density for sample A and sample B were counted to be 5.5×10^6 cm^{-2} and 1.8×10^6 cm^{-2}, respectively. The AFM yields RMS roughness of 2.5 nm and 1.9 nm respectively for a 5×5 μm^2 scan area. These results indicated that higher growth temperature provided better surface morphology.

Figure 70 shows the SIMS results for sample A and sample B. Sample A had Mg concentration of 1.7×10^{20} cm^{-3} on average in the heavily doped p-GaN layer and 7×10^{19} cm^{-3} on average in the moderately doped p-GaN layer.
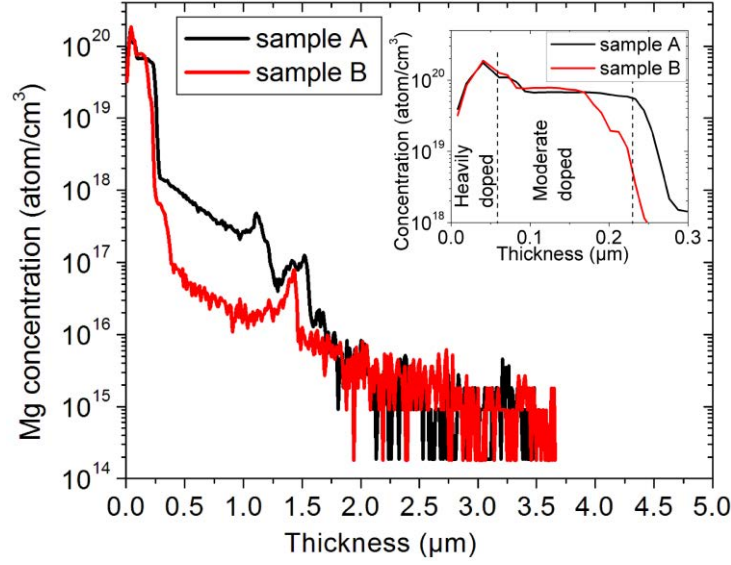
Figure 70 : SIMS result for p-GaN samples: sample A (850 °C growth temperature) and sample B (1000 °C growth temperature). The inset shows the heavily doped p-GaN layers.

Sample B had Mg concentration of 1.3×10^{20} cm^{-3} on average in the heavily doped p-GaN layer and 4×10^{19} cm^{-3} on average in the moderately doped p-GaN layer. These results imply that reducing the growth temperature to 850 °C did not change the Mg concentration dramatically. However, in SIMS result, slight p-GaN apparent thickness increase for sample A is visible (Figure 70, inset), which is attributed to the rougher surface with bigger V-pits and slight growth rate variation. As we discuss later, this high Mg concentration helps to reduce the space charge extension in the cap layer, but it is probably too high in the moderately doped layer for obtaining higher mobility values and hence lower p-GaN resistivity. Even though the high-temperature-grown sample shows better crystal quality, to avoid thermal load on the MQW underneath [125], we need to limit the growth temperature of p-GaN which is the reason that we have chosen 850 °C as the best compromise.

4.4.2   Optimal carrier concentration in p-GaN

The three main parameters governing p-contact performance are the doping level in the p-type GaN, choice of p-contact metal alloys and the annealing conditions. As mentioned already, to realize an ohmic contact to the p-GaN, it is necessary to have Mg concentration in the order of 10^{19}-10^{20} cm^{-3} to get hole concentration in the order of 10^{17} cm^{-3}. Sets of samples with different growth temperatures of 730 ^{o}C, 800 ^{o}C, 850 ^{o}C and 1000 ^{o}C with same total p-GaN thickness of 200 nm were epitaxially grown and analyzed by Hall measurements.
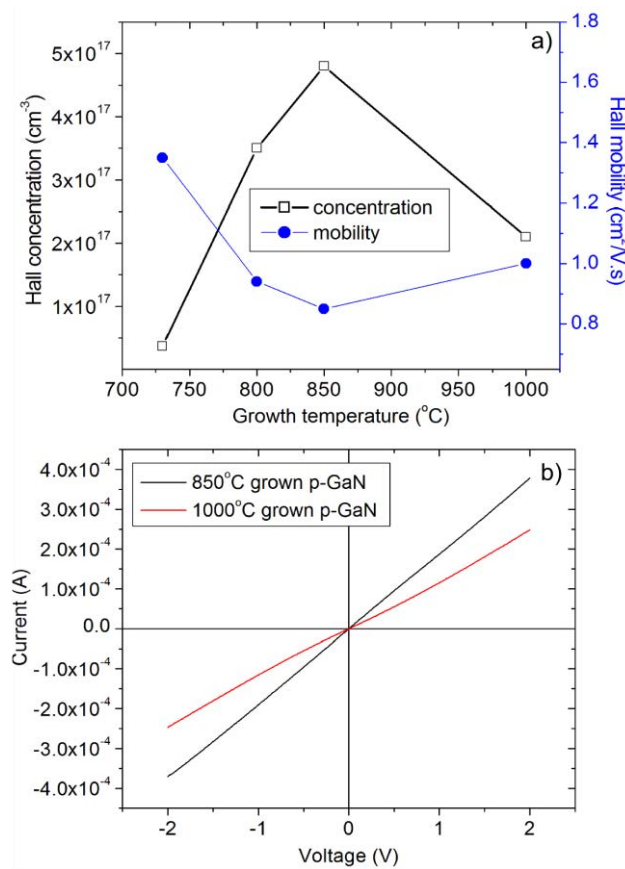
Figure 71 : Carrier concentration and mobility from Hall measurement as a function of growth temperature (a) and *I-V* curves for the samples grown at 850 ^{o}C and 1000 ^{o}C temperature (b).

In order to limit self-compensation [126,127], 150 nm moderately doped p-type GaN and 50 nm highly doped p-type GaN thickness were maintained to provide a good ohmic contact. The carrier concentration and carrier mobility measured are shown in

Figure 71. We obtained hole concentration of 4.8×10^{17} cm^{-3} and 2×10^{17} cm^{-3} and Hall mobility of 0.85 cm^2/V.s and 1.0 cm^2/V.s for 850 ^{o}C and 1000 ^{o}C grown samples, respectively. Hall concentration increases with growth temperature up to 850 ^{o}C, because of increased Mg activation by breaking of Mg-H bonds and then decreases for higher temperature, which can be attributed to self-compensation [127]. The mobility shows reverse behaviour as expected except at temperature of 1000 ^{o}C, lower defect and impurity densities result in slightly higher mobility at 1000 ^{o}C temperature.

This also gives a relationship between p-GaN growth temperature and its corresponding resistivity: The resistivity decreases up to 850 ^{o}C and again increases up to 1000 ^{o}C. These results are also supported by current versus voltage (*I-V*) curves (Figure 71b), that show higher current hence lower resistance for the 850 ^{o}C grown p-GaN.

4.5   Epitaxial growth of the complete LED structure

After the optimization of In$_{0.05}$Ga$_{0.95}$N "semi-bulk" buffer, In$_{0.15}$Ga$_{0.85}$N/ In$_{0.05}$Ga$_{0.95}$N MQW and p-GaN; the complete LED structure (Figure 41) were grown in one single epitaxy run. The SEM and AFM images of the complete epi-wafer LED structure are shown in Figure 72. The surface pits in the p-GaN layer are the result of low growth temperature (850 ^{o}C) of p-GaN. The p-GaN growth temperature was kept low to minimize the thermal budget on the MQW underneath.
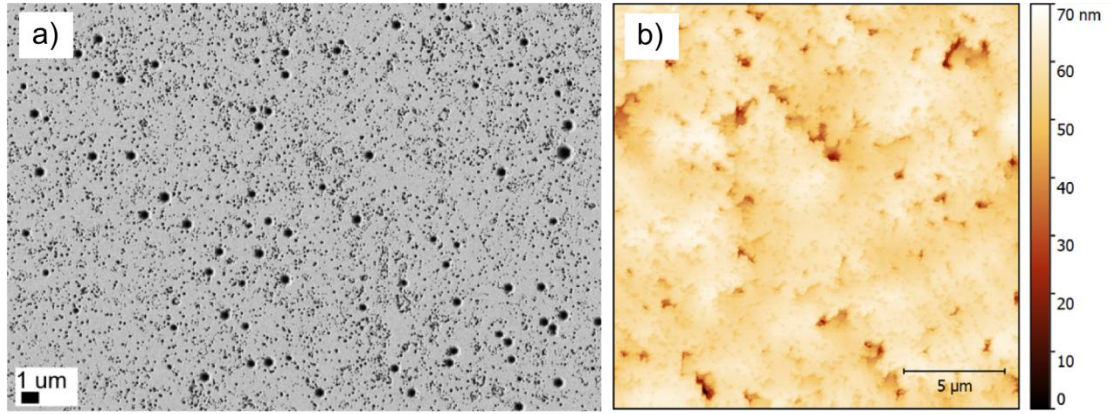
Figure 72: SEM (a) and AFM (b) images of the complete LED structure.

From AFM, the RMS roughness of a 20 × 20 μm² scan area was 10 nm. In the LTCL

experiment, the MQW emission peak was visible at 459 nm (Figure 73a).
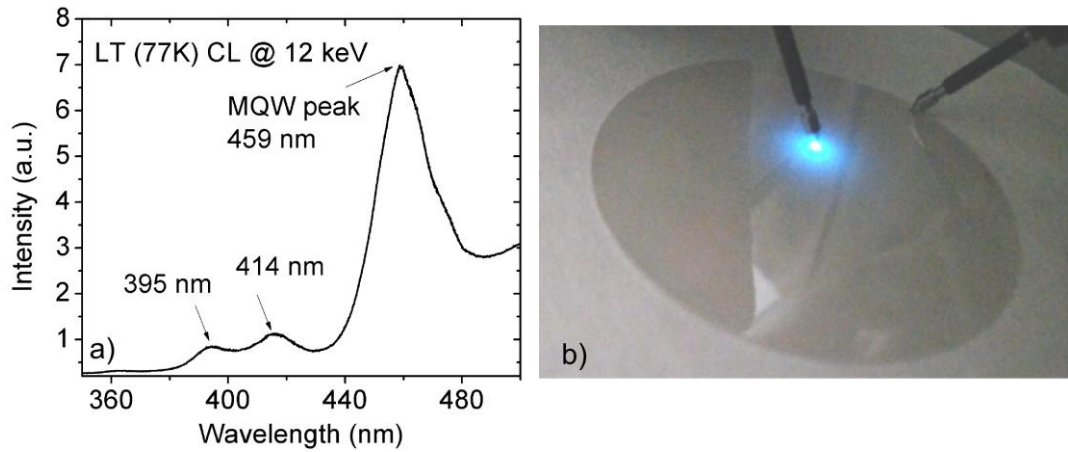
Figure 73: LTCL spectra of the complete LED structure (a) and emission from the epi-wafer LED by electrical probe test (b).

The SB emission peak was at 395 nm and the Mg related emission from the p-GaN

was at 414 nm (Figure 73a). From the XRD 2θ-ω scan data, the average In-content in

the SB and in the barrier was 6±1% and in the well was 15±1%. The epi-wafer LED

was scratched to reach down the n-GaN and then indium metal contact was deposited

by soldering to make n-contact in the scratch and p-contact in some other place on the

wafer surface. A bias voltage of 5 V to 12 V was applied and cyan light emission was

observed (Figure 73b).

CHAPTER 5.   PROCESSING OF LEDS GROWN ON "SEMI-BULK" BUFFER

The epi-wafer LEDs were technologically processed by conventional chip (CC) process. The n-contact, p-contact, and other processing steps were optimized to achieve the best optical output power and EQE.

5.1   Optimization of p-contact

Following the optimization of the p-GaN in epitaxy, it is necessary to choose suitable metal contacts and optimized annealing condition to have an ohmic p-type contact. Several groups have proposed p-type contacts based on metals like Pd, Au, Ag, Pt, Ni and alloys like Ni/Au [123], Pt/Au [121], Pd/Au [128], Ag/Pd [45], Pd/Ir/Au [129], or Pd/Ni/Au [130] and have achieved specific contact resistivity as low as 10^{-4}-10^{-6} $\Omega.cm^2$. They have attributed this low specific contact resistivity to one or more factors like surface preparation, metal deposition technique, annealing technique [131], and increase of holes due to the creation of acceptor-like gallium (Ga) vacancies [132]. However, regarding carrier transport mechanism in p-contact with low specific contact resistivity, differing theories have been proposed such as trap-assisted tunnelling enhanced by nitrogen vacancy related defects [127], tunnelling of carriers through Schottky barrier [120,128,133], thermionic emission (TE) [134], thermionic field emission (TFE) [120,135], or carrier transport through deep-level-defect (DLD) band [127,136]. Therefore, it is still important to study the p-contact metallization process, particularly for In-rich InGaN-based device structures, and to understand the carrier transport through the metallic contacts. In this thesis work, we have studied p-contact processing for the realization of a low-resistance

ohmic contact that could be suitable for In-rich InGaN-based devices such as green LEDs.

5.1.1 p-contact metal alloys

A multilayer Pd/Ag/Ni/Au metal contact was used as p-contact in our case. First, a thin layer of Pd was chosen which has large work function of 5.12 eV [121]. Even though Ag has a lower work-function, it has been shown to give excellent ohmic contacts in conjunction with Pd, once annealed. Song *et al*. observed, with Auger Electron Spectroscopy, Ga out-diffusion and possible reaction with Pd and Ag [137]. Ag has also a very high reflectivity which we used to obtain light emission through the sapphire substrate. Ni on top of the Ag acts as a diffusion barrier for protecting the top Au electrode.

After processing, depositing and annealing the p-contact, the contact was studied by XRD and morphologically by AFM. It has been reported that Pd diffuses slightly into the GaN through surface oxide and reduces the Schottky barrier height [124,128].
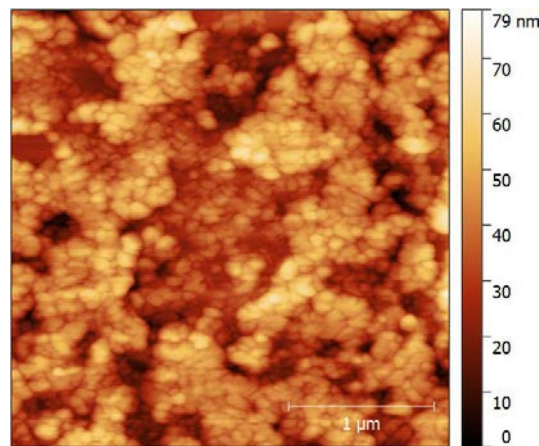
Figure 74 : AFM morphology of the complete LED structure with processed p-contact.

Thin Ag as interlayer has also been used to improve the adhesion and reduce specific contact resistivity of the Pd contact to GaN [137]. The stabilizing role of the Ni layer is confirmed by the absence of big voids in the Au surface that is clearly seen in the AFM image of the contact surface (Figure 74).
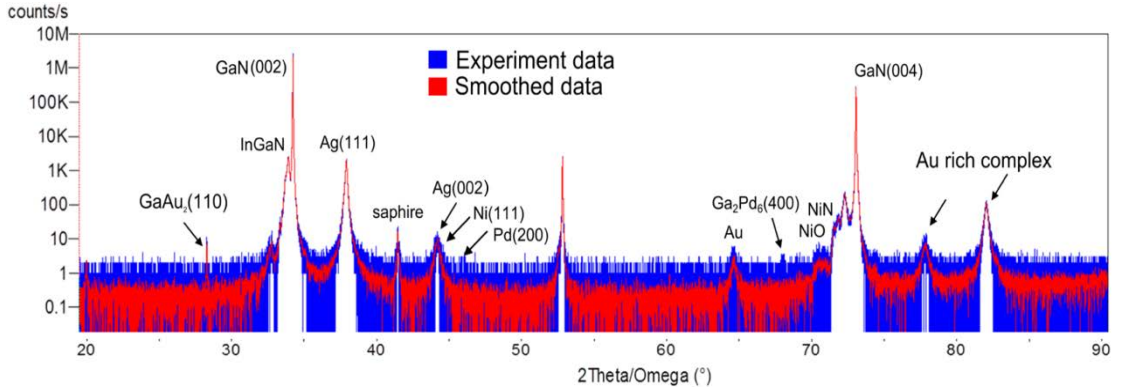
Figure 75: HR-XRD (002) 2θ-ω scan of the complete LED structure with processed contacts.

The HR-XRD 2θ-ω scan of the complete LED structure with processed contact is shown in Figure 75. Ag atoms tend to organize along (111) direction which is the energetically preferred direction and this trend is enhanced by annealing. Partial oxidation of Ni produces NiO which underlines the penetration of oxygen in the alloy enhanced by the annealing conditions.

5.1.2   Resistivity of the p-contact

5.1.2.1   Transfer length model (TLM)

The transfer length model (TLM) is the most widely used model to calculate the specific contact resistivity and thus to assess the quality of metal contacts. First proposed by Shockley *et al*. [138] and then improved by Murramann and Widmann [139], Reeves and Harrison [140], TLM has been used with rectangular or linear
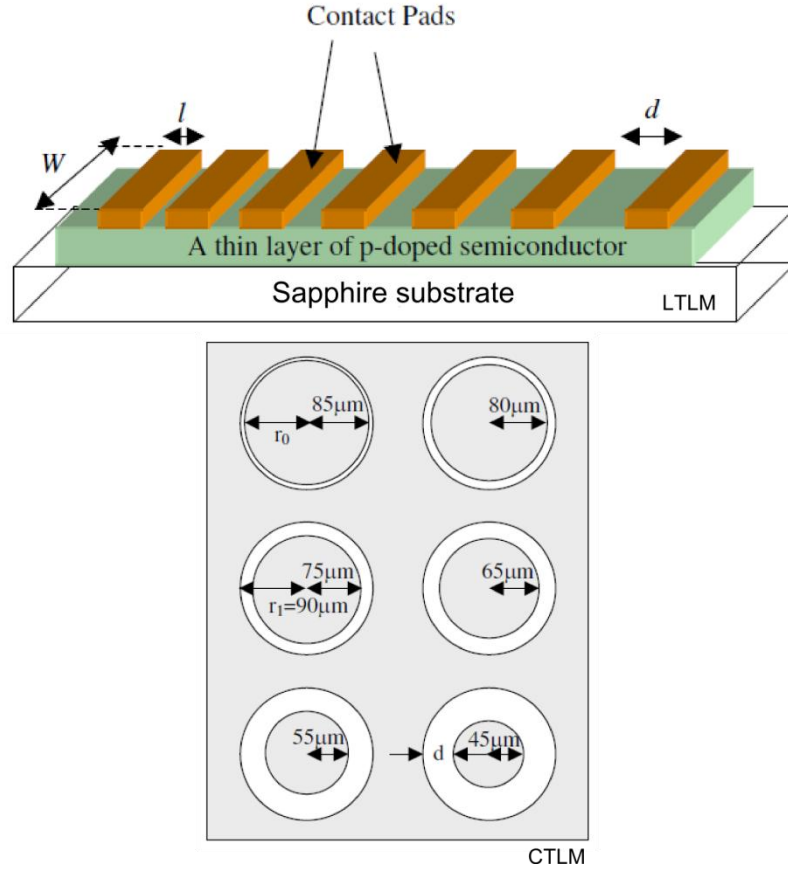
Figure 76: Typical contact patterns for LTLM and CTLM.

(LTLM) and concentric circle (CTLM) metal contacts to obtain the semiconductor layer sheet resistance R_{sh}, and the specific contact resistivity ρ_c. The R_{sh} can be calculated by the equation [141],

$$R_{sh} = \frac{\rho}{t}$$

Where, ρ is the resistivity of the semiconductor and t is the thickness of the semiconductor layer. R_{sh} is usually expressed as ohms per square ($\Omega/\square$). Typical contact patterns used for evaluating the specific contact resistivity by LTLM and CTLM are shown in Figure 76. In LTLM, rectangular ohmic metal contacts are placed over a semiconductor mesa pad, shaped as a linear array, with increasing distances between the adjacent pads d_i ($d_1 < d_2 < ... < d_i$).

The second type of transfer length model is the circular transfer length model (CTLM). The CTLM metal contacting eliminates the need of the mesa etching of the epitaxial layer for current restriction, and also the errors related to the lateral current crowding and gap effect. The refined CTLM method by Rechid and Heime [142] uses several number of concentric circles with different inner and outer radii. In this thesis work, mainly CTLM patterns were used (Figure 77).
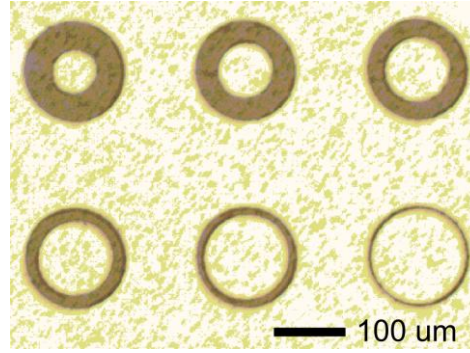
Figure 77: C-TLM patterns used in this thesis work.
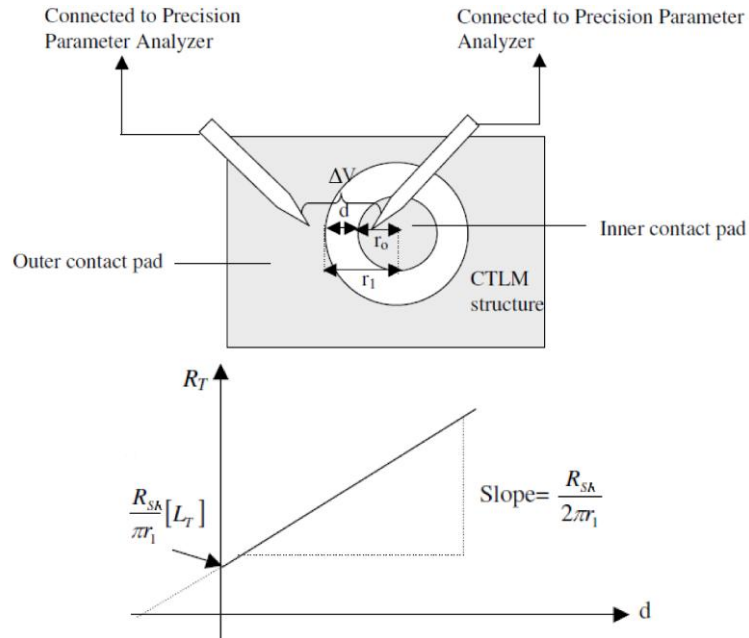
Figure 78: Typical experimental setup for extraction of specific contact resistance (top) and plot of total resistance R_T versus gap size d (bottom).

From the experimental CTLM setup shown in Figure 78 (top), if the voltage drop and the current flowing across the metal contacts are ΔV and i_o respectively, L_T is the transfer length, r_o and r_1 are the inner and outer radii, then,

$$L_T = \sqrt{\frac{\rho_c}{R_{sh}}}$$

Where, R_{sh} is the sheet resistance and ρ_c is the specific contact resistivity.

Considering that r_o and r_1 are much greater than L_T (in practice, at least by a factor of 4), and using the Bessel function approximation, the ΔV can be expressed as [141],

$$\Delta V = \frac{i_o R_{sh}}{2\pi} \left(\ln\left(\frac{r_1}{r_1 - d}\right) + L_T \left(\frac{1}{r_1 - d} + \frac{1}{r_1}\right) \right)$$

The total resistance R_T is given by,

$$R_T = \frac{\Delta V}{i_o}$$

And, hence,

$$R_T = \frac{R_{sh}}{2\pi} \left(\ln\left(\frac{r_1}{r_1 - d}\right) + L_T \left(\frac{1}{r_1 - d} + \frac{1}{r_1}\right) \right)$$

Since $2\pi(r_1 - d) \gg d$, it can be written,

$$R_T = \frac{R_{sh}}{2\pi r_1} (2L_T + d)$$

Using least squares fit of the experimental data, L_T and R_{sh} can be calculated by the equations (Figure 78, bottom),

$$L_T = (y\ interception/slope) \times 2$$

And,

$$R_{sh} = (slope) \times 2\pi r_1$$

Then the specific contact resistivity (ρ_c) is,

$$\rho_c = L_T{}^2 \times R_{sh}$$

5.1.2.2   Study of p-contact performance by CTLM

The contact performance was studied by circular transfer length model (CTLM). The gap sizes (*d*) were 3.35 μm, 8.52 μm, 13.8 μm, 19.1 μm, 23.6 μm and 28.7 μm. The current-voltage curves for different gap sizes are shown in Figure 79. The current decreases with increasing gap sizes because it has to flow through a longer p-GaN path, with higher resistance. However, for all gap sizes, the contacts show ohmic behaviour. The specific contact resistivity of p-GaN for the optimum anneal of 575 °C was 6.2×10^{-4} Ω.cm^2, calculated from fitting, which corresponds to a sheet resistance of 384 kΩ/□. This low contact resistance with O$_2$ annealing is attributed to mainly three facts; creation of acceptor like Ga vacancies [135], freeing of more Mg acceptor by breaking Mg-H complex [143], and more inter-diffusion and interface reaction between contact metals and GaN that reduces the Schottky barrier or enhances the tunneling effect. Interface reaction of Ag and Pd with GaN may lead to the formation of Ga vacancies (V$_{Ga}$) forming Ag-Ga [120]. The as-deposited sample showed higher sheet resistance and higher specific contact resistivity whereas the annealed sample showed ohmic behaviour with very low specific contact resistivity.
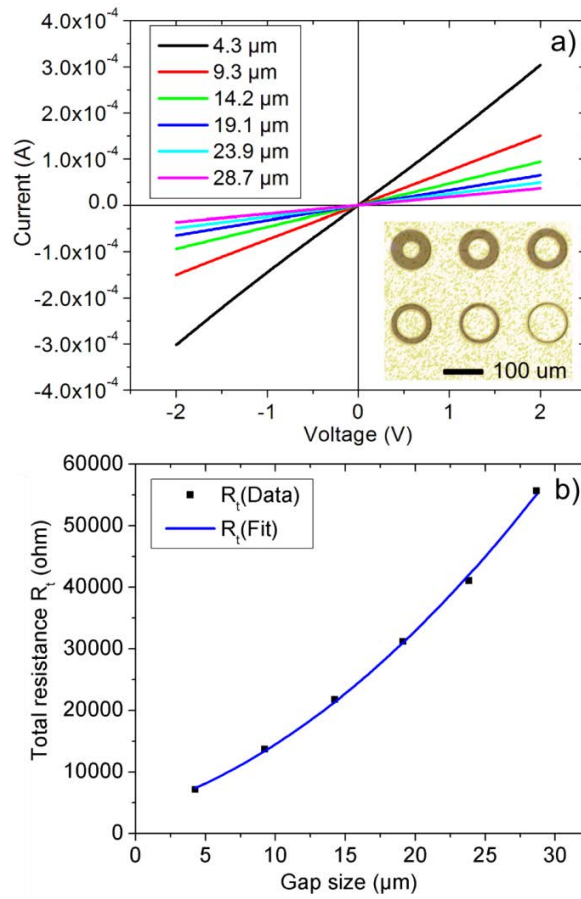
Figure 79 : Result of CTLM experiment for p-GaN contact: *I-V* **curves for different gap sizes (a) and gap size versus measured total resistance (b), the blue curve represents the fit used to extract the specific contact resistivity and sheet resistance.**

First principle calculations by Jiao *et al*. showed barrier height dependence on the dopant position whereas the barrier height can go to zero for sufficient doping in the vicinity of the metal contact [124]. Using the deep level barrier model of Tung [144], they reported that, for surface density of dopant levels of $>10^{14}$ cm^{-2}, Schottky barrier lowering effect should be observed. At this level of doping, the space charge region will be very thin and the tunneling effect will be highly enhanced. Kwak *et al*. also reported about deep level defects and their role to obtain low contact resistance [145]. Our 50 nm of p+ GaN with dopant concentration of ~2 × 10^{20} cm^{-3} corresponds to an active surface density of 10^{15} cm^{-2} which may explain the Schottky barrier height lowering in our case. The good ohmic contact may be due only to the efficient

tunneling effect. Moreover, at such high doping level, supposing a large part of the Mg is substituted, the acceptor level gets closer to the valence band (impurity sub-band).

We believe that the initial Schottky barrier height of 2.38 eV between Pd and p-GaN is lowered or even vanishes through the deep level acceptors and shallow dopants in intimate proximity with the metal. So, the ohmic behaviour comes from the presence of the high doping level in the vicinity of the metal contact, which is enhanced by the annealing and the diffusion of the contact metals as our low p-GaN growth temperature of 850 °C promotes the incorporation of more Mg [146].
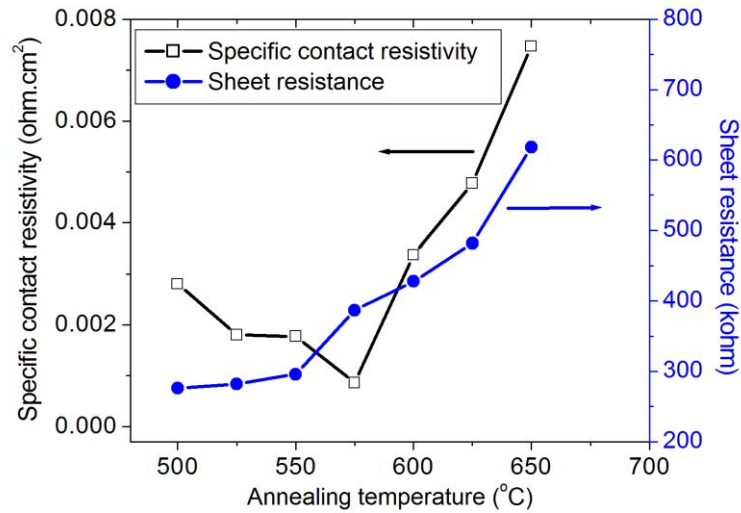
Figure 80 : Specific contact resistivity and sheet resistance versus contact annealing temperature.

Figure 80 shows the specific contact resistivity ρ_c and sheet resistance R_{sh} versus annealing temperature curves for different contact annealing temperatures. The annealing temperature necessary to lower the contact resistivity depends on the doping level and microscopic structure of the p-GaN. The R_{sh} increases with higher annealing temperatures. This could be due to the compensation of the shallowest

dopants induced by oxygen penetration into the moderately doped p-GaN. The specific contact resistivity decreases while increasing the annealing temperature up to 575 °C. However, annealing temperature higher than 600 °C deteriorates the specific contact resistivity.

The complete high In-content LED structure with processed contacts was electrically tested for contact performance validation. The turn-on voltage was less than 3.5 V. The emission wavelength was in the range from 450 nm to 480 nm, in the blue to cyan spectra. Optimization of growth and processing for longer wavelength emission are subject of current study. Leakage current of $\sim 10^{-3}$ A was observed for reverse bias presumably for the rough surface of p-GaN, where some of the large V-pits reaching the n-GaN could act as a leakage current path. However, reasonable surface roughness is necessary for higher light extraction efficiency by reducing internal reflection [147]. Further improvement and investigations on these issues are ongoing.

5.1.3 *Optimization of n-contact*

As discussed before, ohmic n-contact to n-GaN is much more straightforward to realize compared to p-contact. Even though there are some short-comings, such as oxidization, possible formation of nitrogen vacancies [148]; titanium (Ti), aluminium (Al) and gold (Au) based metal alloys have been effectively used for the formation of low resistivity n-contact. Specific contact resistivity as low as 10^{-7} $\Omega.cm^2$ can be achieved by suitable annealing with temperature ranging from 750 ^{o}C to 850 ^{o}C in O_2 or air ambient [148]. We have used n-contact metal scheme of 5 nm Ti on n-GaN and then 300 nm Au on top as final layer. Ti was used to match the Schottky barrier height and Au was used to avoid oxidization. The contact was then annealed at 700 ^{o}C in O_2 ambient. The specific contact resistivity was measured by CTLM, as was for p-

contact. The same gap sizes were used. The annealed contact was ohmic for almost all gap sizes (Figure 81), the total resistance versus gap sizes and the *I-V* curves are shown in Figure 81. The specific contact resistivity was 6.3×10^{-5} $\Omega.cm^2$. The sheet resistance was 51.1 $\Omega/\square$.
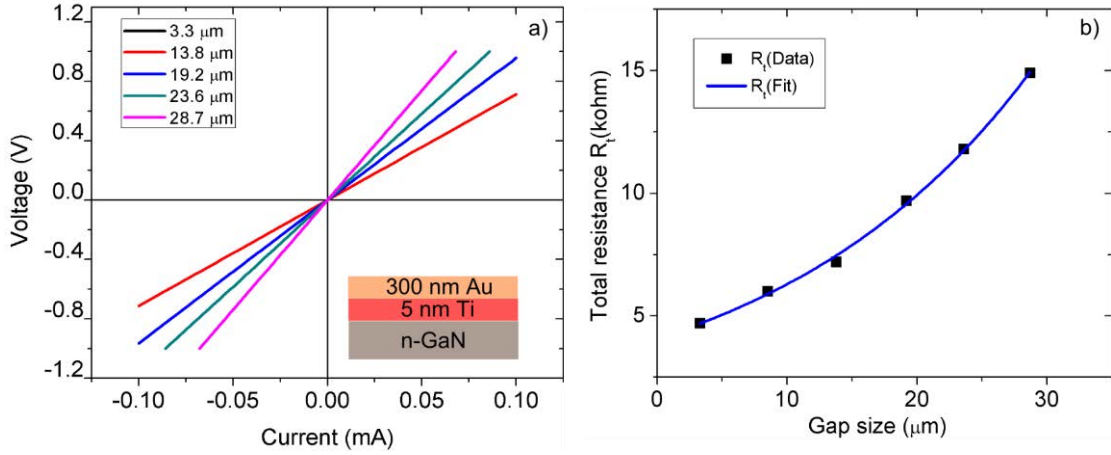
Figure 81: *I-V* **curves for different gap sizes for our Ti/Au n-contact (a) and the plot of total resistance (R$_t$) versus gap sizes (b).**

5.2 The steps of technological processing of the epi-wafer LEDs

The technological processing of our epi-wafer LEDs was done at CEA-Leti. The technological processing and the electrical test result of the LED structures grown on InGaN SB buffer will be discussed briefly in this section. The steps of the processing flow are shown in the flow chart of Figure 82. The processed LED structure is shown in Figure 83. Since, the p-contact is not transparent, light is supposed to emit from the back side of the substrate. This requires a double side polished sapphire substrate for the best light extraction.

<u>Wafer cleaning by HCl</u>

First of all, the LED wafer was cleaned by HCl for removing surface native oxides and other contaminations (Figure 84).
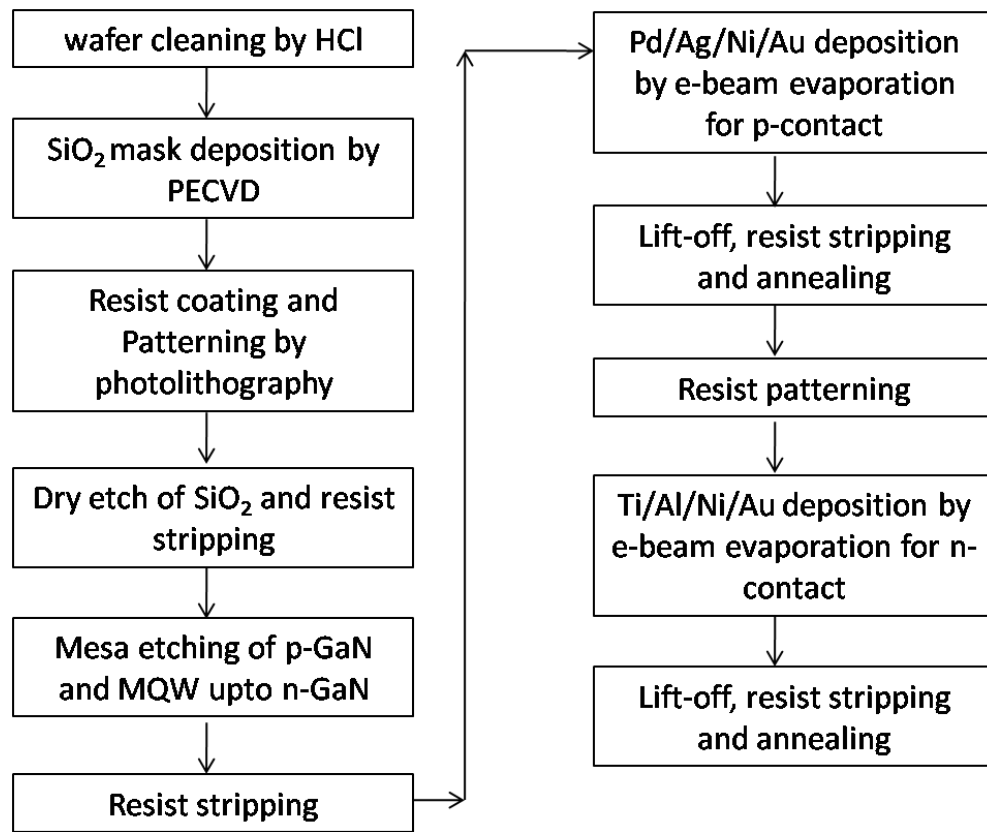
Figure 82: Flow chart of LED processing steps.
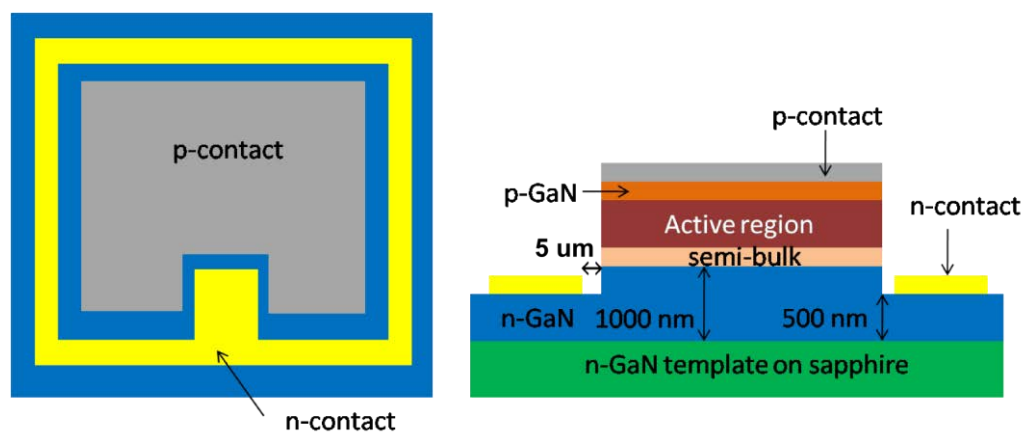
Figure 83: Top view (left) and cross-section view (right) of the processed LED structure (schematically and not to scale).

After the cleaning, SiO$_2$ mask was deposited by plasma enhanced chemical vapour Deposition (PECVD) (Figure 85).
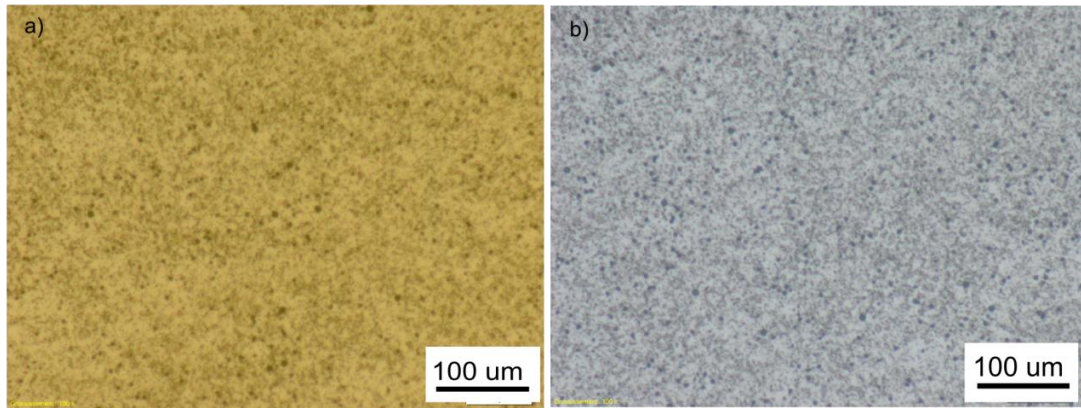
Figure 84: The LED wafer surface before (a) and after (b) HCl cleaning.
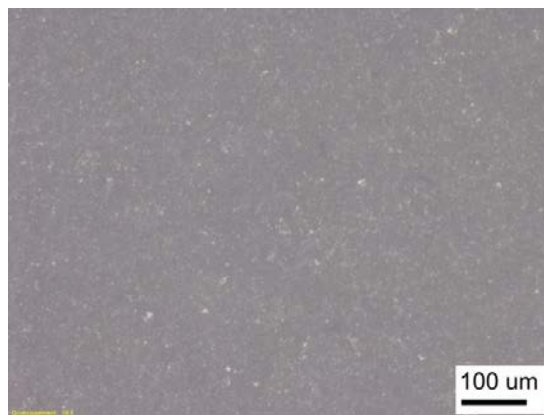
Figure 85: wafer with SiO$_2$ deposited by PECVD.

Patterning and photolithography

After the deposition of masking layer, patterning and photo lithography were done using positive photoresist. The patterns consisted of different LED devices along with CTLM and rectangular TLM patterns (Figure 86).

Etching of SiO$_2$

After photo lithography, the SiO$_2$ mask was locally etched away by fluorine dry etch (Figure 87).
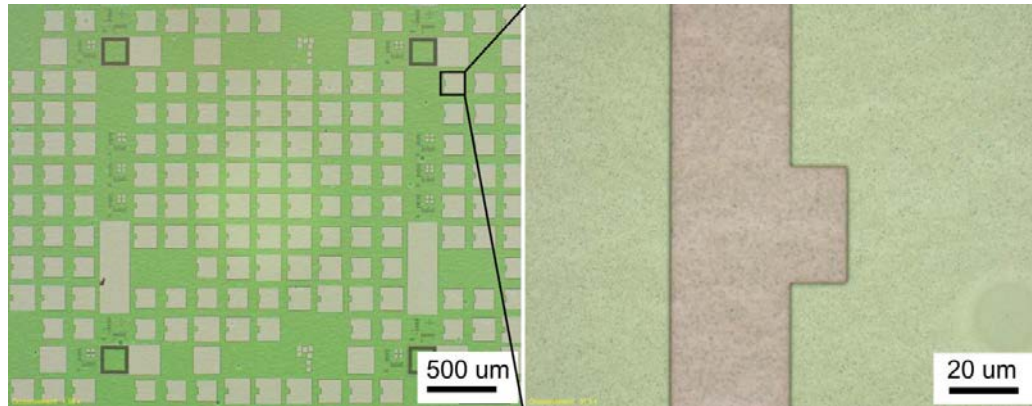
Figure 86: Patterning and photolithography of the LED wafer.
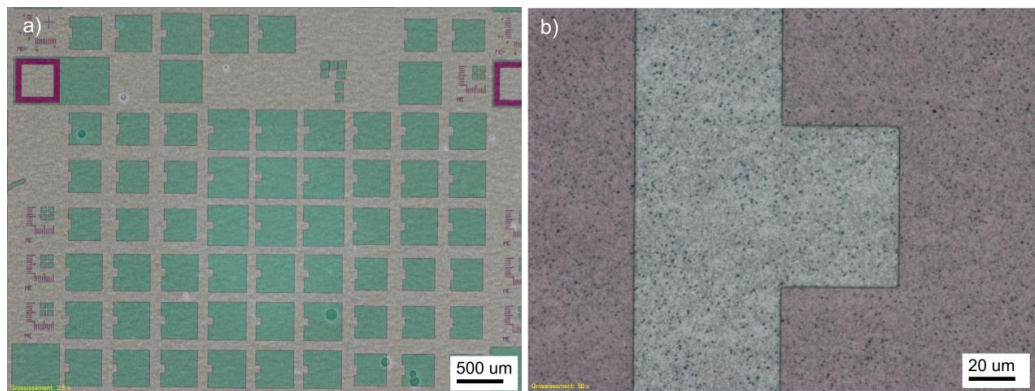
Figure 87: Wafer after etching of SiO$_2$ mask.

GaN and MQW etching

Hard mask etching was followed by etching of GaN by chlorine-based ICP etching (Figure 88). p-GaN and MQW were etched down to the n-GaN.

Resist stripping

After the GaN etch, the additional resist was stripped (Figure 89).
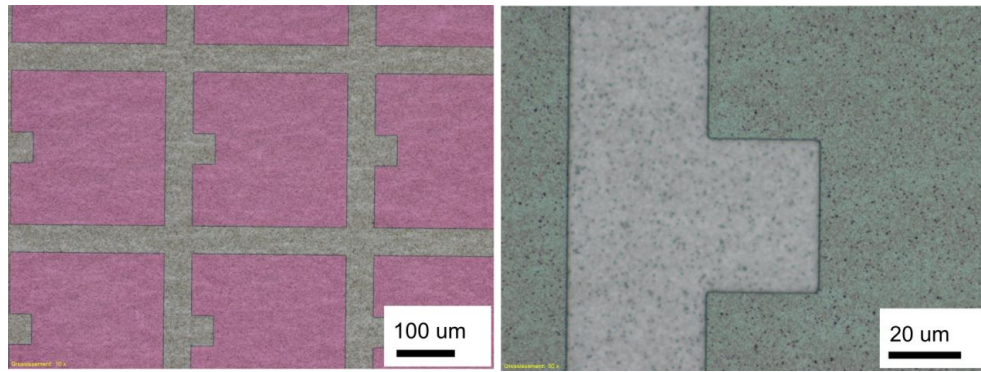
Figure 88: LED wafer after etching of GaN by ICP.
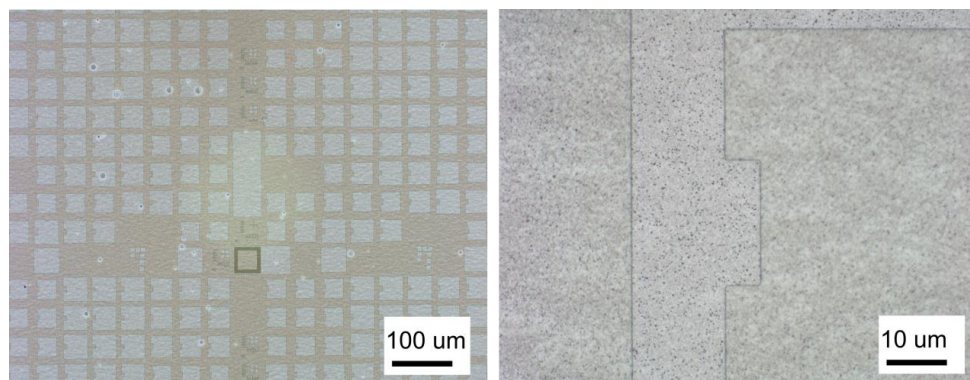
Figure 89: Stripping of resist after GaN etching.

Formation of p-contact

For p-contact realization, first, lithography was done for contact and CTLM patterning. It was followed by contact metal (Pd/Ag/Ni/Au) deposition by electron beam evapouration and then lift-off and the rapid thermal annealing in O_2 atmosphere (Figure 90).

Formation of n-contact

Similar as p-contact, first, lithography was done and then contact metal layers of Ti/Au were deposited and then lifted off (Figure 91).
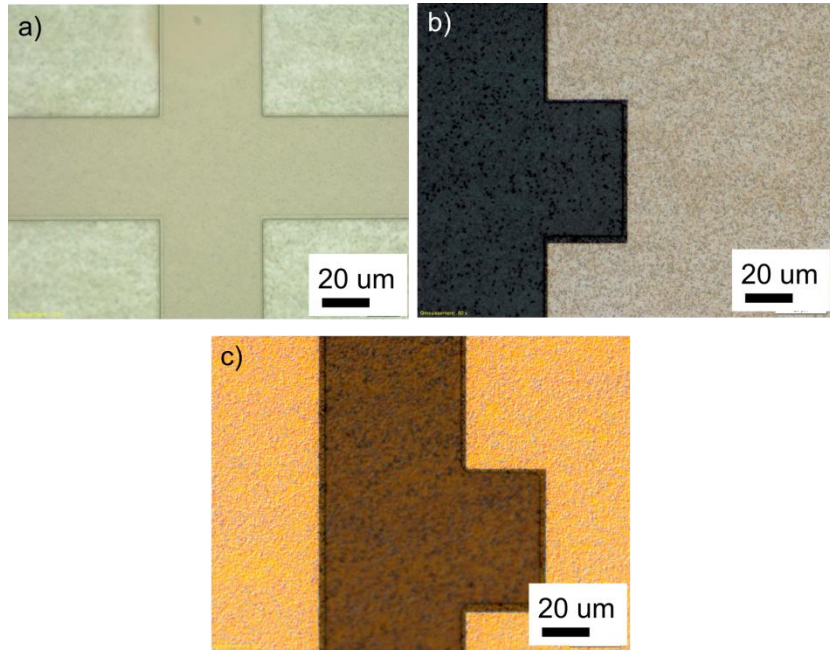
Figure 90: Optical microscope images after p-contact lithography (a), lift-off (b) and resist removal and annealing (c).
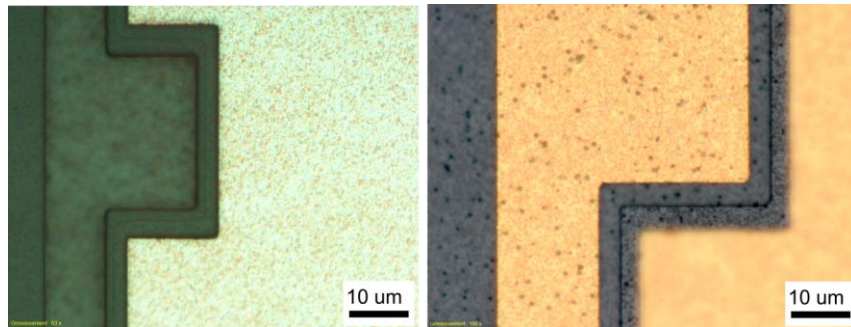
Figure 91: n-contact after lithography, metal deposition, lift-off (left), and then the resist was removed and annealed (right).

The light would be emitted from the bottom side of the substrate, making this type of contacts more suitable for double-side polished wafer rather than single-side polished ones.

5.3 Electrical test of the processed LED chips

The processed LED wafer with LED chips is shown in Figure 92. The sizes of LED chips were 225 μm^2, 250 μm^2 and 275 μm^2.
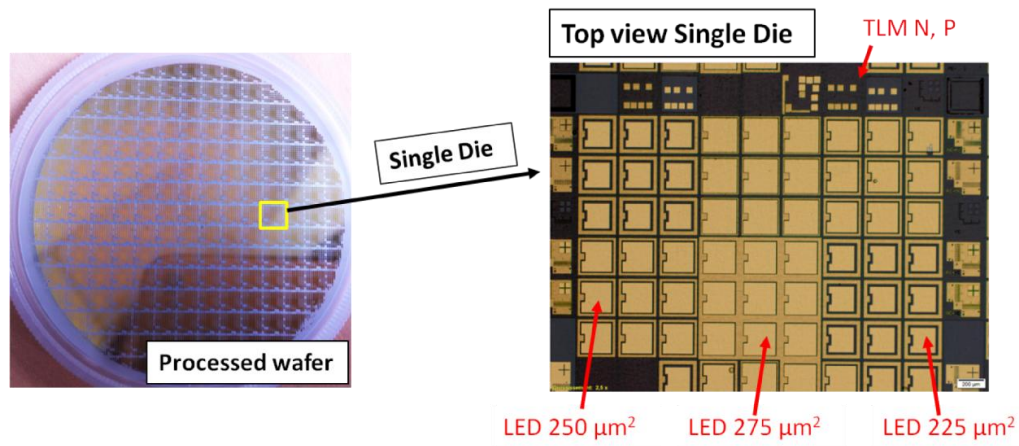
Figure 92: On-wafer processed LED chips (left) and optical microscope image of the LED chips with three different sizes (right).
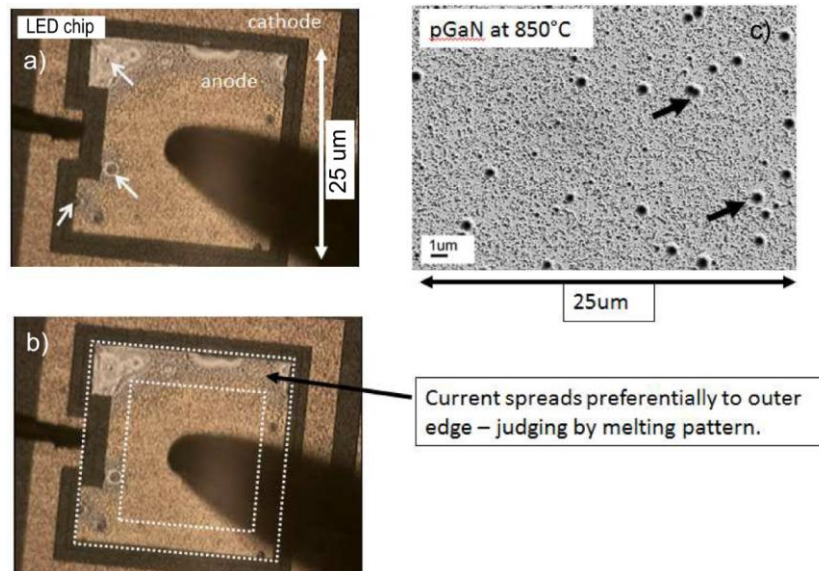
Figure 93: Voltage applied to the LED chip (a), current crowding effect in the edge of LED chip (b) and SEM image of the epi-wafer LED surface (c).

The voltage was applied gradually to the LED chips up to 10 V and maximum current density of 200 A/cm^2 (Figure 93). As the applied voltage was increased, the current crowded preferentially at the edges and around the bigger V-pits (indicated by arrows). Therefore, presumably the large and deep V-pits were responsible for the high leakage current of ~10^{-3} A. As voltage (hence current) increased, the LED emission turned on locally (Figure 94). Some zones emitted over larger voltage ranges

(white arrows), perhaps due to better local contact and material properties. Some other emitting zones were short-lived. Brightest spots were likely due to higher extraction and were associated with V-pits location. High extraction was also at mesa edge (green arrow, Figure 94, image 9).
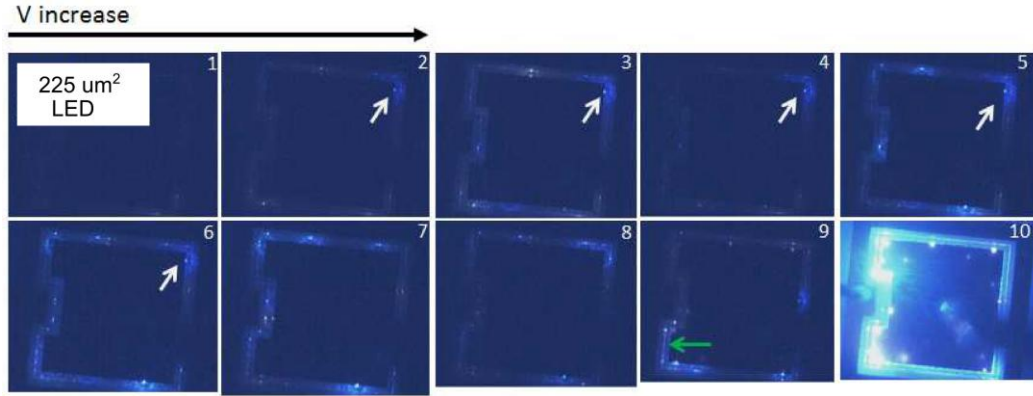
Figure 94: Turn-on of LEDs as the voltage increases (the maximum current density was 200 A/cm^2).

At a current density of 200 A/cm^2, light emission is visible (Figure 94, image 10). The colour corresponds to ~460 nm wavelength which is consistent with the PL emission wavelength.

5.3.1 Current-voltage (I-V) characteristics and leakage current

The *I-V* curve for the observation of leakage current behaviour is shown in Figure 95.

The turn on voltage was less than 3 V for concerned voltage range. The leakage current was ~10^{-3} A, slightly high value, presumably for some large V-pits reaching the n-GaN and also for the absence of electron blocking layer (EBL) in our LED structures. Moreover, it seems that the p-type metal locally migrated towards the n-type zone, possibly forming metal "fingers" along some of the emerging crystal defects, which would explain the evolution of the *I-V* curves towards Schottky-like
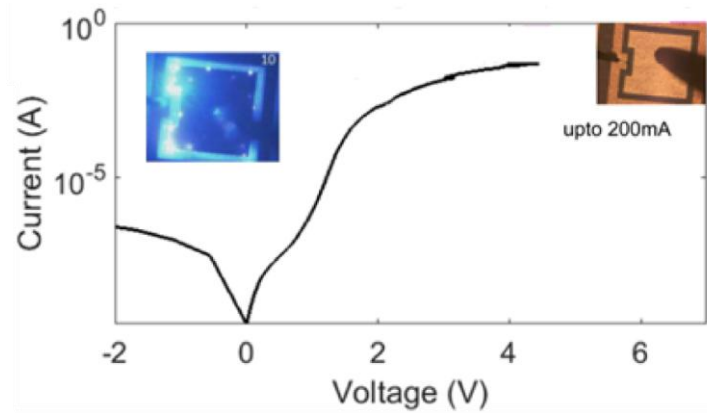
Figure 95: The leakage current for the processed LED chip.

behaviour with increasing bias voltage hence current. The absence of EBL could cause electron spill-over and hence poor carrier injection efficiency [149]. The rough p-GaN surface with some big and deep V-pits might be one of the reasons of poor electroluminescence performance of our LED chips. Another reason might be that, better optimization of the contacts in respect of transparency and light extraction performance, is required for our specific LED structure on "semi-bulk" buffer. Further optimization of the p-GaN, contacts and electroluminescence study of the LED devices are ongoing.

CHAPTER 6.   CONCLUSION AND OUTLOOK

6.1   Conclusion

To compete with conventional lighting, solid state lighting has to be intense, highly efficient and with good CRI. Throughout the thesis, the effort was to understand and find possible solution to overcome the "green-gap", and to realize a highly efficient complete LED device emitting in the intermediary wavelength in blue to green spectra, so that in future work, combining the RGB LEDs on a monolithic chip, bright and high CRI white light can be achieved.

In contrast to the conventional LED design and fabrication, we designed and epitaxially grew our InGaN-MQW structure with InGaN barrier on our so-called InGaN "semi-bulk" (SB) buffer, rather than growing on GaN buffer with GaN barrier.

Changing the barrier from GaN to InGaN, combined together with the optimum 5% In-content in the 5 nm thick barriers for an MQW with 16% indium in the 3 nm thick wells, resulted in the prediction of improved emission intensity. The predicted optimal turn-on voltage was 2.9 V for an optimum number of quantum wells of 3 or 5, and the theoretical maximum IQE was ~68% at a drive current density of 290 A/cm^2 which means actually ~170% improvement of IQE at 200 A/cm^2 compared to that of the reference MQW with GaN buffer and GaN barriers. Moreover, from the calculated radiative recombination rate, it was simulated that radiative recombination should took place in all the wells rather than only in the last well and the total radiative recombination rate should increase by ~5.8 × 10^{26} cm^{-3}s^{-1} in the case of InGaN barrier. From the simulated electron and hole distributions, it was obvious that both electrons and holes should be much more homogeneously distributed in all the wells

rather than in the last well, which is the case for GaN barrier. Due to the use of InGaN barrier, the reduced energy barrier resulted in lower calculated band bending, eventually resulting in more overlap of electron-hole wave function and hence more radiative recombination.

We simulated $In_{0.15}Ga_{0.85}N/In_{0.05}Ga_{0.95}N$ MQW-based LED structure with $In_{0.05}Ga_{0.95}N$ SB buffer along with reference LED structure with GaN buffer. At a current density of 200 A/cm^2, an improvement of 130% of room temperature IQE compared to configuration with GaN buffer and GaN barrier, and 15% compared to the case with GaN buffer and InGaN barrier, was obtained. No theoretical efficiency droop was predicted for the design with InGaN barrier grown on InGaN SB buffer at this current density compared to the reference design. The calculated luminous power for our design with InGaN SB buffer was doubled compared to reference case with GaN buffer and GaN barrier, and ~60% improved compared to reference case with GaN buffer and InGaN barrier, at this current density. This improvement is attributed to the reduction of net electric field in the well. For our final optimal structure design, 1.5 times lower electric field was calculated, compared to reference case with GaN buffer and GaN barrier, and the average electric field in the wells was 0.1 MV/μm lower as compared to that of reference design with GaN buffer and InGaN barrier. The reduction in net electric field when using SB InGaN as buffer resulted in reduced calculated band bending and hence more overlap of electron and hole wave functions for our final structure: 38.7% more overlap compared to reference case with GaN buffer and GaN barrier and 9% more overlap compared to reference design with GaN buffer and InGaN barrier was obtained.

We optimized the epitaxial growth of a ~70 nm thick "semi-bulk" buffer (realized with 2 nm GaN interlayers between every two 15 nm of InGaN layers) to obtain a high quality InGaN buffer layer with single phase In. For growing a MQW with ~16% In intended for emission in blue to cyan spectra, the SB buffer was grown with ~6% In and it was only ~8% relaxed on the GaN template underneath. The V-pit density of 8×10^6 cm^{-2}, the RMS roughness of ~3.0 nm for a 3×3 μm^2 scan in AFM, and a single CL emission peak at ~400 nm, that corresponds to ~6% In in strained InGaN, with FWHM of ~13 nm, confirmed good quality single phase SB InGaN. For InGaN/GaN and InGaN/InGaN MQW, for the same average In content in the well, extracted from XRD, for the thicker well, the CL and PL emission wavelength was longer, because of the reduction of the effective bandgap energy and increased QCSE. The thicker well also resulted in worse surface quality with more V-pits presumably for In desorption in active region. Moreover, the lower growth temperature (780 ^{o}C) resulted in more V-pits and inclusion defects compared to sample with 20 ^{o}C higher InGaN growth temperature (800 ^{o}C). The In incorporation was higher for the sample grown at low temperature, with a ~30 nm shift in LTCL emission wavelength. One way to increase the In content in the well is to increase the TMIn/III ratio. 50% increase of TMIn/III ratio gave 3% increase of In-content in the well for the fixed flow rates of other precursors and fixed growth parameters.

As a part of optimization of the MQW, samples with both GaN barrier and In$_{0.05}$Ga$_{0.95}$N barrier were epitaxially grown and compared experimentally. Using InGaN as the barrier caused degradation of the surface and increase in V-pit density and inclusion defects. However, the emission intensity was doubled with improved FWHM for InGaN barrier compared to that for GaN barrier, and the emission wavelength was blue-shifted by ~30 nm. We attribute this blue shift to the increased effective bandgap, reduced potential barrier height, reduction in QCSE and slight reduction (~2%) in average In content in wells. In low temperature (15 K) PL study,

for sets of samples with the same structure but with higher In incorporation (25%), intended for "green-gap" spectra emission, similar result as for lower In-content (15%) samples was observed. A blue-shift of ~35 nm was observed with more than three-fold increase in emission intensity and improved FWHM.

After the optimization of the $In_{0.15}Ga_{0.85}N/In_{0.05}Ga_{0.95}N$ MQW on GaN buffer, the MQW structures were grown on SB $In_{0.05}Ga_{0.95}N$ buffer. The XRD 2θ-ω scan data showed average well indium of 18±1% in the reference MQW samples with GaN buffer with GaN barrier, and of 16±1% in both the MQW samples with GaN buffer with $In_{0.05}Ga_{0.95}N$ barrier, and with $In_{0.05}Ga_{0.95}N$ SB buffer with $In_{0.05}Ga_{0.95}N$ barrier. The RMS roughness of the third sample was 3 nm, compared to 2.0 nm and 1.5 nm of the second and first reference samples, respectively, for a 5 μm × 5 μm scan area in AFM. Though using SB buffer in the final sample increased the size of the V-pits, the lower pit density and the absence of inclusion defects could be attributed to the partial reduction of localized variation of strain energy or strain balance. The PL emission intensity, when using the SB InGaN as buffer, got doubled compared to sample with GaN buffer and $In_{0.05}Ga_{0.95}N$ barrier and showed six-fold increment compared to sample with GaN buffer and GaN barrier. We believe that this improvement was definitely due to the insertion of the SB buffer layer because the second reference sample had the same MQW structure with $In_{0.05}Ga_{0.95}N$ barrier, with the only difference that our final structure had $In_{0.05}Ga_{0.95}N$ SB buffer beneath the MQW. The room temperature IQE for our final sample was calculated to be 67.5% by considering the radiative recombination efficiency to be 100% at 15 K. The integrated PL intensity versus $1/T$ curves revealed the reduced effect of non-radiative recombination channel for our final sample.

The fully-strained high quality $In_{0.05}Ga_{0.95}N$ SB buffer layer did not degrade the surface quality of the $In_{0.15}Ga_{0.85}N$/ $In_{0.05}Ga_{0.95}N$ MQW grown on top. For the optimal number and thickness of quantum wells, the stack was not sufficiently thick to relax when grown without InGaN SB buffer. However, the complete structure started to relax partially (~20%), as seen in the RSM. No significant increase in average In incorporation was visible in EDX scan which was consistent with the XRD result, where the average In incorporation in wells of both the reference sample and the final sample was similar (~15%). For both LTCL and LTPL, ~15 nm red-shift of emission wavelength was observed for the final $In_{0.15}Ga_{0.85}N$/$In_{0.05}Ga_{0.95}N$ MQW on $In_{0.05}Ga_{0.95}N$ SB buffer compared to the sample on GaN buffer. Depth resolved CL showed only ~4 nm peak wavelength variation for our final sample from top to bottom of the QWs, suggesting much lower compositional pulling effect. From the dependence of emission wavelength on the PL excitation power, it was concluded that the QCSE for our sample was at most equal (if not less) to that of the reference sample. In the PL experiment, a clear indication of increase in emission intensity has been seen in the final sample, which is attributed to the reduced electric field, and hence reduced band bending, and also possibly to the interface roughness which may have reduced the non-radiative recombination. The red-shift was more dominant than the band-filling induced blue-shift at this excitation power density of 1.30 mW/cm^2.

The HAADF-STEM images confirmed the designed width and clear interface of the layers for our final MQW sample with $In_{0.05}Ga_{0.95}N$ SB buffer and $In_{0.05}Ga_{0.95}N$ barrier. However, no significant In-rich clusters were visible. Out-diffusion of indium from the wells caused thickness increase in some locations of wells, particularly in the last QW, that changed the confinement energy state and may have contributed the most to the red-shift for our MQW sample with SB buffer. The effect of thickness

variation on emission wavelength was simulated and we have estimated that the thickness of our QW might have increased by 0.5 to 1 nm in the final InGaN/InGaN MQW sample on InGaN SB buffer compared to the reference InGaN/InGaN MQW on GaN buffer.

The p-GaN layer for high indium content InGaN MQW applications was optimized by variations of growth temperature, precursor CP_2Mg flow rate, and III/V ratio. At growth temperature of 850 ^{o}C, the optimized thickness was 150 nm for the p-type GaN layer with moderate Mg doping, and 50 nm for contact layer with high Mg doping concentration. Hall measurement yielded hole concentration of 4.8×10^{17} cm^{-3} for the optimized sample. SIMS showed Mg concentration of 1.7×10^{20} cm^{-3} on average in the heavily doped layer, and 4×10^{19} cm^{-3} on average in the moderately doped p-GaN layer for the optimized p-GaN, which are comparable to the state of the art values that are in the order of $\sim 10^{20}$ cm^{-3} [150,151]. A multilayer Pd/Ag/Ni/Au metal contact was deposited on this p-GaN. Optimization of both p-GaN layers and p-contact processing led to a low resistance contact with specific contact resistivity of 6.2×10^{-4} Ω.cm^2 and sheet resistance of 384 kΩ/□. The optimized p-type contact annealing temperature was 675 ^{o}C. Our optimized n-contact was 5 nm Ti on n-GaN and then 300 nm Au on top as final layer with contact annealing at 700 ^{o}C in O_2 ambient. For n-contact, the specific contact resistivity was 6.3×10^{-5} Ω.cm^2 and the sheet resistance was 51.1 Ω/□.

The technological processing steps for conventional chip (CC) process of our epi-wafer LEDs were optimized. The steps to realize LED chips were cleaning by HCl, SiO$_2$ deposition, pattering and lithography, etching of SiO$_2$, GaN etching, resist stripping, p-contact and n-contact deposition, lift-off and contact annealing. The sizes

of the processed LED chips were 225 μm^2, 250 μm^2 and 275 μm^2. As the applied voltage was increased up to 10 V and to maximum current density of 200 A/cm^2, the current crowded preferentially at the edges and around the bigger V-pits. Presumably the large and deep V-pits on the p-GaN were responsible for the high reverse bias leakage current of ~10^{-3} A, by creating short circuit path reaching the n-GaN. The absence of electron blocking layer in our LED structure might also be a reason of high leakage. The brightest spots were likely due to higher extraction and were also associated with V-pits locations. The LED turn-on voltage was less than 3 V for the concerned current density range. The emitted light was of cyan colour that was consistent with the PL emission wavelength of ~460 nm.

6.2 Perspectives

6.2.1 *Optimization of high In-content MQW for deep green emission*

We will further optimize the InGaN/InGaN MQW with more In-content (~28%) in the well, with 5% - 7% In-content in the InGaN barrier and in the InGaN SB buffer, to push the emission wavelength longer in the deep green spectra (520 nm - 540 nm). The optimal epitaxial growth parameters to obtain good quality InGaN SB buffer, good quality InGaN/InGaN MQW and the combination of both to achieve MQW on SB with deep green emission is the subject of current study.

6.2.2 *Optimization of the p-GaN layer*

Further optimization of the p-GaN layer will be done to improve the surface morphology and to reduce the leakage current in our LED chips. The growth temperature and the thickness of the p-GaN will be optimized to get the optimum

surface quality of the p-GaN layer and to reduce the depth, size and number of the V-pits.

6.2.3   Optimization of the technological process for blue-green LEDs

The wafer processing of the LED devices will be optimized further in terms of processing steps and choice of p- and n-contact metal alloys. A different type of n- and p-contact metal schemes, other than the n- and p-contact discussed in the processing chapter, will be investigated. The technological processing steps are shown in Figure 96.
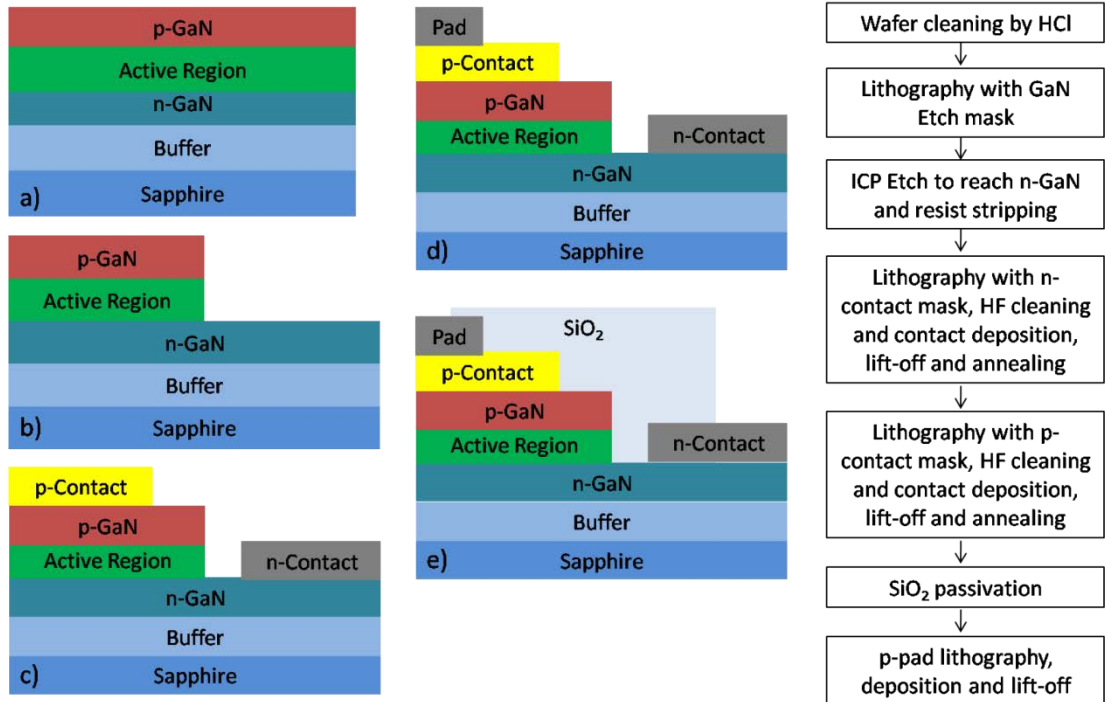
Figure 96: Planned processing steps of LED wafer with alternative p-and n-contacts.

The n-contact will be Ti/Al/Ni/Au (20 nm / 200 nm / 25 nm / 25 nm) with annealing at temperature of 850 ^{o}C for 30 s under N_2. The p-contact will be Ni/Au (10 nm / 10 nm) with annealing at temperature of 600 ^{o}C for 60 s under N_2/O_2.

Growth of InGaN MQW-based LEDs with InGaN SB buffer on 2D hexagonal boron nitride (h-BN) layer

Recently, growth of 2D materials such as h-BN has got much attention because of the potential for wafer-scale transfer onto low-cost substrates. Our group has already reported wafer scale exfoliation of MOVPE grown InGaN/GaN MQW structure grown on a 5 nm thick h-BN layer on a 2-inch sapphire substrate. My future work will be further optimizing the h-BN on sapphire and then to grow our InGaN/InGaN MQW on InGaN SB buffer with ~25% In in well and 5% - 7% In in barrier and in SB buffer, on this h-BN and then to transfer on low-cost substrate and to investigate the retention of emission properties before and after transfer.

6.3 Publications and Conference contributions

6.3.1 *Journal Publications*

1. **S. Alam**, S. Sundaram, M. Elouneg-Jamroz, X. Li, Y. El Gmili, I.C. Robin, P.L. Voss, J.-P. Salvestrini, A. Ougazzaden. "InGaN/InGaN multiple quantum well grown on InGaN/GaN semi-bulk buffer for blue to cyan emission with improved optical emission and efficiency droop", Superlattices Microstruct. 104 (2017) 291–297.

2. **S. Alam**, S. Sundaram, X. Li, M. E. Jamroz, Y. El Gmili, I. C. Robin, P. L. Voss, J.-P. Salvestrini, A. Ougazzaden, "Influence of barrier layer indium on efficiency and wavelength of InGaN multiple quantum well (MQW) with and without semi-bulk InGaN buffer for blue to green regime emission", Phys. Status Solidi A, 214 (8) (2017), 1600868.

3. **S. Alam**, S. Sundaram, H. Haas, X. Li, Y. El Gmili, M. E. Jamroz, I. C. Robin, P. L. Voss, J.-P. Salvestrini, A. Ougazzaden, "Investigation of p-contact performance

for indium rich InGaN based light emitting diodes and solar cells", Phys. Status Solidi A, 214 (4) (2017), 1600496.

4. X. Li, M.B. Jordan, T. Ayari, S. Sundaram, Y. El Gmili, **S. Alam**, M. Alam, G. Patriarche, P. L. Voss, J.-P Salvestrini, and A. Ougazzaden, "Flexible metal-semiconductor-metal device prototype on wafer-scale thick boron nitride layers grown by MOVPE", Sci. Rep. 7 (2017), 786.

5. **S. Alam**, S. Sundaram, X. Li, Y. El Gmili, M. E. Jamroz, I. C. Robin, P. L. Voss, J.-P. Salvestrini, A. Ougazzaden, "Emission wavelength red-shift by using "semi-bulk" InGaN buffer layer in InGaN/InGaN multiple-quantum-well", Superlattices Microstruct. 112 (2017), 279-286.

6.3.2 Conferences

1. **Saiful Alam**, Helge Haas, Suresh Sundaram, Xin Li, Youssef El Gmili, Miryam E. Jamroz, Ivan C. Robin , Jean-Paul Salvestrini, Paul L. Voss, and Abdallah Ougazzaden, "Investigation of p-contact performance for InGaN/InGaN LEDs for blue to green emission", EMRS Spring Meeting 2016, Lille, France.

2. **Saiful Alam**, Suresh Sundaram, Xin Li, Youssef El Gmili, Miryam E. Jamroz, Ivan C. Robin , Jean-Paul Salvestrini, Paul L. Voss, and Abdallah Ougazzaden, "Emission wavelength red-shift of InGaN/InGaN multi-quantum-well by using novel semi-bulk InGaN template", ICMOVPE 2016, San Diego, USA.

3. **Saiful Alam**, Suresh Sundaram , Miryam E. Jamroz, Xin Li, Ivan C. Robin, Jean Paul Salvestrini, Paul L. Voss, and Abdallah Ougazzaden, "Influence of indium in barriers of multi quantum well (MQW) with novel InGaN pre-Layer emitting in blue to green regime", IWN 2016, Orlando, USA.

4. Suresh Sundaram, Taha Ayari, Xin Li, **Saiful Alam**, Youssef El Gmili, Paul L. Voss, Jean Paul Salvestrini and Abdallah Ougazzaden, "Realization of GaN, InGaN/GaN MQW and semi-Bulk based PIN structures on the ultrathin 2D layered h-BN for Simple mechanical lift-off", IWN 2016, Orlando, USA.

5. **Saiful Alam**, Suresh Sundaram, Xin Li, Youssef El Gmili, Miryam E. Jamroz, Ivan C. Robin, Jean-Paul Salvestrini, Paul L. Voss, and Abdallah Ougazzaden, "Realization of green light-emitting diode by using novel InGaN semi-bulk buffer technique", Photoptics 2017, Porto, Portugal.

6. **Saiful Alam**, Suresh Sundaram, Xin Li, Youssef El Gmili, Miryam E. Jamroz, Ivan C. Robin, Jean-Paul Salvestrini, Paul L. Voss, and Abdallah Ougazzaden, "Study of photoluminescence mechanism of InGaN multi-quantum-well based LEDs grown on novel high quality semi-bulk InGaN buffer for blue to cyan emission", EMRS Spring Meeting 2017, Strasbourg, France.

7. Suresh Sundaram, Xin Li, Taha Ayari, **Saiful Alam**, Youssef El Gmili, Gilles Patriarche, Paul L. Voss, Jean Paul Salvestrini, Abdallah Ougazzaden, "Wafer scale MOVPE growth of AlGaN/GaN HEMT structures on 2D h-BN buffered sapphire templates", ICNS 2017, Strasbourg, France.

8. Xin Li, Matthew B. Jordan, Taha Ayari, Suresh Sundaram, Youssef El Gmili, **Saiful Alam**, Muhbub Alam, Gilles Patriarche, Paul L. Voss, Jean-Paul Salvestrini, and Abdallah Ougazzaden, "Deep UV photodetector prototype on flexible wafer-scale thick boron nitride layers grown by MOVPE", ICNS 2017, Strasbourg, France.

6.3.3 Award

1. Best poster award, Symposium L, EMRS Spring Meeting 2016, Lille, France.

REFERENCES

[1]   E. F. Schubert, Light-Emitting Diodes, Cambridge University Press, 2006.

[2]   R. D. Dupuis, M.R. Krames, History, development, and applications of high-brightness visible light-emitting diodes, J. Light. Technol. 26 (2008) 1154–1171.

[3]   X. Guo, Q.-L. Liu, C. Li, B. Liu, J. Dong, G.-D. Shen, Phosphor-free white light-emitting diodes, Chinese Phys. B. 24 (2015) 68505.

[4]   M. Auf Der Maur, A. Pecchia, G. Penazzi, W. Rodrigues, A. Di Carlo, Efficiency Drop in Green InGaN/GaN Light Emitting Diodes: The Role of Random Alloy Fluctuations, Phys. Rev. Lett. 116 (2016) 1–5.

[5]   Y. Narukawa, M. Ichikawa, D. Sanga, M. Sano, T. Mukai, White light emitting diodes with super-high luminous efficacy, J. Phys. D. Appl. Phys. 43 (2010) 354002.

[6]   T. Wunderer, M. Feneberg, F. Lipski, J. Wang, R. a. R. Leute, S. Schwaiger, K. Thonke, A. Chuvilin, U. Kaiser, S. Metzner, F. Bertram, J. Christen, G. J. Beirne, M. Jetter, P. Michler, L. Schade, C. Vierheilig, U. T. Schwarz, A. D. Dräger, A. Hangleiter, F. Scholz, Three-dimensional GaN for semipolar light emitters, Phys. Status Solidi. 248 (2011) 549–560.

[7]   F. K. Yam, Z. Hassan, InGaN: An overview of the growth kinetics, physical properties and emission mechanisms, Superlattices Microstruct. 43 (2008) 1–23.

[8] C. Tran, R.. Karlicek, M. Schurman, A. Osinsky, V. Merai, Y. Li, I. Eliashevich, M.. Brown, J. Nering, I. Ferguson, R. Stall, Phase separation in InGaN/GaN multiple quantum wells and its relation to brightness of blue and green LEDs, J. Cryst. Growth. 195 (1998) 397–400.

[9] J. Piprek, Efficiency droop in nitride-based light-emitting diodes, Phys. Status Solidi. 207 (2010) 2217–2225.

[10] F. Scholz, T. Wunderer, M. Feneberg, K. Thonke, A. Chuvilin, U. Kaiser, S. Metzner, F. Bertram, J. Christen, GaInN-based LED structures on selectively grown semi-polar crystal facets, Phys. Status Solidi. 207 (2010) 1407–1413.

[11] B. Hahn, Closing the Green Efficiency Gap ... Status and recent approaches, DoE workshop, Raleigh (2016) 1–16.

[12] D. Feezell, S. Nakamura, Invention, development, and status of the blue light-emitting diode, the enabler of solid-state lighting, Comptes Rendus Phys. 1 (2018) 1–21.

[13] A. Bergh, G. Craford, A. Duggal, R. Haitz, The promise and challenge of solid-state lighting, Phys. Today. 54 (2001) 42–47.

[14] US. D. of Energy, Solid-State Lighting R&D Plan, Electron. Publ. (2016) 1–208.

[15] C. J. Humphreys, Solid-State Lighting, MRS Bull. 33 (2008) 459–470.

[16] I. C. Robin, P. Ferret, A. Dussaigne, C. Bougerol, D. Salomon, X. J. Chen, M. Charles, P. Tchoulfian, A. Gasse, A. Lagrange, M. Consonni, H. Bono, F. Levy, Y. Desieres, A. Aitmani, S. Makram-Matta, E. Bialic, P. Gorrochategui,

L. Mendizabal, Complete solid state lighting (SSL) line at CEA LETI, 9190 (2014) 91900I.

[17] R. Haitz, J. Y. Tsao, Solid-state lighting Why it will succeed , and why it won ' t be overtaken, Light. Technol. (2011) 26–30.

[18] H. Morkoç, Nitride Semiconductor Devices: Fundamentals and Applications, Wiley-VCH, 2013.

[19] S. Nakamura, M. R. Krames, History of Gallium – Nitride-Based Light-Emitting Diodes for Illumination, Proceedings of the IEEE 101 (2013) 1–10.

[20] H. P. Maruska, W. C. Rhines, A modern perspective on the history of semiconductor nitride blue light sources, Solid. State. Electron. 111 (2015) 32–41.

[21] J. Cho, J. H. Park, J. K. Kim, E. F. Schubert, White light-emitting diodes: History, progress, and future, Laser Photon. Rev. 1600147 (2017) 1600147.

[22] H. Morkoç, Handbook of Nitride Semiconductors and Devices, Wiley-VCH, 2008.

[23] H. Amano, M. Kito, K. Hiramatsu, I. Akasaki, P-Type Conduction in Mg-Doped GaN Treated with Low-Energy Electron Beam Irradiation (LEEBI), Jpn. J. Appl. Phys., 28(12) (1989) L2112-L2114.

[24] H. Amano, T. Asahi and I. Akasaki, Stimulated Emission Near Ultraviolet at Room Temperature from a GaN Film Grown on Sapphire by MOVPE Using an AlN Buffer Layer, Jpn. J. Appl. Phys., 29(2) (1990) L205-L206.

[25]   S. Nakamura, T. Mukai, and M. Senoh, High-Power GaN P-N Junction Blue-Light-Emitting Diodes, Jpn. J. Appl. Phys., 30(12A) (1991) L1998-L2001.

[26]   S. Nakamura, M. Senoh, and T. Mukai, Highly P-Typed Mg-Doped GaN Films Grown with GaN Buffer Layers, Jpn. J. Appl. Phys., 30(10A) (1991) L1708-L1711.

[27]   S. Nakamura, T. Mukai, M. Senoh, and N. Iwasa, Thermal Annealing Effects on P-Type Mg-Doped GaN Films, Jpn. J. Appl. Phys., 31 (1992) L139-L142.

[28]   K. Pantzas, Growth and Characterization of High-Quality, Thick InGaN Epilayers for High-Efficiency , Low-Cost Solar Cells, Ph.D. thesis, Georgia Institute of Technology, (2015).

[29]   J.W. Orton, C.T. Foxon, Group III nitride semiconductors for short wavelength light-emitting devices, Rep. Prog. Phys. 61 (1998) 1–75.

[30]   K. Ohkawa, T. Watanabe, M. Sakamoto, A. Hirako, M. Deura, 740-nm emission from InGaN-based LEDs on c -plane sapphire substrates by MOVPE, J. Cryst. Growth. 343 (2012) 13–16.

[31]   S. Nakamura, III-V Nitride Based Light-Emithng Devices, Solid State Communications, 102 (2-3) (1997), 237-248.

[32]   M. R. Krames, Status and Future Prospects for Visible-Spectrum Light-Emitting Diodes, SID Digest 1 (2016) 39–41.

[33]   U. K. Mishra, Y. Wu, B. P. Keller, S. Keller, S. P. Denbaars, GaN Microwave Electronics, 46 (1998) 756–761.

[34] S. T. Sheppard, K. Doverspike, W. L. Pribble, S. T. Allen, J. W. Palmour, L. T. Kehias, T. J. Jenkins, High-Power Microwave GaN / AlGaN HEMT ' s on Semi-Insulating Silicon Carbide Substrates, 20 (1999) 161–163.

[35] B. M. Green, S. Member, K. K. Chu, E. M. Chumbes, S. Member, J. A. Smart, J. R. Shealy, L. F. Eastman, L. Fellow, The Effect of Surface Passivation on the Microwave Characteristics of Undoped AlGaN / GaN HEMT 's, 21 (2000) 268–270.

[36] R. Vetury, N. Q. Zhang, S. Keller, U. K. Mishra, The Impact of Surface States on the DC and RF Characteristics of AlGaN / GaN HFETs, 48 (2001) 560–566.

[37] Y. Wu, D. Kapolnek, J. P. Ibbetson, P. Parikh, B. P. Keller, U. K. Mishra, Very-High Power Density AlGaN / GaN HEMTs, 48 (2001) 586–590.

[38] J. Kuzmík, Power Electronics on InAlN /(In) GaN : Prospect for a Record Performance, 22 (2001) 510–512.

[39] Y. El Gmili, G. Orsal, K. Pantzas, T. Moudakir, S. Sundaram, G. Patriarche, J. Hester, A. Ahaitouf, J. P. Salvestrini, A. Ougazzaden, Multilayered InGaN/GaN structure vs. single InGaN layer for solar cell applications: A comparative study, Acta Mater. 61 (2013) 6587–6596.

[40] Y. Halfaya, C. Bishop, A. Soltani, S. Sundaram, V. Aubry, P. L. Voss, J. Salvestrini, A. Ougazzaden, NO 2 and NH 3 Exhaust Gas Sensors for Automotive Antipollution Systems, Sensors 16 (3) (2016) 273.

[41] E. Munoz, E. Monroy, J. L. Pau, F. Calle, F. Omnes, and P. Gibart, III nitrides and UV detection, J. Phys.: Condens. Matter 13 (2001) 7115–7137.

[42] T. Mukai, M.Yamada, and S. Nakamura, Characteristics of InGaN-Based UV/Blue/ Green/Amber/Red Light-Emitting Diodes, J. Appl. Phys. 38 (1999) 3976–3981.

[43] E. Monroy, F. Omnes, and F. Calle, Wide-bandgap semiconductor ultraviolet photodetectors, Semicond. Sci. Technol. 18 (2003) R33–R51.

[44] X. Li, Lasers A Cavite Vertical Emettant Par La Surface Dans L ' Ultraviolet Profond A Base Des Materiaux BAlGaN, Ph.D. thesis, University of Lorraine, France, December (2015).

[45] S. Alam, Fabrication and Characterization of InGaN / GaN Based Semipolar Green Light Emitting Diodes, Master's Thesis, University of Ulm, December (2013).

[46] F. Scholz, Compound Semiconductors : Physics, Technology, and Device Concepts, Pan Stanford Publishing, 2018.

[47] I. Vurgaftman, J. R. Meyer, L. R. Ram-Mohan, Band parameters for III-V compound semiconductors and their alloys, J. Appl. Phys. 89 (2001) 5815–5875.

[48] M. A. Moram, M. E. Vickers, X-ray diffraction of III-nitrides, Reports Prog. Phys. 72 (2009) 36502.

[49] K. Pantzas, Elaboration Par MOVPE Et Caractérisation Des Matériaux (B) Ingan Pour Les Cellules Solaires De 3ème Génération, Ph.D. thesis, University of Lorraine, France, September (2013).

[50] S. Khromov, The Effect of Mg Doping on Optical and Structural Properties of

GaN, Ph.D. thesis, Linkoping University, Sweden, (2012).

[51]   H. Amano, Development of GaN-based blue LEDs and metalorganic vapor phase epitaxy of GaN and related materials, Prog. Cryst. Growth Charact. Mater. 62 (2016) 126–135.

[52]   F. Bernardini, V. Fiorentini, Spontaneous vs. piezoelectric polarization in III-V nitrides: conceptual aspects and practical consequences, Phys. Status Solidi B 216 (1) (1999) 391–398.

[53]   F. Bernardini, V. Fiorentini, D. Vanderbilt, Spontaneous polarization and piezoelectric constants of III-V nitrides, Phys. Rev. B 56 (16) (1997) 4.

[54]   M. Feneberg, K. Thonke, Polarization fields of III-nitrides grown in different crystal orientations, J. Phys. Condens. Matter. 19 (2007) 403201.

[55]   P. P. Paskov, T. Paskova, P. O. Holtz, B. Monemar, Internal Structure of Free Excitons in GaN, 470 (2001) 467–470.

[56]   J. Wu, W. Walukiewicz, K. M. Yu, J. W. Ager, E. E. Haller, H. Lu, W. J. Schaff, J. Wu, Small band gap bowing in In $_{1-x}$Ga$_x$N alloys, Appl. Phys. Lett. 80 (25) (2002) 4741-4743.

[57]   B. Monemar, P.P. Paskov, G. Pozina, C. Hemmingsson, J.P. Bergman, H. Amano, I. Akasaki, S. Figge, D. Hommel, T. Paskova, A. Usui, Phys. Status Solidi C 7 (2010) 1850–1852.

[58]   C. Brosseau, M. Perrin, C. Silva, R. Leonelli, Carrier recombination dynamics in In x Ga 1 − x N Õ GaN multiple quantum wells, Phys. Rev. B 82 (2010) 085305.

[59] A. F. Wright, K. Leung, M. Van Schilfgaarde, A.F. Wright, K. Leung, Effects of biaxial strain and chemical ordering on the band gap of InGaN Effects of biaxial strain and chemical ordering on the band gap of InGaN, Appl. Phys. Lett. 78 (2001) 189.

[60] U.T. Schwarz, and M. Kneissl, Nitride emitters go nonpolar, Phys. Status Solidi RRL 1 (3) (2007) A44–A46.

[61] G.A. Garrett, H. Shen, M. Wraback, A. Tyagi, M.C. Schmidt, J.S. Speck, S.P. Denbaars, S. Nakamaura, Phys. Status Solidi C 6 (S2) (2009) S800–S803.

[62] Sk. S. Rahman, Optimization of Optoelectronic Device Structures on Freestanding Galliumnitride Templates, Master's Thesis, University of Ulm, Germany, (2013).

[63] J. Jang, C. Lee, S. Park, T. Seong, I.T. Ferguson, Low-Resistance and Thermally Stable Pd / Ru Ohmic Contacts to p-Type GaN, Journal of Electron. Mat., 31 (9) 2002 903–906.

[64] M. J. Jou, Luminescence of an InGaN / GaN multiple quantum well light-emitting diode, Solid State Electron.44 (2000) 1055–1058.

[65] J.O. Song, J.-S. Ha, T.-Y. Seong, Ohmic-Contact Technology for GaN-Based Light-Emitting Diodes: Role of P-Type Contact, IEEE Trans. Electron Devices. 57 (2010) 42–59.

[66] T. Mukai, M. Yamada, and S. Nakamura, Characteristics of InGaN-Based UV / Blue / Green / Amber / Red Light-Emitting Diodes, Jpn. J. Appl. Phys. (38) (1999) 3976–3981.

[67] Y.C. Shen, G.O. Mueller, S. Watanabe, N.F. Gardner, A. Munkholm, M.R. Krames, Auger recombination in InGaN measured by photoluminescence, Appl. Phys. Lett. 91 (2007) 141101.

[68] L. Wang, X. Meng, J. Wang, Z. Hao, Y. Luo, C. Sun, Y. Han, B. Xiong, J. Wang, H. Li, Understanding different efficiency droop behaviors in InGaN-based near-UV, blue and green light-emitting diodes through differential carrier lifetime measurements, Arxiv. (2016) 1611.07972.

[69] A. I. Alhassan, R. M. Farrell, B. Saifaddin, A. Mughal, F. Wu. S. P. Denbaars, S. Nakamura, and J. S. Speck, High luminous efficacy green light-emitting diodes with AlGaN cap layer, Opt. Express 24 (16) (2016) 17868–17873.

[70] P. Pust, P. J. Schmidt, W. Schnick, A revolution in lighting, Nat. Publ. Gr. 14 (2015) 454–458.

[71] Y. Narukawa, J. Narita, T. Sakamoto, K. Deguchi, T. Yamada, T. Mukai, Ultra-High Efficiency White Light Emitting Diodes, Jpn. J. Appl. Phys. 45 (2006) L1084–L1086.

[72] K. A. Bulashevich, A. V. Kulik, S. Y. Karpov, Optimal ways of colour mixing for high-quality white-light LED sources, Phys. Status Solidi A 212 (2015) 914–919.

[73] D. Schiavon, M. Binder, M. Peter, B. Galler, P. Drechsel, F. Scholz, Wavelength-dependent determination of the recombination rate coefficients in single-quantum-well GaInN/GaN light emitting diodes, Phys. Status Solidi B 250 (2013) 283–290.

[74] M. Peter, A. Laubsch, W. Bergbauer, T. Meyer, M. Sabathil, J. Baur, B. Hahn, New developments in green LEDs, Phys. Status Solidi A 206 (2009) 1125–1129.

[75] Z. Deng, Y. Jiang, W. Wang, L. Cheng, W. Li, W. Lu, H. Jia, W. Liu, J. Zhou, H. Chen, Indium segregation measured in InGaN quantum well layer., Sci. Rep. 4 (2014) 6734.

[76] S. Gautier, C. Sartel, S. Ould-Saad, J. Martin, A. Sirenko, A. Ougazzaden, GaN materials growth by MOVPE in a new-design reactor using DMHy and NH_3, J. Cryst. Growth. 298 (2007) 428–432.

[77] D. C. Look, G. C. Farlow, P. J. Drevinsky, D. F. Bliss, J. R. Sizelove, On the nitrogen vacancy in GaN, Appl. Phys. Lett. 83 (2003) 3525–3527.

[78] P. Gibart, Metal organic vapour phase epitaxy of GaN and lateral overgrowth, Reports Prog. Phys. 67 (2004) 667–715.

[79] Y. El Gmili, G. Orsal, K. Pantzas, a Ahaitouf, T. Moudakir, S. Gautier, G. Patriarche, D. Troadec, J.P. Salvestrini, a Ougazzaden, G. Tech-cnrs, R. Marconi, G.T. Lorraine, Characteristics of the surface microstructures in thick InGaN layers on GaN, Opt. mater. express 3 (8) (2013) 1111–1118.

[80] Atlas User's Manual, Silvaco Inc. (2014) 567–1000.

[81] J. Dalfors, J. P. Bergman, P. O. Holtz, B. E. Sernelius, B. Monemar, H. Amano, I. Akasaki, Optical properties of doped InGaN/GaN multiquantum-well structures, Appl. Phys. Lett. 74 (1999) 3299–3301.

[82] Y. Yang, Y. Zeng, Enhancement of hole injection with Mg-Si-codoped barriers

in InGaN-based light-emitting diodes, Opt. Commun. 326 (2014) 121–125.

[83]   N. G. Young, R. M. Farrell, S. Oh, M. Cantore, F. Wu, S. Nakamura, S. P. DenBaars, C. Weisbuch, J. S. Speck, Polarization field screening in thick (0001) InGaN/GaN single quantum well light-emitting diodes, Appl. Phys. Lett. 108 (2016) 1–6.

[84]   J. Piprek, F. Römer, B. Witzigmann, On the uncertainty of the Auger recombination coefficient extracted from InGaN / GaN light-emitting diode efficiency droop measurements, Appl. Phys. Lett. 106 (2015) 101101–4.

[85]   M. Meneghini, N. Trivellin, G. Meneghesso, E. Zanoni, U. Zehnder, B. Hahn, A combined electro-optical method for the determination of the recombination parameters in InGaN-based light-emitting diodes, J. Appl. Phys. 106 (2009) 114509.

[86]   A. David, M. J. Grundmann, Droop in InGaN light-emitting diodes: A differential carrier lifetime analysis, Appl. Phys. Lett. 97 (2010) 033501.

[87]   I. Vurgaftman, J. R. Meyer, Band parameters for nitrogen-containing semiconductors, J. Appl. Phys. 94 (6) (2003) 3675-3696.

[88]   J. Bai, T. Wang, S. Sakai, Influence of the quantum-well thickness on the radiative recombination of InGaN/GaN quantum well structures, J. Appl. Phys. 88 (2000) 4729.

[89]   P. Kumar, M.S.B.M. Saheed, Z.A. Burhanudin, Performance Comparison of One & Two Quantum Wells Light Emitting Diodes Simulated With COMSOL Multiphysics, Proceedings of the 6th International Conference on Intelligent

and Advanced Systems 3 (2016) 1-6.

[90]   S. M. Thahab, H. A. Hassan, Z. Hassan, Effect of varying quantum well thickness on the performance of InGaN/GaN single quantum well laser diode, AIP Conf. Proc. 1017 (2008) 149–153.

[91]   Z. Lin, H. Wang, Y. Lin, M. Yang, Influence of In content in InGaN barriers on crystalline quality and carrier transport of GaN-based light-emitting diodes, J. Phys. D. Appl. Phys. 49 (2016) 115112.

[92]   Y. Yang, Y. Zeng, Alternating InGaN barriers with GaN barriers for enhancing optical performance in InGaN light-emitting diodes, J. Appl. Phys. 117 (2015). 035705.

[93]   F. Römer, B. Witzigmann, Effect of Auger recombination and leakage on the droop in InGaN / GaN quantum well LEDs, Opt. Express 22 (2014) 1440–1452.

[94]   D. Watson-parris, Carrier Localization in InGaN / GaN Quantum Wells, Ph.D. thesis, The University of Manchester, UK, (2011).

[95]   K. Pantzas, Y. El Gmili, J. Dickerson, S. Gautier, L. Largeau, O. Mauguin, G. Patriarche, S. Suresh, T. Moudakir, C. Bishop, a. Ahaitouf, T. Rivera, C. Tanguy, P.L. Voss, a. Ougazzaden, Semibulk InGaN: A novel approach for thick, single phase, epitaxial InGaN layers grown by MOVPE, J. Cryst. Growth. 370 (2013) 57–62.

[96]   J. Dickerson, Heterostructure Polarization Charge Engineering For Improved And Novel III-V Semiconductor Devices, Ph.D. thesis, Georgia Institute of

Technology, USA, (2014).

[97] W. C. Lai, Y. S. Huang, Y. W. Yen, J. K. Sheu, T. H. Hsueh, C. H. Kuo, S. J. Chang, The CL emission observation of the InGaN/GaN MQWs V shaped pits with different superlattices underlayers, Phys. Status Solidi C 5 (2008) 1639–1641.

[98] M. J. Davies, F.C.P. Massabuau, P. Dawson, R. A. Oliver, M. J. Kappers, C. J. Humphreys, Effects of an InGaN prelayer on the properties of InGaN/GaN quantum well structures, Phys. Status Solidi C 11 (2014) 710–713.

[99] D. M. Van Den Broeck, D. Bharrat, A. M. Hosalli, N. A. El-Masry, S.M. Bedair, Strain-balanced InGaN/GaN multiple quantum wells, Appl. Phys. Lett. 105 (2014) 31107.

[100] M. J. Davies, P. Dawson, F.C.P. Massabuau, R. A. Oliver, M. J. Kappers, C. J. Humphreys, The effects of Si-doped prelayers on the optical properties of InGaN/GaN single quantum well structures, Appl. Phys. Lett. 105 (2014) 092106.

[101] D. M. Van Den Broeck, D. Bharrat, Z. Liu, N.A. El-Masry, S. M. Bedair, Growth and Characterization of High-Quality, Relaxed In $_y$ Ga$_{1-y}$ N Templates for Optoelectronic Applications, J. Electron. Mater. 44 (2015) 4161–4166.

[102] Y. Xia, W. Hou, L. Zhao, M. Zhu, T. Detchprohm, C. Wetzel, Boosting Green GaInN / GaN Light-Emitting Diode Performance by a GaInN Underlying Layer, IEEE Trans. on Electron Devices, 57 (10) 201057 (2010) 2639–2643.

[103] M. J. Davies, P. Dawson, F. C. Massabuau, A. Le Fol, R. A. Oliver, M. J.

Kappers, C. J. Humphreys, A study of the inclusion of prelayers in InGaN / GaN single- and multiple-quantum-well structures, Phys. Status Solidi B 252 (2015) 866–872.

[104] G. Orsal, Y. El Gmili, N. Fressengeas, J. Streque, R. Djerboub, T. Moudakir, S. Sundaram, A. Ougazzaden, J. P. Salvestrini, Bandgap energy bowing parameter of strained and relaxed InGaN layers, Opt. Mater. Express. 4 (2014) 1030.

[105] C. Bazioti, E. Papadomanolaki, T. Kehagias, T. Walther, J. Smalc-Koziorowska, E. Pavlidou, P. Komninou, T. Karakostas, E. Iliopoulos, G. P. Dimitrakopulos, Defects, strain relaxation, and compositional grading in high indium content InGaN epilayers grown by molecular beam epitaxy, J. Appl. Phys. 118 (2015) 115301.

[106] Y. Kuo, J. Chang, M. Tsai, S. Yen, Y. Kuo, J. Chang, M. Tsai, S. Yen, Advantages of blue InGaN multiple-quantum well light-emitting diodes with InGaN barriers, 95 (2009) 011116.

[107] N. Nanhui, W. Huaibing, L. Jianping, L. Naixin, X. Yanhui, H. Jun, D. Jun, S. Guangdi, Improved quality of InGaN/GaN multiple quantum wells by a strain relief layer, J. Cryst. Growth. 286 (2006) 209–212.

[108] J.-H. Yang, L. Shi, L.-W. Wang, S.-H. Wei, Non-Radiative Carrier Recombination Enhanced by Two-Level Process: A First-Principles Study, Sci. Rep. 6 (2016) 21712.

[109] S.W. Chen, H. Li, C.J. Chang, T.C. Lu, Effects of nanoscale V-shaped pits on GaN-based light emitting diodes, Materials 10 (2017) 1–11.

[110] Y.-L. Lai, C.-P. Liu, Y.-H. Lin, T.-H. Hsueh, R.-M. Lin, D.-Y. Lyu, Z.-X. Peng, T.-Y. Lin, Origins of efficient green light emission in phase-separated InGaN quantum wells, Nanotechnology. 17 (2006) 3734.

[111] N. Ben-Sedrine, T. C. Esteves, J. Rodrigues, L. Rino, M. R. Correia, M. C. Sequeira, A. J. Neves, E. Alves, M. Bockowski, P. R. Edwards, K. P. O'Donnell, K. Lorenz, T. Monteiro, Photoluminescence studies of a perceived white light emission from a monolithic InGaN/GaN quantum well structure., Sci. Rep. 5 (2015) 13739.

[112] C. Hums, T. Finger, T. Hempel, J. Christen, A. Dadgar, A. Hoffmann, A. Krost, Fabry-Perot effects in InGaNGaN heterostructures on Si-substrate, J. Appl. Phys. 101 (2007) 1–5.

[113] S. Alam, S. Sundaram, M. Elouneg-Jamroz, X. Li, Y. El Gmili, I.C. Robin, P.L. Voss, J.-P. Salvestrini, A. Ougazzaden, InGaN/InGaN multiple-quantum-well grown on InGaN/GaN semi-bulk buffer for blue to cyan emission with improved optical emission and efficiency droop, Superlattices Microstruct. 104 (2017) 291–297.

[114] N. Gao, K. Huang, J. Li, S. Li, X. Yang, J. Kang, Surface-plasmon-enhanced deep-UV light emitting diodes based on AlGaN multi-quantum wells, Sci. Rep. 2 (816) (2012) 1-6.

[115] G. H. Gu, D. H. Jang, K. B. Nam, C. G. Park, Composition Fluctuation of In and Well-Width Fluctuation in InGaN / GaN Multiple Quantum Wells in Light-Emitting Diode Devices, Microsc.Microanal. 19 (2013) 99–104.

[116] I. L. Lu, Y.R. Wu, J. Singh, A study of the role of dislocation density, indium

composition on the radiative efficiency in InGaN/GaN polar and nonpolar light-emitting diodes using drift-diffusion coupled with a Monte Carlo method, J. Appl. Phys. 108 (2010) 124508.

[117] M. Singh, J. Singh, Design of high electron mobility devices with composite nitride channels, J. Appl. Phys. 94 (2003) 2498–2506.

[118] J.-H. Ryou, W. Lee, J. Limb, D. Yoo, J.P. Liu, R. D. Dupuis, Z. H. Wu, A. M. Fischer, F. A. Ponce, Control of quantum-confined Stark effect in InGaN⁄GaN multiple quantum well active region by p-type layer for III-nitride-based visible light emitting diodes, Appl. Phys. Lett. 92 (2008) 101113.

[119] S. J. Pearton, J. C. Zolper, R. J. Shul, F. Ren, GaN: Processing, defects, and devices, J. Appl. Phys. 86 (1999) 1–78.

[120] X.-L. Hu, L. Liu, H. Wang, X.-C. Zhang, Effects of pre-annealed ITO film on the electrical characteristics of high-reflectance Ni/Ag/Ni/Au contacts to p-type GaN, Appl. Surf. Sci. 357 (2015) 1703–1707.

[121] S. Belahsene, G. Patriarche, D. Troadec, S. Sundaram, A. Ougazzaden, A. Martinez, A. Ramdane, Microstructural and electrical investigation of Pd/Au ohmic contact on p-GaN, J. Vac. Sci. Technol. B, Nanotechnol. Microelectron. Mater. Process. Meas. Phenom. 33 (2015) 10603.

[122] J. Buckeridge, C.R.A. Catlow, D.O. Scanlon, T.W. Keal, P. Sherwood, M. Miskufova, A. Walsh, S.M. Woodley, A.A. Sokol, Determination of the nitrogen vacancy as a shallow compensating center in GaN doped with divalent metals, Phys. Rev. Lett. 114 (2015) 1–5.

[123] B.P. Gunning, C.A.M. Fabien, J.J. Merola, E.A. Clinton, W.A. Doolittle, S. Wang, A.M. Fischer, F.A. Ponce, Comprehensive study of the electronic and optical behavior of highly degenerate p-type Mg-doped GaN and AlGaN, J. Appl. Phys. 117 (2015).

[124] Y. Jiao, A. Hellman, Y. Fang, S. Gao, M. Käll, Schottky barrier formation and band bending revealed by first- principles calculations, Sci. Rep. 5 (2015) 11374.

[125] J. Yang, D.-G. Zhao, D.-S. Jiang, P. Chen, Z.-S. Liu, J.-J. Zhu, L.-C. Le, X.-J. Li, X.-G. He, L.-Q. Zhang, H. Yang, Different variation behaviors of resistivity for high-temperature-grown and low-temperature-grown p-GaN films, Chinese Phys. B. 25 (2016) 27102.

[126] Q. Z. Liu, S. S. Lau, A Review of The Metal-GaN Contact Technology, Solid-state Electron. 42 (1998) 677–691.

[127] J. Wang, Y. Gao, S. Alam, F. Scholz, Mg doping of 3D semipolar InGaN/GaN-based light emitting diodes, Phys. Status Solidi A 211 (2014) 2645–2649.

[128] J. K. Kim, J.-L. Lee, J. W. Lee, H. Eoi Shin, Y. Jo Park, T. Kim, Low resistance Pd/Au ohmic contacts to p-type GaN using surface treatment, Appl. Phys. Lett. 73 (1998) 2953.

[129] J. W. Bae, T. Hossain, I. Adesida, K.H. Bogart, D. Koleske, A. A. Allerman, J. H. Jang, Low resistance ohmic contact to p-type GaN using Pd∕Ir∕Au multilayer scheme, J. Vac. Sci. Technol. B 23 (2005) 1072.

[130] H. K. Cho, T. Hossain, J. W. Bae, I. Adesida, Characterization of Pd/Ni/Au

ohmic contacts on p-GaN, Solid. State. Electron. 49 (2005) 774–778.

[131] W. Gu, T. Xu, J. Zhang, Solid-State Electronics Improved ohmic contact of Ga-Doped ZnO to p-GaN by using copper sulfide intermediate layers, Solid State Electron. 89 (2013) 76–80.

[132] X.-L. Hu, H. Wang, X.-C. Zhang, Fabrication and characterization of GaN-based light-emitting diodes without pre-activation of p-type GaN, Nanoscale Res. Lett. 10 (2015) 1-5.

[133] J.-S. Park, J. Han, T.-Y. Seong, Formation of low resistance Ti/Al-based ohmic contacts on (11–22) semipolar n-type GaN, J. Alloys Compd. 652 (2015) 167–171.

[134] Y.Y. Choi, S. Kim, M. Oh, H. Kim, T.Y. Seong, Investigation of Fermi level pinning at semipolar (11-22) p-type GaN surfaces, Superlattices Microstruct. 77 (2015) 76–81.

[135] G. Greco, P. Prystawko, M. Leszczyski, R. Lo Nigro, V. Raineri, F. Roccaforte, Electro-structural evolution and Schottky barrier height in annealed Au/Ni contacts onto p-GaN, J. Appl. Phys. 110 (2011) 123703.

[136] Y. Park, K. Ahn, H. Kim, Carrier Transport Mechanism of Ni / Ag / Pt Contacts to p-Type GaN, IEEE Trans. On Electron Devices 59 (2012) 680–684.

[137] S. Alam, S. Sundaram, H. Haas, X. Li, Y. El Gmili, M.E. Jamroz, I.C. Robin, P.L. Voss, J.-P. Salvestrini, A. Ougazzaden, Investigation of p-contact performance for indium rich InGaN based light emitting diodes and solar cells,

Phys. Status Solidi A 214 (4) (2017) 1600496.

[138] W. Schockley, Research And Investigation of Inverse Epitaxial UHF Power Triansistors,Technical Documrnentary Report No. AL TDR 64-207, AF Avionics Laboratory, Ohio, USA, September, (1964).

[139] H.H. Berger, Models For Contacts To Planar Devices, Solid-State Electron.15 (1972) 145–158.

[140] G.K. Reeves, and H.B. Harrison, Obtaining the specific contact resistance from transmission line model measurements, IEEE Electron Device Lett. 3(5) (1982) 111–113.

[141] M. Arif, Investigation of new approaches for the realization of InGaN based solar cells PhD thesis, University of Lorraine, France, (2017).

[142] J. Rechid, K. Heime, Concentric ring contacts used for the determination of contact resistances, Solid-State Electron. 44 (2000) 451–455.

[143] Y.-J. Cha, G.J. Lee, Y.L. Lee, S.K. Oh, J.S. Kwak, Temperature-dependent contact resistivity of radio frequency superimposed direct current sputtered indium tin oxide ohmic contact to p-type gallium nitride, Thin Solid Films. 591 (2015) 182–185.

[144] R.T. Tung, The physics and chemistry of the Schottky barrier height, Appl. Phys. Rev. 1 (2014) 011304.

[145] J.S. Kwak, O.H. Nam, Y. Park, Temperature-dependent contact resistivity of the nonalloyed ohmic contacts to p-GaN, J. Appl. Phys. 95 (2004) 5917–5919.

[146] L.L. Wu, D.G. Zhao, D.S. Jiang, P. Chen, L.C. Le, L. Li, Z.S. Liu, S.M. Zhang, J.J. Zhu, H. Wang, B.S. Zhang, H. Yang, Effects of thin heavily Mg-doped GaN capping layer on ohmic contact formation of p-type GaN, Semicond. Sci. Technol. 28 (2013) 105020.

[147] A. Hangleiter, F. Hitzel, C. Netzel, D. Fuhrmann, U. Rossow, G. Ade, P. Hinze, Suppression of nonradiative recombination by V-shaped pits in GaInN/GaN quantum wells produces a large increase in the light emission efficiency, Phys. Rev. Lett. 95 (2005) 1–4.

[148] M. B. Jordan, Growth Optimization And Process Development Of Indium Gallium Nitride / Gallium Nitride Solar Cells, PhD Thesis, Georgia Tech, USA, (2017).

[149] J. Wang, T. Meisch, D. Heinz, R. Zeller, F. Scholz, Internal quantum efficiency and carrier injection efficiency of c -plane, $\{10\bar{1}1\}$ and $\{11\bar{2}2\}$ InGaN/GaN-based light-emitting diodes, Phys. Status Solidi. 253 (2016) 174–179.

[150] B. P. Yonkee, R. M. Farrell, J. T. Leonard, S. P. DenBaars, J. S. Speck, S. Nakamura, Demonstration of low resistance ohmic contacts to p-type $(20\bar{2}\bar{1})$ GaN, Semicond. Sci. Technol. 30 (2015) 75007.

[151] X.-J. Li, D.-G. Zhao, D.-S. Jiang, P. Chen, J.-J. Zhu, Z.-S. Liu, L.-C. Le, J. Yang, X.-G. He, L.-Q. Zhang, J.-P. Liu, S.-M. Zhang, H. Yang, Influence of a deep-level-defect band formed in a heavily Mg-doped GaN contact layer on the Ni/Au contact to p-GaN, Chinese Phys. B. 24 (2015) 96804.

APPENDIX

A1. Calculation of relaxation from XRD RSM

Let, lattice parameters for,

Substrate : a_s, c_s

Fully relaxed layer : a_0, c_0

Layer on the substrate : a, c

Values obtained from RSM using "semi automatic peak search" in X'pert Epitaxy software are,

Q_x and Q_z of the layer; Q_{xs} and Q_{zs} of the substrate

Therefore, lattice parameters of the layer on the substrate could be obtained by,

$$a = a_s \cdot Q_{xs}/Q_x$$

$$c = c_s \cdot Q_{zs}/Q_z$$

The out-of-plane strain is related to the in-plane strain:

$$\frac{c - c_0}{c_0} = -\frac{2\upsilon}{1 - \upsilon}\frac{a - a_0}{a_0}$$

Where, υ is Poisson's ratio and c_0, a_0 and υ could be linearly interpolated between the values for the end members. For InGaN on GaN,

$$a_0 = x \cdot a_{InN} + (1 - x) \cdot a_{GaN}$$

$$c_0 = x \cdot c_{InN} + (1 - x) \cdot c_{GaN}$$

$$v = x \cdot v_{InN} + (1 - x) \cdot v_{GaN}$$

From the equations above, we can get the value of composition x. And the relaxation is,

$$R = \frac{a - a_s}{a_o - a_s}$$

The X'Pert Epitaxy software can give the results of composition and relaxation directly if we indicate the substrate peak and layer peak by using the "semi-automatic peak search" feature.

Résumé

Les diodes électroluminescentes (DEL) à base de GaN ont déjà été commercialisées comme solution économique d'éclairage, étant donné que les multi-puits quantiques (MQW) basés sur InGaN/GaN peuvent être conçus pour produire de la lumière dans toute la gamme spectrale visible. Pour obtenir une émission de lumière blanche, la conversion à base de phosphore conduit à une faible efficacité due à la perte de Stokes et peut également produire un faible indice de rendu des couleurs (IRC). Par conséquent, pour une efficacité élevée et une lumière blanche avec un IRC élevé, la génération de lumière blanche par combinaison rouges-vertes-bleues (RGB) est nécessaire. La DEL bleue basée sur InGaN/GaN présente une bonne performance aujourd'hui. La DEL rouge à base de III-phosphure est également très efficace. Cependant, avec des longueurs d'onde intermédiaires pour l'émission de spectre vert, l'efficacité des dispositifs diminue avec l'augmentation de la composition d'indium (In) dans la région active à cause de l'épitaxie selon la direction de GaN communément utilisée (0001-Ga). Ce «green-gap» est le principal obstacle pour obtenir une DEL blanche sans phosphore. Les structures DEL non ou semi-polaires pourraient être une solution pour réduire ou omettre le problème de polarisation, cependant, une croissance plus facile de bonne qualité cristalline avec moins d'étapes de fabrication font que la croissance de la direction (0001-Ga) est toujours commercialement prometteuse. Par conséquent, une conception de structure optimisée pour atténuer la polarisation et augmenter l'émission optique provenant d'hétéro-structures élaborées dans cette direction de croissance est toujours demandée. Les structures de DEL classiques multi-puits quantiques (MQW) InGaN/GaN sont développées sur une template GaN et utilisent du GaN comme couches barrières. Cependant, notre objectif a été de faire croître des MQW à contenu élevé avec des barrières InGaN sur une nouvelle template InGaN appelé «semi-bulk» (SB). La réalisation de la thèse est de simuler, décroître par épitaxie en phase vapeur organométallique (MOVPE) et de fabriquer la structure de DELs à haute teneur en In dans les barrières MQW avec InGaN, crues sur une template InGaN «semi-bulk» de haute qualité, et qui émettent dans le spectre du bleu au vert.

Mots-clés: LED, MOVPE, InGaN MQW, InGaN <<semi-bulk>>

Abstract

GaN-based light-emitting diodes (LEDs) have already been commercialized for solid-state lighting, since the InGaN/GaN-based multi-quantum-well (MQW) of LEDs can be designed to produce light in the entire visible spectral range. To obtain white LED, phosphor-based down-conversion results in low efficiency due to Stokes loss and also can yield low colour rendering index (CRI). Hence, for highly efficient and with high CRI white light, generation of white light by monolithic red-green-blue (RGB) combination is necessary. InGaN/GaN-based blue LED has good performance now-a-days. III-phosphides based red LED has also achieved good efficiency. However, with intermediary wavelengths for green spectra emission, the efficiency of devices from epitaxy grown along the commonly used (0001-Ga) direction of GaN decreases with increasing indium (In) content in the active region and this "green-gap" is the main obstacle to get phosphor-free white LEDs. Non- or semi-polar LED structures could be a solution to reduce or omit the polarization problem, however, easier growth of good crystal quality and fewer processing steps make (0001-Ga) direction growth still commercially promising. Therefore, optimized structure design to alleviate polarization and enhance optical emission from hetero-structures grown along this direction growth is still in demand. The conventional InGaN multi-quantum-well (MQW) LED structures are grown on GaN buffer and use GaN as barrier layers. However, the objective of this thesis has been to grow high In-content MQWs with InGaN barriers on a novel so called "semi-bulk" (SB) InGaN buffer. The achievement of the thesis was to simulate, grow by metalorganic vapour phase epitaxy (MOVPE) and process LED structure with high In-content in the MQW with InGaN barriers, grown on high quality "semi-bulk" InGaN buffer, that will emit in the blue to green spectra. 70 nm thick high crystal quality InGaN SB buffer was obtained with 5% In-content. On top of this, $In_{0.15}Ga_{0.85}N/In_{0.05}Ga_{0.95}N$ MQW was grown followed by 200 nm optimized p-GaN. The room temperature IQE was 67.5% at 460 nm emission wavelength. The processed LED chips yielded turn-on voltage less than 3 V with leakage current of $\sim 10^{-3}$ A. $In_{0.25}Ga_{0.75}N/ In_{0.05}Ga_{0.95}N$ MQW was also realized on InGaN SB with 7% In, with emission peak at ~530 nm.

Keywords: LED, MOVPE, InGaN MQW, InGaN "semi-bulk" buffer